Design of optical and microwave devices for iot applications and future telecommunications

Politecnico di Bari

Department of Electrical and Information Engineering
ELECTRICAL AND INFORMATION ENGINEERING
Ph.D. Program
SSD: IINF-02/A – ELECTROMAGNETIC FIELDS

Final Dissertation

Design of Optical and Microwave Devices for IoT Applications and Future Telecommunications

---

by
Vito Vincenzo Francione

Supervisor:

Prof. Francesco Prudenzano

Coordinator of Ph.D. Program:
Prof. Mario Carpentieri

Course n°38, 01/11/2022 - 14/02/2026

Politecnico di Bari

Department of Electrical and Information Engineering

ELECTRICAL AND INFORMATION ENGINEERING

Ph.D. Program

SSD: IINF-02/A – ELECTROMAGNETIC FIELDS

Final Dissertation

Design of Optical and Microwave Devices for IoT Applications and Future Telecommunications

---

by

Vito Vincenzo Francione

Referees:

Prof. Maurizio Ferrari

Prof. Francesco Morichetti

Supervisor:

Prof. Francesco Prudenzano

Coordinator of Ph.D. Program:

Prof. Mario Carpentieri

Course n°38, 01/11/2022 - 14/02/2026

Abstract

This PhD thesis is focused on the design, optimization, and characterization of innovative optical and microwave devices supporting the development of the Sixth Generation (6G) of telecommunications and Internet of Things (IoT) applications. The need for high-speed communication and advanced sensing promotes the design of novel microwave and optical devices. The current research addresses these challenges through two distinct approaches: high-frequency devices, useful for Fiber-Wireless (FiWi) networks, and for beam-steering applications, where the antenna design and the improvement of radiative parameters can be achieved by employing Metamaterials (MTMs) and Metasurfaces (MTSs); and optical devices operating in the Mid-InfraRed (Mid-IR) range, targeting sensing or novel communication applications relevant to IoT and 6G.

In particular, the Ph.D. thesis reports the following key contributions: i) the design and optimization of a Mid-IR Fiber Laser based on praseodymium-doped fluoroindate (Pr^{3+}:InF_3) glasses operating at $\lambda_s = 4\ \mu m$; *ii)* the design and optimization of a Mid-IR Optical Fiber Amplifier based on praseodymium-doped

fluoroindate (Pr^{3+}:InF_3) glasses operating at $\lambda_s = 4\ \mu m$; iii) the design, fabrication, and characterization of a non-adiabatic tapered ZBLAN optical fiber sensor operating in the Mid-IR range for temperature measurements; iv) the design, fabrication and characterization of an Antipodal Vivaldi Antenna (AVA) with MTS; v) the design, fabrication and characterization of a Fabry-Perot Antenna (FPA) realized through unconventional fabrication techniques based on inkjet and 3D printing; vi) the design, fabrication and characterization of a Transmitarray Antenna (TA) for beam-steering applications and vii) the design and optimization of a Folded Transmitarray Antenna (FTA) working in the millimeter-wave range. The last activity has been carried out in collaboration with the *Institut d'Electronique et des Technologies du numéRique* (*IETR*) of Rennes (France). Part of this research has been published in international journals and presented at national and international conferences, as detailed in the list at the end of the thesis.

Contents

Introduction

The digital transition represents one of the most critical socio-economic challenges of our time, demanding innovative technological solutions to build reliable, high-speed, and interconnected global infrastructure. The growth of Internet-connected devices, coupled with the rising volume of shared data, constitutes a significant challenge for future network infrastructure. This is a topic of great global interest, with the aim of increasing the transmission speed of information and guaranteeing the efficient use of services like remote working, distance learning, telemedicine, communication systems, and Internet of Things (IoT) systems. These services must be supported by a broadband network that is reliable, efficient, with low latency, and high speed. In recent years, several countries have already initiated research and development programs for the Sixth Generation (6G) of telecommunications, aiming to overcome the limitations of current technology.

Nowadays, hybrid solutions integrating optical and microwave devices have attracted significant research interest. These hybrid solutions have permitted high efficiency and exploitation of innovative and fast wireless communication channels, characterized by wide bandwidth and low latency. The combination of these

two technologies is known in the literature as the Fiber-Wireless (FiWi) network, an architecture where the advantages of optical and microwave devices are combined and find application.

Fiber optic technologies stand out as excellent candidates for providing massive bandwidth, specifically through the adoption of Wavelength Division Multiplexing (WDM) techniques to transmit multiple signals in parallel. Innovation in optical devices is currently also focused on materials, particularly those operating in the Mid-InfraRed (Mid-IR) range, such as fluoroindate, chalcogenide, and ZBLAN glasses. The Mid-IR range, particularly the wavelength range $\lambda = 3 - 5\ \mu m$, is attracting strong interest currently due to its potential for sensing and communication. Several devices can be realized in this wavelength range such as fiber lasers, fiber optical amplifiers, supercontinuum sources, optical combiners, and sensors by adopting passive glasses or glasses doped with rare earths.

In addition, by employing beamforming and beam steering techniques, it is possible to improve the efficiency and the reliability of wireless networks with large coverage areas. The improvement of gain, bandwidth, and beam-steering angle of antennas can be obtained by employing Metamaterials (MTMs) and Metasurfaces (MTSs). They are artificially engineered materials able to modify the properties of electromagnetic waves such as amplitude, phase, and polarization state.

The aim of this research thesis is to propose both optical and microwave devices overcoming the limitations imposed by current technology. To reach this pur-

pose, this thesis proposes microwave devices to enhance next-generation telecommunication systems, and optical devices operating in the Mid-IR range for sensing and communication applications relevant to the IoT and 5G/6G systems. The obtained results are illustrated following this organization:

- Chapter 1: *Microwave and Optical Devices* introduces the state of the art concerning the microwave and optical devices considered in the Ph.D. research activity.
- Chapter 2: *Recall of Theory* reports the fundamental theory for the design of microwave and optical devices considered in the Ph.D. research activity.
- Chapter 3: *Mid-IR Laser and Amplifier Design* describes the design and the optimization of *i)* a fiber laser and *ii)* an optical fiber amplifier based on Praseodymium-doped Fluoroindate glass (Pr^{3+}: InF_3) operating at $\lambda = 4\ \mu m$.
- Chapter 4: *Mid-IR ZBLAN Fiber Temperature Sensor* describes the design, fabrication and characterization of a non-adiabatic tapered ZBLAN fiber sensor operating in the Mid-IR range for temperature measurements.
- Chapter 5: *Design and Fabrication of Antipodal Vivaldi Antenna with MTMs* describes the design, fabrication, and characterization of an Antipodal Vivaldi Antenna (AVA), focusing on how the integration of

MTSs enhances the gain of the antenna while preserving the bandwidth.

- Chapter 6: *Design and Fabrication of Fabry-Perot Antenna* presents the design, fabrication, and characterization of a Fabry-Perot Antenna (FPA) using a hybrid fabrication technique consisting of both inkjet printing and 3D printing technology.
- Chapter 7: *Design and Fabrication of a Transmitarray for Beam Steering* describes the design, fabrication, and characterization of Transmitarray Antenna (TA) for beam steering applications operating for both linearly polarized incident waves at the same frequency.
- Chapter 8: *Dual-Linear-Polarized Folded Transmitarray Antenna Operating in Ka-Band* describes the design and optimization of Folded Transmitarray Antenna (FTA) operating in *mm*-wave range, able to operate for both linearly polarized incident waves at the same frequency.

1 Microwave and Optical Devices

This chapter reviews the state of the art concerning the microwave and optical devices mainly considered in the Ph.D. research activity. It details the evolution of Mid-IR technology, specifically rare-earth doped lasers and amplifiers, and fiber sensors based on soft glasses. Furthermore, the chapter explores the capability of metamaterials to improve antenna radiative properties, with a specific focus on high-gain antennas such as TA and FPA.

1.1 Optical Fiber Devices for Mid-IR Applications

Mid-IR technology is rapidly gaining recognition as a key enabler for future communication networks and IoT applications. The current infrastructure for information and communication technologies (ICT) is primarily limited to terrestrial networks, which consist of fiber-optic and radio access networks [1]. The next-generation ICT infrastructure involves moving beyond just terrestrial networks. It is envisioned as a "multi-layered 3D architecture" integrating networks from underwater to satellite systems [1]. Free Space Optical (FSO) communications are becoming an essential part of this paradigm shift process [1]. Earth-space communication is currently dominated by the Radio Frequency (RF)

range, specifically the Ku-band (12 to 18 GHz) and the Ka-band (26.5 to 40 GHz) [1].

Initially, optical components developed for fiber-optic telecom systems operating in the Short-Wave InfraRed (SWIR, $1 - 2.5\ \mu m$) region were employed for Free Space Optical (FSO) communication. However, the SWIR band is highly susceptible to atmospheric disturbances, rendering it unsuitable for reliable FSO transmission. Consequently, these challenges are significantly mitigated by shifting to longer wavelengths. The Mid-IR region, specifically the Middle-Wave InfraRed (MWIR, $3 - 5\ \mu m$) and Long-Wave InfraRed (LWIR, $8 - 12\ \mu m$) atmospheric transmission bands, offers the necessary resilience and robustness against adverse weather and atmospheric effects. The spectral region from $\lambda = 3\ \mu m$ to $\lambda = 5\ \mu m$, is highly suitable for communication and sensing, as it benefits from a low-loss atmospheric transmission window, thereby enhancing communication range and reliability for long-distance FSO communication and for IoT applications [1-3]. Indeed, in spectroscopy, the Mid-IR wavelength range has attracted significant scientific interest because most molecules exhibit rotational-vibrational absorption lines in this spectral range, showing a characteristic fingerprint [4-5]. Mid-IR sensors can be designed to detect specific gases and pollutants by exploiting their unique fingerprints [6]. Furthermore, fiber optic technology can be used to design sophisticated sensors for sensing physical parameters such as temperature, strain or refractive index measurement [7, 8].

Lastly, Mid-IR emitting sources and amplifiers based on doped fluoroindate fiber have received significant attention in recent years, particularly for optical communications [1, 9] and for environmental monitoring and sensing [6].

1.1.1 Fiber Lasers Based on Rare-Earth Doped Glasses

Fiber lasers and fiber amplifiers can be fabricated with various host glasses, including silicate, tellurite, chalcogenide, and fluoride, which are doped or co-doped with different rare-earth ions such as erbium (Er^{3+}), ytterbium (Yb^{3+}), holmium (Ho^{3+}), praseodymium (Pr^{3+}), neodymium (Nd^{3+}), terbium (Tb^{3+}), or europium (Eu^{3+}) [10-23]. The choice of host glass depends on its operational wavelength range, while the choice of rare-earth dopant determines the specific emission wavelengths [10-23]. In particular, fluoroindate glasses are promising hosts due to their low phonon energy, high transparency (from UV up to $5\mu m$), high rare-earth ion solubility, and low attenuation coefficient [24]. Thanks to these characteristics, fluoroindate glasses are good candidates for laser and amplifier construction [24]. In recent years, spectroscopic analysis of rare-earth doped fluoride glasses has been conducted, with the aim of finding new pumping schemes and operating wavelengths [12-23, 25-29]. Fluoride fibers doped with erbium, holmium and dysprosium have attracted particular attention for their emission at $\lambda_s = 3.4\ \mu m$, $\lambda = 3.9\ \mu m$, and $\lambda = 4.4\ \mu m$, respectively [12-23].

For example, erbium-doped fluoroindate fibers have been demonstrated to operate around $\lambda_s = 3.4\ \mu m$. This operation was achieved utilizing a dual-wavelength pumping scheme at $\lambda_p = 974\ nm$ and $\lambda_p = 1976\ nm$, showing slope efficiency of $\eta = 19\ \%$ [12-13]. Furthermore, theoretical predictions indicate that emission up to $\lambda_s = 3.91\ \mu m$ with a pumping at $\lambda_p = 635\ nm$ is achievable in these fibers, with a maximum slope efficiency $\eta = 1.6\ \%$ and pump power threshold $P_{th} = 25\ mW$ [14]. Fluoroindate fibers doped heavily with holmium have been employed to design Continuous Wave (CW) and gain-switching pulsed lasers emitting at $\lambda_s = 3.92\ \mu m$, when pumped at $\lambda_p = 888\ nm$, with a slope efficiency around $\eta = 10\%$ for the CW laser [15-16]. The low slope efficiency is attributed to the $I_5 \rightarrow I_6$ holmium transition, which is self-terminating. This limitation can be overcome by employing a dual-wavelength pumping scheme at $\lambda_p = 976\ nm$ or $\lambda_p = 1660\ nm$ or by co-doping the fiber with neodymium or europium ions [17-20]. The simulation of dual-wavelength pumping promises a slightly higher slope efficiency of $\eta = 12.1\ \%$ [18] while co-doping holmium with neodymium has been proposed to obtain a slope efficiency $\eta = 16.67\ \%$, and pump power threshold $P_{th} = 0.2\ W$. Lastly, dysprosium-doped fluoroindate fiber lasers have been designed to emit at $\lambda_s = 4.4\ \mu m$, when utilizing a pump source at $\lambda_p = 1.7\ \mu m$ [22-23]. The laser shows a slope efficiency $\eta \approx 27\ \%$ and high pump power threshold $P_{th} \approx 30\ W$ [22, 23]. Recent spec-

troscopic investigations have analysed fluoroindate fibers doped with dysprosium and terbium [30], praseodymium, and praseodymium/ytterbium [31]. Emission at $\lambda_s = 4\ \mu m$ has been reported under two pumping schemes: in the case of praseodymium-doped fluoroindate fiber, it must be pumped at $\lambda_p = 1550\ nm$, while in the case of praseodymium/ytterbium co-doped fluoroindate fiber it must be pumped at $\lambda_p = 980\ nm$ [31]. In this thesis, a Mid-IR Fiber Laser based on Praseodymium-doped fluorindate glasses has been designed and optimized, with the aim of proposing new innovative sources operating in the Mid-IR range.

1.1.2 Mid-IR Optical Fiber Amplifier

In recent years, several Mid-IR optical fiber amplifiers have been simulated and experimentally demonstrated [32-38]. Fluoride glasses doped with erbium have been developed to work in the range $\lambda_s = 2.7 - 2.8\ \mu m$, leading to the development of optical fiber amplifiers in zirconium fluoride glasses for CW and nanosecond pulse amplification [32-34]. For the longer wavelengths ($\lambda_s = 4.3\ \mu m$ and beyond), chalcogenide glasses doped with praseodymium, dysprosium, and terbium are employed for broadband and ultrashort pulse amplification [35, 36]. Alternative solutions include Master Oscillator Power Amplifier (MOPA) based on dysprosium-doped chalcogenide glasses operating at $\lambda_s = 4.38\ \mu m$ [37] and tapered fiber coupled with microspheres based on Erbium-doped chalcogenide

glasses used for amplification at a central wavelength $\lambda_s = 2.77\ \mu m$ [38]. In this thesis, a Mid-IR optical fiber amplifier based on praseodymium-doped fluoroindate glasses has been designed and optimized, with the aim of proposing an integrated amplifier into an all-in-fiber system operating in the Mid-IR.

1.1.3 Mid-IR Fiber Optic Sensor

Sensors are crucial elements for environmental monitoring applications, where real-time data on air quality and other physical parameters, such as strain or temperature, are vital for public health and safety [39-45]. Fiber-optic sensors have received ever-increasing attention due to their well-known intrinsic advantages, e.g., immunity to electromagnetic interference, compact size, and low cost [7, 46]. Optical fiber sensors can be identified by considering the employed operational principle, e.g., long period gratings [40], fiber Bragg gratings [41,42], plasmon resonances [43], in-line interferometers [44], and tapers [45]. Silica all-fiber interferometers are widely recognized for their high sensitivity, compact size, low fabrication cost, and broad measurement range [46, 47-49]. A possible implementation is based on a non-adiabatic optical fiber taper, to excite cladding modes and exploit the different optical path lengths of the electromagnetic modes. This allows obtaining a comb spectrum at the output, which shifts with strain, environmental refractive index change, and temperature variation [48-49]. The fabrication of Mid-IR compatible devices utilizing fluoride optical fiber is currently receiving significant attention. For instance, a fluoride fiber sensor

based on a side-polished structure has been demonstrated for refractive index measurement [8]. The employment of fluoride glasses is promising for different reasons: *i)* the higher operating wavelength λ leads to higher sensitivity and *ii)* the Mid-IR is the fingerprint region of several molecules [7]. Despite this interest, few fluoride optical fiber sensors fabricated using heating techniques have been reported in the literature, likely due to the inherent challenges associated with processing this type of glass [7,50]. In this thesis, a non-adiabatic tapered ZBLAN optical fiber sensor working in the Mid-IR range is designed and characterized. The feasibility of temperature sensing, based on Mach-Zehnder interferometry of the optical modes in a ZBLAN taper fiber, is demonstrated.

1.2 High-Gain Antenna Technologies

High-gain antennas are essential for long-distance communication systems, including radar, satellite, and emerging 5G/6G applications [51, 52]. In advanced wireless communications, microwave and millimeter-wave (mm-Wave) technology relies primarily on antennas to establish a secure, stable, and fast link with the user. A key requirement is the ability to maintain connectivity with a moving user, which demands that antennas be capable of changing the direction of their main lobe: this is achieved through beam-steering and beam-forming techniques, typically implemented using antenna arrays. In an array, steering is

achieved by introducing a specific time delay between the elements, so that the contributions from all elements are coherently summed [53].

However, traditional high-gain solutions, such as reflector antennas and phased antenna arrays, provide strong directional gain but suffer from significant drawbacks. Reflectors are often large and heavy, while phased arrays require complex feed networks and numerous phase shifters, which introduce significant insertion losses, increase cost, and reduce overall efficiency [51, 52].

The technology to be employed for the fabrication of these arrays is critical. Microstrip technology is one possible implementation; this is low-cost and easy to construct, but it suffers from parasitic current losses, which degrade efficiency. Substrate Integrated Waveguide (SIW) technology is often considered a better solution; in fact, it offers a good trade-off, providing high integration, compactness, ease of construction, and intermediate power handling [54-59]. SIW technology is employed for the fabrication and integration of microwave devices, like waveguides and filters, into a single substrate using metalized vias, and recent research has been focused on partially air-filled SIW to further reduce dielectric losses and improve gain [57-59].

1.2.1 Transmitarray and Reflectarray Antennas

To overcome these limitations, Reflectarray Antennas (RAs) and TAs have been developed, offering lower mass, reduced volume, and simpler manufacturing while maintaining high performance [60-63]. Unlike RAs, which operate in reflection mode, TAs transmit the signal and avoid feed blockage [64, 65]. A key challenge is managing the antenna profile, as TAs and RAs often require long focusing lengths, which limits practical applications [66]. Folded configurations (FTAs) are a compact solution developed to reduce the focal distance (F) and increase practicality [66]. The overall performance of a TA system depends critically on the focal distance to metasurface size (F/D ratio) which influences both spillover and taper efficiency [67]. MTMs and MTSs can be employed in the design of RA and TA antennas in both conventional and folded configurations. In the literature, various solutions have been reported, including conventional and folded RA and TA antennas designed for single linear polarization [51, 52, 66, 68], dual linear polarization [64, 65], and circular polarization [60, 61, 69-72]. For TAs and RAs operating with Dual Linear Polarization (DLP), dual-band solutions have been proposed [64, 65, 73].

More recently, dual-linear polarized RA, TA and FTA operating at the same frequency have been proposed [62, 74-79]. In this thesis, TAs in traditional and folded configurations are investigated and designed to operate at the same frequency with DLP.

1.2.2 Metamaterial and Metasurface

MTMs and MTSs are engineered artificial materials that exhibit unusual electromagnetic properties not found in nature [80]. While MTMs are defined as three-dimensional (3D) structures, MTSs represent their two-dimensional planar counterparts [80]. These materials are composed of metallic elements that are small compared to the guided wavelength [80]. Therefore, they can be considered as electromagnetically homogeneous media. They are characterized by specific relative dielectric permittivity ϵ_r and relative magnetic permeability μ_r. These parameters can be engineered to achieve specific values, including negative values not available in nature. MTMs can be classified by the sign of the relative dielectric permittivity and the magnetic permeability. The four possible sign combinations can be arranged in an $\epsilon - \mu$ diagram [81].

These materials allow for precise control of various electromagnetic properties such as the amplitude, phase, and polarization of the transmitted or reflected waves [70, 80, 82, 83]. For example, they can improve antenna performance in terms of directivity and gain, while keeping a compact size and low profile [84-86]. MTMs are also utilized to enhance impedance matching with biological tissues for medical applicators, as well as in the development of electromagnetic tracking systems for surgical navigation [85-88]. In this thesis, metamaterials are investigated to improve the gain and bandwidth of a Vivaldi Antenna and for the design of TA in traditional and folded configurations.

1.2.3 Low-Cost Inkjet-Printed Antennas

The demand for cost-effective, compact, and lightweight antennas is rapidly increasing due to the spreading of wireless communication systems and services such as IoT applications and wearable devices. In this context, conductive inkjet printing has emerged as a promising candidate [89, 90]. Conductive inkjet printing has been successfully used to build conventional antenna designs, but its use for metamaterial-based antennas remains largely underexplored [90-92]. For example, conductive inkjet has been employed to design a wideband 4x4 microstrip patch array on flexible Polyethylene Terephthalate (PET) substrates, analysing the performance impact of curving [89]. The work in [90] demonstrates a full characterization of the inkjet-printing process on paper substrates to design and fabricate high-gain Ultra-Wide Band (UWB) Vivaldi antennas and miniaturized log-periodic arrays [90]. Furthermore, a multilayer inkjet process was demonstrated for fabricating patch arrays on Liquid Crystal Polymer (LCP) substrates working at 24 GHz [91]. Lastly, the inkjet process was adapted for eco-friendly fibrous substrates, such as cardboard [92]. This adaptation involved a dielectric ink pretreatment, which minimizes high-frequency conductor losses. Fabry-Pérot Antennas (FPAs) have gained significant attention due to their ability to achieve high directivity and a low profile [93]. This performance is achieved by placing a simple radiator within a resonant cavity, where multiple in-phase reflections between a total reflector and a Partially Reflective Surface

(PRS) coherently enhance the directivity of the radiator [94]. The resulting improvement is critically dependent on the reflective properties of the PRS, which can be designed using various strategies, such as metalized frequency-selective-surfaces (FSSs) non-metalized all-dielectric slabs, and electromagnetic band-gap structures [93-98]. In this thesis, an FPA is designed and fabricated using unconventional and low-cost materials, such as ultra-thin PET (Polyethylene Terephthalate) substrates, conductive inkjet patterns, and all-dielectric 3D-printed PETG (Polyethylene Terephthalate Glycol) layers.

2 Recall of Theory

In this chapter, the fundamental theory required for the design of Mid-IR optical and microwave devices, investigated in this Ph.D. research activity, is briefly recalled. The first part presents the analytical models of the fiber laser and optical fiber amplifier; the second describes the working principle of a tapered fiber sensor based on the Mach-Zehnder Interferometry (MZI) effect; and finally, the last part details the analytical models of AVA, FPA, and TA antennas.

2.1 Analytical Models for Pr^{3+}: InF_3 Glasses

In this section, analytical models of the fiber laser and optical fiber amplifier are reported. The praseodymium-doped fluoroindate glass can be modelled by a 6-level diagram, when pumped at wavelength $\lambda_p = 1550\ nm$. Fig. 2.1 shows the 6-level energy scheme and the energetic transitions considered [99]. The emission phenomena to be considered are depicted with solid arrows, while the absorption phenomena are depicted with dashed arrows. In particular, the energetic transitions reported are: *i)* pump absorption; *ii)* stimulated emission; *iii)* radiative and non-radiative emissions; and *iv)* Excited-State Absorption (ESA), Upconversion (UP) and Cross-Relaxation (CR) phenomena.

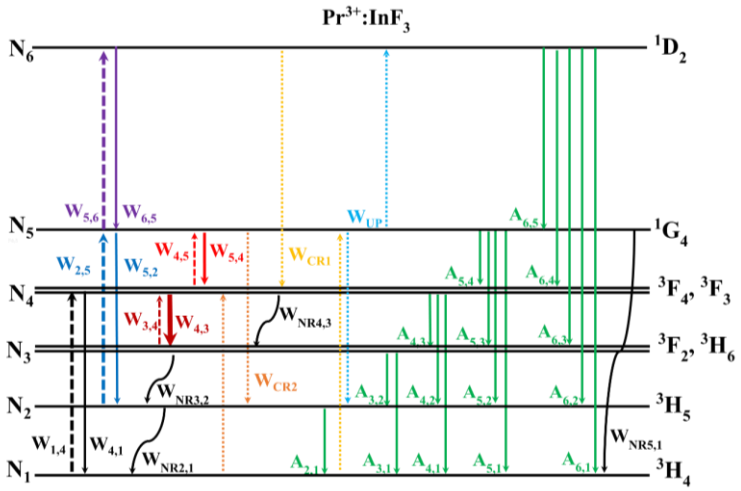

Figure. 2.1 6-level energy diagram of Pr^{3+}:InF_3 glass including pump absorption (dashed black arrow); stimulated emission at $\lambda_s = 4\ \mu m$ (solid dark-red arrow) and at $\lambda_s = 3.56\ \mu m$ (solid red arrow); radiative (solid green arrows) and non-radiative (solid curved black arrows) emissions; and ESA (dashed blue and violet arrows), UP (light-blue dotted arrows), and CR (orange and yellow dotted arrows) phenomena [99].

The following rate equations can be written and solved to evaluate the ion populations of each level $N_1, \dots, N_6$:

$$\begin{aligned}\frac{\partial N_1}{\partial t} = & -W_{14}N_1 + W_{41}N_4 + A_{61}N_6 + A_{51}N_5 + A_{41}N_4 + A_{31}N_3 \\ & + A_{21}N_2 - W_{CR1}N_6N_1 + W_{NR21}N_2 - W_{CR2}N_1N_5 \\ & + W_{NR51}N_5\end{aligned} \tag{2.1}$$

$$\begin{aligned}\frac{\partial N_2}{\partial t} = & -W_{25}N_2 + W_{52}N_5 - \frac{1}{\tau_{R2}}N_2 + A_{62}N_6 + A_{52}N_5 + A_{42}N_4 \\ & + A_{32}N_3 + W_{CR2}N_1N_5 + W_{UP}N_5^2 + W_{NR32}N_3 - W_{NR21}N_2\end{aligned} \tag{2.2}$$

$$\frac{\partial N_3}{\partial t} = -W_{34}N_3 + W_{43}N_4 - \frac{1}{\tau_{R3}}N_3 + A_{63}N_6 + A_{53}N_5 + A_{43}N_4 - W_{NR32}N_3 + W_{NR43}N_4 \tag{2.3}$$

$$\frac{\partial N_4}{\partial t} = W_{14}N_1 - W_{41}N_4 - W_{43}N_4 + W_{34}N_3 + W_{54}N_5 - W_{45}N_4 - \frac{1}{\tau_{R4}}N_4 + A_{64}N_6 + A_{54}N_5 + W_{CR1}N_6N_1 + W_{CR2}N_1N_5 - W_{NR43}N_4 \tag{2.4}$$

$$\frac{\partial N_5}{\partial t} = W_{25}N_2 - W_{52}N_5 + W_{65}N_6 - W_{56}N_5 - W_{54}N_5 + W_{45}N_4 - \frac{1}{\tau_{R5}}N_5 + A_{65}N_6 + W_{CR1}N_6N_1 - W_{CR2}N_1N_5 - 2W_{UP}N_5^2 - W_{NR51}N_5 \tag{2.5}$$

$$\frac{\partial N_6}{\partial t} = -W_{65}N_6 + W_{56}N_5 - \frac{1}{\tau_6}N_6 - W_{CR1}N_6N_1 + W_{UP}N_5^2 \tag{2.6}$$

where $A_{i,j}$ and $W_{NR,ij}$ are the radiative decays and the non-radiative decay rates between the i-th and j-th levels, respectively. The radiative decays $A_{i,j}$ are defined as $A_{i,j} = \beta_{i,j}/\tau_i$ where τ_i are the i-th level lifetimes and $\beta_{i,j}$ are the branching ratios for the $i \rightarrow j$ transition. The coefficient W_{CR} is the cross-relaxation rate, while the coefficients W_{ij} are the transition rates for the $i \rightarrow j$ transition. The term W_{UP} is the up-conversion coefficient, whereas the transition rates for the pump $W_{i,j}^{p}$, the signal $W_{i,j}^{s}$, and the Amplified Spontaneous Emission (ASE) $W_{i,j}^{ASE}$ are defined by the following equations:

$$W_{i,j}^{p,s} = \frac{\sigma_{i,j}(\lambda_{p/s})}{h\, c_0/\lambda_{p,s}} \frac{\Gamma(\lambda_{p/s})}{A_d} P_{p/s}(z) \tag{2.7}$$

$$W_{i,j}^{ASE} = \int_0^{+\infty} \frac{\sigma_{i,j}(\lambda)}{h\, c_0/\lambda_{p,s}} \frac{\Gamma(\lambda)}{A_d} S_{ASE}(z,\lambda) \tag{2.8}$$

where $\sigma_{i,j}(\lambda)$ is the cross section between the i-th and j-th levels at the wavelength λ; $\Gamma(\lambda)$ is the overlap coefficient; h is the Planck constant, c_0 is the speed of light in vacuum; A_d is the core doped area; $P_{p,s}(z)$ is the pump or signal power, and $S_{ASE}(z,\lambda)$ is the ASE power spectrum density. The rate equation system (2.1-2.6) can be solved in steady-state conditions, considering the conservation of the total ions concentration $N_{Pr} = N_1 + N_2 + N_3 + N_4 + N_5 + N_6$. The overlap coefficient $\Gamma(\lambda)$ is defined by the following expression [24, 99-101]:

$$\Gamma(\lambda) = \frac{\int_{A_d} |E_i(x,y)|^2 dx\, dy}{\int_A |E_i(x,y)|^2 dx\, dy} \tag{2.9}$$

where $E_i(x,y)$ is the distribution of the electric field in the doped cross-section area A_d within the total cross-section fiber area A. The following three equations have been considered to model the pump power P_p, the signal power P_s, and the ASE power spectral density $S_{ASE}^{\pm}$ as a function of the fiber length z:

$$\frac{\partial P_p}{\partial z} = \left[g_p(z) - \alpha(\lambda_p)\right] P_p(z) \tag{2.10}$$

$$\frac{\partial P_s^{\pm}}{\partial z} = \pm[g_s(z) - \alpha(\lambda_s)]P_s^{\pm}(z) \tag{2.11}$$

$$\frac{\partial S_{ASE}^{\pm}}{\partial z} = \pm\{[-\sigma_{34}(\lambda)N_3(z) + \sigma_{43}(\lambda)N_4(z)]\Gamma(\lambda) - \alpha(\lambda)\} \cdot S_{ASE}^{\pm}(\lambda, z) \pm a_{sp}(\lambda) \tag{2.12}$$

where α is the glass attenuation at the wavelength λ, and $a_{sp}(\lambda) = 2hc_0/\lambda\left(\sigma_{43}(\lambda)N_4(z) + \sigma_{54}(\lambda)N_5(z)\right)\Gamma(\lambda)$ is the spontaneous emission term. The superscripts $+$ and $-$ denote respectively the forward and backward components of ASE power spectral density S_{ASE}, and the signal power P_s. The terms $g_p(z)$ and $g_s(z)$ are the pump and signal gains along the fiber length z defined as follows:

$$g_p(z) = [-\sigma_{14}(\lambda_p)N_1(z) + \sigma_{41}(\lambda_p)N_4(z) - \sigma_{25}(\lambda_p)N_2(z) + \sigma_{52}(\lambda_p)N_5(z) - \sigma_{56}(\lambda_p)N_5 + \sigma_{65}(\lambda_p)N_6]\Gamma(\lambda_p) \tag{2.13}$$

$$g_s(z) = [-\sigma_{34}(\nu_s)N_3(z) + \sigma_{43}(\nu_s)N_4(z) - \sigma_{45}(\lambda_s)N_4(z) + \sigma_{54}(\lambda_s)N_5(z)]\Gamma(\lambda_S) \tag{2.14}$$

In the case of a fiber laser, the following boundary conditions are imposed:

$$P_p(0) = P_{p0} \tag{2.15}$$

$$P_s{}^{+}(0) = R_{in}P_s^{-}(0) \tag{2.16}$$

$$P_s{}^{-}(L) = R_{out}P_s^{+}(L) \tag{2.17}$$

where $z = 0$ and $z = L$ represent the ends of the laser cavity, R_{in} and R_{out} are respectively the input and output mirror reflectivity, and P_{p0} is the input pump power. The initial conditions for level populations are also imposed as follows:

$$N_1(0) = N_{Pr} \tag{2.18}$$

$$N_2(0) = N_3(0) = N_4(0) = N_5(0) = 0 \tag{2.19}$$

In the case of an optical fiber amplifier, the following boundary conditions are imposed:

$$P_p(0) = P_{p0} \tag{2.20}$$

$$P_s(0) = P_{s0} \tag{2.21}$$

$$S_{ASE}{}^{+}(0, \lambda) = 0 \tag{2.22}$$

$$S_{ASE}{}^{-}(L, \lambda) = 0 \tag{2.23}$$

where P_{s0} is the input signal power. The gain G and the noise figure NF for small signal operation of the fiber optic amplifier are defined by the following equations:

$$G = \frac{P_s(L)}{P_s(0)} \tag{2.24}$$

$$NF = 10 \log\left(\frac{1}{G}\left(1 + \frac{S_{ASE}{}^{+}(L, \lambda_s)}{hc_0/\lambda_s}\right)\right) \tag{2.25}$$

2.2 Tapered Fiber Sensor

The fabrication of an optical fiber taper involves the diametrical reduction of the core and cladding radii by heating and pulling the fiber [102, 103]. The adiabatic or non-adiabatic nature of this transition defines the behaviour of the guided light. In a single-mode optical fiber, an adiabatic taper maintains power confinement within the fundamental mode LP_{01} [103]. In a non-adiabatic taper, the power of the fundamental mode (LP_{01}) is coupled into Higher Order Mode (HOM), which co-propagates within the transition and waist regions. Fig. 2.2(a) shows a schematic of the non-adiabatic taper regions (down-taper, waist, and up-taper), in which the fundamental mode LP_{01} co-propagates with the LP_{0m} mode. Due to the varying optical paths of these co-propagating modes, a MZI effect is produced. The interference between the fundamental mode LP_{01} and the HOM mode (LP_{0m}) generates a periodic series of transmission maxima and minima at the spectrum output, forming a comb spectral response [104]. Fig. 2.2 (b) shows this operating principle, illustrating the comb spectrum at the output.

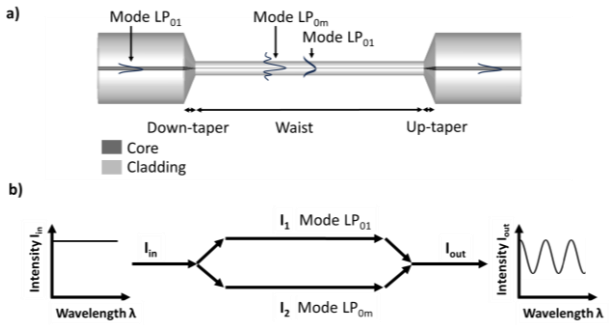

Figure 2.2 a) Diagram of a non-adiabatic taper's regions: down-taper, waist, and up-taper. b) Operating principle of the non-adiabatic taper as a Mach-Zehnder interferometer. [7].

The following equation is used to estimate the output intensity of the interference between the core and cladding modes [48, 49]:

$$I = I_1 + I_2 + 2\sqrt{I_1 I_2}\cos(\Delta\phi) \tag{2.26}$$

$$\Delta\phi = \frac{2\pi\Delta n_{eff} L_{eff}}{\lambda} \tag{2.27}$$

where I_1, I_2 are the intensities of the LP_{01} mode and of the LP_{0m} mode in the waist region, respectively, $\Delta\phi$ and Δn_{eff} are the phase difference and the effective refractive index difference between the aforementioned modes, L_{eff} is the effective length of the taper, and λ is the wavelength. The output intensity I changes when an external quantity (i.e., strain or environmental temperature) induces a variation in the refractive index difference Δn_{eff} and effective length of the taper L_{eff}.

2.2.1 Optical Fiber Taper

The tapering method involves heating and stretching an optical fiber. Fig. 2.3 shows a representation of a fused biconical taper with the main parameters: the original cladding diameter d_{cl}, the original core diameter d_{co}, the waist region diameter $d_{cl,w}$, the waist region length L_w, and the transition region length Z_0

The process of fiber tapering is characterized by two parameters: e the total elongation of the fiber after heating and stretching, and L_0 the starting length of the fiber [105]. The reduction of the waist radius r_w follows an exponential decay profile as a function of elongation e [106, 107]:

$$r_w(e) = r_0^{-\left(\frac{e}{2L_0}\right)} \tag{2.28}$$

Under the assumption that the final waist length L_w is equal to the initial heated length L_0, i.e. $L_w = L_0$, and considering the conservation of the total geometry during the fabrication process, i.e. $2Z_0 + L_W = e + L_0$, the taper profile r depends on the longitudinal coordinate z [106, 107]:

$$r(z) = r_0^{-\left(\frac{z}{L_0}\right)} \tag{2.29}$$

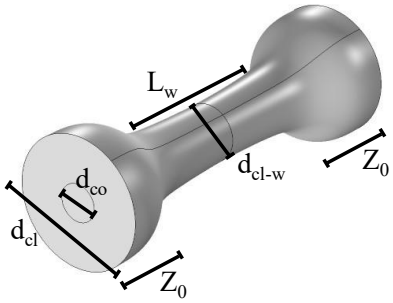

Figure 2.3 Sketch of a taper optical fiber with the main geometrical parameters.

Propagation losses in optical fiber devices are mainly due to two primary mechanisms: scattering, where light radiates out of the core, and coupling, where power is transferred from core modes to cladding radiation modes [108, 109]. Scattering losses are negligible if the following condition is verified:

$$\frac{\lambda}{n_{cl}} \leq Z_0 \tag{2.30}$$

where λ is the wavelength in vacuum of the light signal, and n_{cl} is the refractive index of the fiber cladding. The modal coupling losses are negligible if the following condition is verified:

$$Z_0 \leq \frac{2\pi}{|\beta_1 - \beta_2|} \tag{2.31}$$

where β_1 is the propagation constant of the core mode and β_2 is the propagation constant of the cladding mode closest to β_1. If both conditions are met, a low-loss fiber taper is designed:

$$\frac{\lambda}{n_{cl}} \leq Z_0 \leq \frac{2\pi}{|\beta_1 - \beta_2|} \tag{2.32}$$

To maintain the adiabatic condition in a tapered optical fiber, the tapering angle Ω must be kept sufficiently small, i.e. the transition must be gradual. The tapering angle Ω is defined as the angle between the longitudinal axis of the fiber and the core-cladding interface in the transition region [110]:

$$\Omega \leq \frac{r_{co}(z)}{2\pi}|\beta_1 - \beta_2| \tag{2.33}$$

where r_{co} is the core radius of the fiber.

2.3 Antipodal Vivaldi Antenna

The design of AVA is based on well-known formulas that model its exponential flares [111, 112]:

$$x_i = C_{1_i} e^{R_i y} + C_{2_i} \tag{2.34}$$

where R is the exponential opening rate. The start $P_{1,i}\ (x_{1,i}, y_{1,i})$ and end $P_{2,i}\ (x_{2,i}, y_{2,i})$ points of the exponential curves are used to determine the coefficients C_{1i} and C_{2i}, according to the following equations:

$$C_{1_i} = \frac{x_{2,i} - x_{1,i}}{e^{R_i y_{2,i}} - e^{R_i y_{1,i}}} \tag{2.35}$$

$$C_{2_i} = \frac{x_{1,i} e^{R_i y_{2,i}} - x_{2,i} e^{R_i y_{1,i}}}{e^{R_i y_{2,i}} - e^{R_i y_{1,i}}} \tag{2.36}$$

Fig. 2.4 shows the top and bottom layout of the designed AVA and the main geometrical parameters.

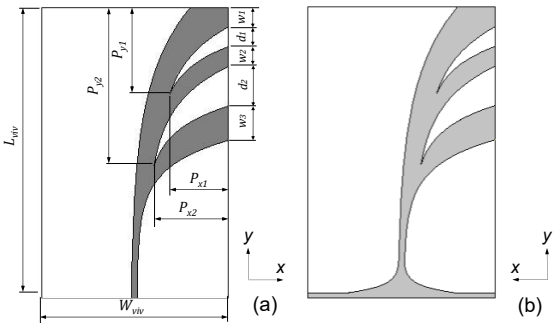

Figure 2.4 a) Top and b) bottom layer of the designed AVA with the main geometrical parameters. Image taken from [113].

A novel MTM is designed in this thesis to improve the radiation performance of the AVA. The effective electric permittivity (ε_{eff}) and the effective magnetic permeability (μ_{eff}) of the MTM are determined by averaging its local charge, current, and field distributions. These parameters can be numerically extracted using the S-Parameter Retrieval Method (SPR), based on the Kramers-Kronig relationship [114, 115]. This method utilizes the S-parameters (S_{11}) and (S_{21}) to first obtain the complex wave impedance (Z_{eff}) and refractive index (N_{eff}), from which the effective permittivity (ε_{eff}) and permeability (μ_{eff}) are calculated [114, 115]. In particular, the complex wave impedance (Z_{eff}) and refractive index (N_{eff}) are calculated using the following equations [114-115]:

$$Z_{eff} = \pm\sqrt{\frac{(1+S_{11})^2 - S_{21}^2}{(1-S_{11})^2 - S_{21}^2}} \tag{2.37}$$

$$N_{eff} = \frac{1}{k_0 L}\cos^{-1}\left(\frac{1 - S_{11}^2 + S_{21}^2}{2S_{21}}\right) \tag{2.38}$$

Finally, the effective permittivity (ε_{eff}) and permeability (μ_{eff}) are calculated using the following equations [114, 115]:

$$\epsilon_{eff} = \frac{N_{eff}}{Z_{eff}} \tag{2.39}$$

$$\mu_{eff} = N_{eff} \cdot Z_{eff} \tag{2.40}$$

2.4 Analytical Model of the Fabry-Perot Antenna

The analytical modelling of the FPA is performed using the ray-tracing method [116, 117]. The operating principle of the antenna is illustrated in Fig. 2.5.

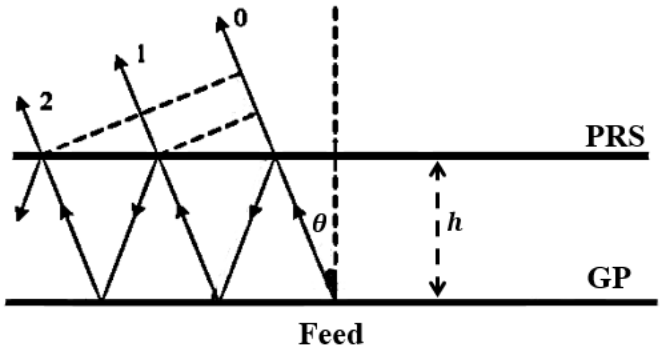

Figure 2.5 Operating principle of the FPA based on antenna ray-tracing model. Image adapted from [117].

The feeding source is modelled as a central point source located on the metal Ground Plane (GP), emitting an electromagnetic field. A PRS is positioned at distance h above the ground plane, creating a cavity that supports multiple reflections with tapering magnitudes. The complex reflection coefficient of the PRS is defined as $pe^{j\phi_{PRS}}$, where p denotes the reflection magnitude and ϕ_{PRS} denotes the reflection phase [117]. In the case of an infinite transverse dimension and a lossless structure, the magnitude of the direct ray (ray 0) is proportional to $\sqrt{1-p^2}$, the magnitude of the first reflected ray (ray 1) is proportional to $p\sqrt{1-p^2}$, the magnitude of the second reflected ray (ray 2) is proportional to $p^2\sqrt{1-p^2}$, and in general, the magnitude of the *n*-th reflected ray is proportional to $p^n\sqrt{1-p^2}$. Taking into account the geometric path differences and also the phase shifts induced by reflections at the ground plane and the PRS, the total phase difference of the *n*-th ray relative to the direct ray (ray 0) is derived as [117-119]:

$$\Delta_n = n\left[\phi_{PRS} - \phi_{BOT} - \frac{4\pi f}{c} h\cos\theta\right] \tag{2.41}$$

where ϕ_{PRS} is the reflection phase response of the PRS, ϕ_{BOT} is the phase introduced by the ground plane, which is $\phi_{BOT} = \pi$ in the case of a Perfect Electric Conductor (PEC), f is the resonance frequency of the cavity, h is the cavity

thickness (i.e. the distance between the PRS and the ground plane), c is the speed of light, and n is an integer number $n = 0,1,2, ...$

To achieve maximum directivity in the broadside direction, the PRS reflection phase ϕ_{PRS} should satisfy the following condition [95, 117-119]:

$$\phi_{PRS} = \frac{4\pi hf}{c} + (2n-1)\pi \tag{2.42}$$

The total directivity of the FPA D_{FPA} can be approximated by combining the directivity of the feed source D_S and the directivity contribution of the PRS D_{PRS} [117-119]. This latter contribution depends on the magnitude of the reflection coefficient ρ of the PRS:

$$D_{FPA}\,(dBi) = D_S\,(dBi) + D_{PRS}\,(dB) \tag{2.43}$$

$$D_{PRS}\,(dB) = 10 \times \log_{10}\left(\frac{1+\rho}{1-\rho}\right) \tag{2.44}$$

Standard PRS structures generally exhibit a negative reflection phase ϕ_{PRS} gradient with respect to frequency. Consequently, the resonance condition is satisfied only at a specific frequency, leading to a very narrow $-3\ dB$ gain bandwidth BW_G [120, 121]. To improve the gain bandwidth, a PRS with a positive phase gradient is required. Various approaches have been proposed to achieve this, including single-layer printed PRSs, multilayer printed PRSs, and unprinted dielectric slabs [93-95, 120-122].

2.5 Analytical Model of the Transmitarray Antenna

2.5.1 Working Principle

The operating principles of the two architectures for a DLP regime are illustrated in Fig. 2.6: a) the traditional configuration, namely DLP-TA and b) the folded configuration, namely DLP-FTA. The traditional configuration consists of a primary feed and a TA layer; whereas the folded version consists of a TA layer (orange layer), a reflector or ground plane (green layer), and a primary feed antenna embedded within the ground plane. The elementary Unit Cell (UC) is designed ad hoc to operate in a DLP regime at the same frequency. In particular, in the TA configuration, the DLP-UC employed in the TA layer is a Phase Compensator (PC) with a transmission magnitude coefficient close to unity [70]. In the FTA configuration, the DLP-UC is based on a PC combined with a PRS. When an *x*-polarized (or *y*-polarized) incident wave hits the UC, half of the power is transmitted and phase compensated considering the focal distance $F/3$, and half of the power is reflected from the TA layer towards the ground plane. After double reflection in the cavity, the *x*-polarized (or *y*-polarized wave) is transmitted and compensated considering the focal distance F. The TA layer has a dual function: *i)* to transmit and compensate the co-polarized (with respect to the incident wave) components, and *ii)* to minimize the cross-polarized (with respect to the incident wave) components. Afterwards, these components will be referred to as co-polarized and cross-polarized components.

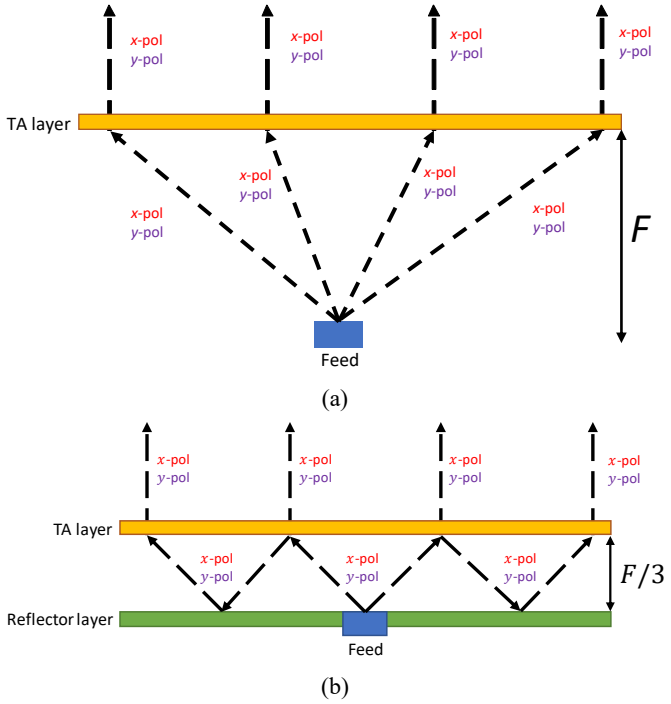

Figure 2.6 Scheme of a) DLP-TA and b) DLP-FTA.

2.5.2 Phase Compensator

The PC should be designed to transform the spherical wavefront radiated by the feed antenna into a planar wavefront. The phase compensation, introduced by the UC, compensates the spatial phase delay due to the distance d_P, between the phase center of the feed antenna and the position of the i-th UC. According to array theory, if the beam direction is (θ, ϕ), the phase of the transmitted electric field of the i-th UC of the TA, denoted as $\Phi(x_i, y_i)$, is given by [123]:

$$\Phi(x_i, y_i) = -k_0 \sin\theta \, (x_i \cos\phi + y_i \sin\phi) \tag{2.45}$$

where (x_i, y_i) are the coordinates of the *i*-th UC and k_0 is the free space wavenumber. The phase $\Phi(x_i, y_i)$ can be also calculated by summing the phase contribution due to the propagation path of the incident electric field $(-k_0 d_P)$ and the transmission phase shift introduced by the UC itself, denoted as $\Phi_{UC}(x_i, y_i)$ [123]:

$$\Phi(x_i, y_i) = -k_0 d_P + \Phi_{UC}(x_i, y_i) \tag{2.46}$$

where d_P is the distance between the feed phase center (x_{FD}, y_{FD}, z_{FD}) and the position of the *i*-th UC of the TA (x_i, y_i, z_i). The distance is defined as:

$$d_P = \sqrt{(x_i - x_{FD})^2 + (y_i - y_{FD})^2 + (z_i - z_{FD})^2} \tag{2.47}$$

Combining equations (2.45) and (2.46), the required transmission phase shift introduced by the UC $\Phi_{UC}(x_i, y_i)$ is [123]:

$$\Phi_{UC}(x_i, y_i) = k_0 \, [d_P - \sin\theta \, (x_i \cos\phi + y_i \sin\phi)] \tag{2.48}$$

For the broadside direction $(\theta, \phi) = (0°, 0°)$ the equation simplifies as follows:

$$\Phi_{UC}(x_i, y_i) = k_0 \sqrt{(x_i - x_{FD})^2 + (y_i - y_{FD})^2 + (z_i - z_{FD})^2} + \phi_r \tag{2.49}$$

where the term ϕ_r has been added in the equation for the DLP-FTA configuration to account for the additional phase shift due to the reflection within the cavity. A 2-bit or 3-bit phase quantization scheme is applied to each element of the TA, selected based on the following criteria [51, 52]:

$$\Phi_{UC} = \begin{cases} 0° & 0° \leq \Phi_{UC} < 90° \\ 90° & 90° \leq \Phi_{UC} < 180° \\ 180° & 180° \leq \Phi_{UC} < 270° \\ 270° & 270° \leq \Phi_{UC} < 360° \end{cases} \tag{2.50}$$

$$\Phi_{UC} = \begin{cases} 0° & 0° \leq \Phi_{UC} < 45° \\ 45° & 45° \leq \Phi_{UC} < 90° \\ 90° & 90° \leq \Phi_{UC} < 135° \\ 135° & 135° \leq \Phi_{UC} < 180° \\ 180° & 180° \leq \Phi_{UC} < 225° \\ 225° & 225° \leq \Phi_{UC} < 270° \\ 270° & 270° \leq \Phi_{UC} < 315° \\ 315° & 315° \leq \Phi_{UC} < 360° \end{cases} \tag{2.51}$$

2.5.3 Geometrical Dimensions

The focal distance F and aperture size D of the TA define the spillover efficiency η_{spill}, the illumination efficiency η_{ill}, and the total efficiency η.

The spillover efficiency is the ratio of the power intercepted by the TA aperture to the total power radiated by the feed. It can be expressed in closed form as a function of the F/D ratio [124-126]:

$$\eta_{spill} = 1 - \cos^{2q+1}\theta_0 \tag{2.52}$$

where q represents the exponent of the function $\cos^q \theta_0$, assuming that the normalized gain profile of the feed antenna can be approximated by this function, and $\theta_0$is the illumination angle at the aperture edge defined as $\theta_0 = \tan^{-1} 2D/F$ The illumination efficiency η_{ill} represents the aperture utilization of the TA and can also be written in closed form as a function of the ratio F/D according to [124-126]:

$$\eta_{ill} = \frac{[((1-\cos^{q+1}\theta)/(q+1)) + ((1-\cos^{q+1}\theta)/q)\,]^2}{2\tan^2\theta\ [(1-\cos^{2q+1}\theta)/(2q+1)} \tag{2.53}$$

Finally, the total efficiency η is equal to [124-126]:

$$\eta = \eta_{ill} \cdot \eta_{spill} \tag{2.54}$$

2.5.4 Analytical Model of Phase Compensator

An electric incident wave $\bar{E}_{in}$, characterized by arbitrary linear polarization, can be decomposed into its orthogonal linear components $E_{in,x}$ and $E_{in,y}$ according to [127]:

$$\bar{E}_{in} = E_{in,x}\hat{x} + E_{in,y}\hat{y} \tag{2.55}$$

When the electric incident wave $\bar{E}_{i,}$ hits a UC, the electric transmitted components $E_{out,x}$ and $E_{out,y}$ are related to the electric incident wave $\bar{E}_{in}$ via the transmission matrix T according to [127]:

$$\begin{pmatrix} E_{out,x} \\ E_{out,y} \end{pmatrix} = \begin{pmatrix} T_{xx} & T_{xy} \\ T_{yx} & T_{yy} \end{pmatrix} \begin{pmatrix} E_{in,x} \\ E_{in,y} \end{pmatrix} \tag{2.56}$$

where T_{xx}, T_{yy} are the co-polarized transmission coefficients, while T_{xy}, T_{yx} are the cross-polarized transmission coefficients. For a device operating in a DLP regime, the off-diagonal terms T_{xy}, T_{yx} should be null. For dual-polarized operation, the transmission matrix T simplifies to a diagonal matrix [127]:

$$T = \begin{pmatrix} |T_{xx}|e^{j\angle T_{xx}} & 0 \\ 0 & |T_{yy}|e^{j\angle T_{yy}} \end{pmatrix} \tag{2.57}$$

where $|T_{ii}|$, and $\angle T_{ii}$ are the modulus and the phase shifts applied to *x*- and *y*-polarized incident waves, respectively.

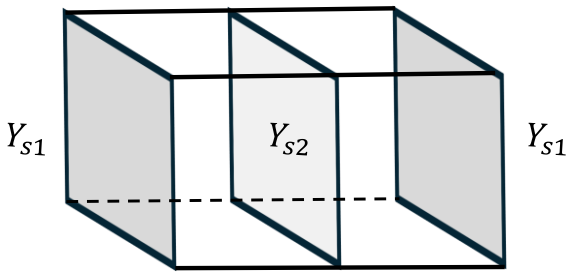

Figure 2.7 UC structure obtained from the cascade of three metallic layer and two dielectric substrates.

A symmetric geometry is chosen for each metallic layer to operate in the DLP regime. The method reported in [72] is employed to obtain the desired phase and

amplitude of the transmitted wave. The UC is composed of three metallic layers and two dielectric substrates, as shown in Fig. 2.7.

The desired phase and amplitude of the scattering parameter S_{21} can be obtained by changing the admittance Y_{s1} and Y_{s2} of the three metallic layers, namely Y_{s1} and Y_{s2} layers. For analytical modelling, the $ABCD$ matrix of the UC can be expressed as [70, 128]:

$$\begin{pmatrix} A & B \\ C & D \end{pmatrix} = \begin{pmatrix} 1 & 0 \\ Y_{s1} & 1 \end{pmatrix} \times \begin{pmatrix} \cos(\beta_d d) & j\eta_d \sin(\beta_d d) \\ j\dfrac{sin(\beta_d d)}{\eta_d} & \cos(\beta_d d) \end{pmatrix} \times \begin{pmatrix} 1 & 0 \\ Y_{s2} & 1 \end{pmatrix} \times \\ \times \begin{pmatrix} \cos(\beta_d d) & j\eta_d \sin(\beta_d d) \\ j\dfrac{sin(\beta_d d)}{\eta_d} & \cos(\beta_d d) \end{pmatrix} \times \begin{pmatrix} 1 & 0 \\ Y_{s1} & 1 \end{pmatrix} \tag{2.58}$$

where d, η_d and β_d are the thickness, the intrinsic impedance, and the phase constant of the dielectric substrate, respectively. The conversion from $ABCD$ parameters to scattering parameters S is given by [72, 128]:

$$\begin{pmatrix} S_{11} & S_{12} \\ S_{21} & S_{22} \end{pmatrix} = \begin{pmatrix} \dfrac{B/\eta_0 - C\eta_0}{2A + B/\eta_0 + C\eta_0} & \dfrac{2}{2A + B/\eta_0 + C\eta_0} \\ \dfrac{2}{2A + B/\eta_0 + C\eta_0} & \dfrac{B/\eta_0 - C\eta_0}{2A + B/\eta_0 + C\eta_0} \end{pmatrix} \tag{2.59}$$

where η_0 is the intrinsic impedance of free space. The phase delay ϕ of the transmitted wave through the UC and the image impedance Z_i of the UC structure are related to the scattering parameters S_{21} and S_{11} by [72, 128]:

$$\cos(\phi) = \frac{1 - S_{11}^2 + S_{21}^2}{2S_{21}} \tag{2.60}$$

$$Z_i = \pm\eta_0 \sqrt{\frac{(1 + S_{11})^2 - S_{21}^2}{(1 - S_{11})^2 - S_{21}^2}} \tag{2.61}$$

Finally, the admittance values Y_{s1} and Y_{s2} are related to the phase delay ϕ and the image impedance Z_i, by the following equation [72]:

$$Y_{s1} = \frac{j}{\eta_d \tan(\beta_d d)} - \frac{j}{Z_i \tan\left(\frac{\phi}{2}\right)} \tag{2.62}$$

$$Y_{s2} = j\frac{\left[-Z_i sin\left(\frac{\phi}{2}\right) - Z_i sin\left(\frac{3\phi}{2}\right) + 2\eta_d sin(2\beta_d d) cos\left(\frac{\phi}{2}\right)\right]}{2\eta_d^2 cos(\phi/2)\, sin^2(\beta_d d)} \tag{2.63}$$

2.5.5 Analytical Model of Partially Reflective Surface

The Dual Split Ring Resonator (DSRR), reported in [68] allows one to divide the magnitude of the incoming wave into two orthogonal components if suitably rotated with respect to the incident polarization. In fact, if the DSRR has a symmetry axis along $\alpha = 45°$ in a cartesian orthogonal system, a *x*-polarized (or *y*-polarized) incident wave generates two transmitted orthogonal waves polarized

along the *x*-axis and the *y*-axis with transmission amplitude $A = -6\,dB$ [68]. Fig. 2.8 shows the transmission amplitude of co-polarized components E_{out}^{x} (red curve) and the cross-polarized component E_{out}^{y} (black curve), when an *x*-polarized incident wave hits the DSRR with the parameters reported in [68]. Due to the symmetry of the structure, analogous behaviour is observed when a *y*-polarized wave hits the metamaterial.

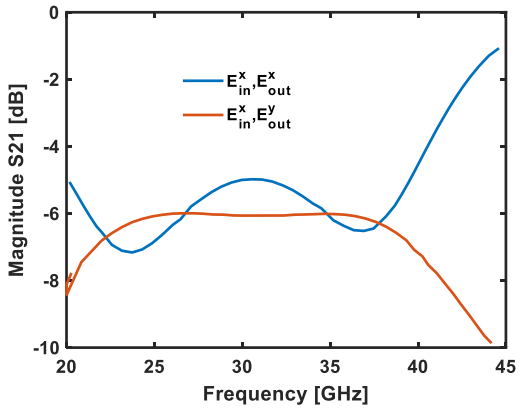

Figure 2.8 Co-polarized (blue curve) and cross-polarized (red curve) transmission magnitudes of the DSRR under an *x*-polarized incident wave excitation. Figure adapted from [68].

3 Mid-IR Laser and Amplifier Design

In this chapter, the design and optimization of a Mid-IR fiber laser and an optical fiber amplifier are presented, using a commercial single-mode praseodymium-doped fluoroindate fiber. The devices are designed and optimized to operate at the wavelength $\lambda_s = 4\ \mu m$, employing a six-level energy system, by taking into account experimental spectroscopic parameters. After the electromagnetic investigation of the fiber, the modelling of the devices has been performed via a home-made computer code solver, employing measured spectroscopic parameters. The validated code solves the rate equation and the power propagation equation considering the first- and second-order phenomena.

The simulations demonstrate very interesting results with reference to the state of the art and promise the fabrication of high beam quality optical sources and amplifiers based on a commercially available fiber, with the aim of proposing an all-in-fiber system operating in the Mid-IR range.

3.1 Model Validation

The home-made solvers used to design the fiber laser, and the optical fiber amplifier have been validated using the measured emission intensity I_e reported in [31] at signal wavelength $\lambda_s = 4\ \mu m$ for the bulk fluoroindate glass. The emission intensity I_e can be compared with the gain coefficient g_s [19, 31, 129]. For comparison purposes, both parameters are normalized with respect to their maximum value obtained at $N_{Pr} = 4000\ ppm$. The gain coefficient g_s has been calculated using equations (2.13) – (2.14) at signal wavelength $\lambda_s = 4\ \mu m$ for different concentrations of praseodymium N_{Pr}, and normalized. The gain coefficient g_s has been calculated by considering the absorption and emission cross section values reported in paragraph 3.2 and solving the rate equations.

Fig. 3.1 shows the measured normalized emission intensity $I_{e,norm}$ (red crosses) [31] and the simulated normalized gain coefficient $g_{s,norm}$ (blue circles) at signal wavelength $\lambda_s = 4\ \mu m$ as a function of the dopant concentration N_{Pr}. The figure shows a good agreement between the experimental data and the simulation results, confirming the accuracy of the proposed model. Similar solver codes, based on the rate equation approach and power propagation equations have been employed for the design of various optical devices [14, 16,19,37,130].

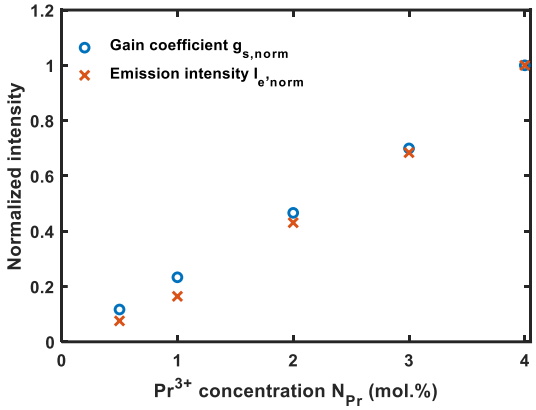

Figure. 3.1 Measured normalized emission intensity $I_{e,norm}$ (red crosses) and simulated normalized gain coefficient $g_{s,norm}$ (blue circles) at signal wavelength $\lambda_s = 4\ \mu m$ as a function of the dopant concentration N_{Pr} [99].

3.2 Modelling, Design and Numerical Analysis

The fiber laser and the optical fiber amplifier have been designed considering a double-cladding single-mode praseodymium-doped fluoroindate fiber, produced by Le Verre Fluoré, with a praseodymium concentration of $N_{Pr} = 8000\ ppm$ [131]. The fiber has a double cladding with the following geometric parameters: core diameter $d_{co} = 7.5\ \mu m$, inner cladding diameter $d_{cl1} = 125\ \mu m$, outer cladding diameter $d_{cl2} = 180\ \mu m$. The inner cladding has a D shape, obtained by making a cut at distance $d = 115\ \mu m$. The D-shape of the inner cladding is highly relevant to the device performance. Indeed, in perfectly circular fiber, a

significant portion of the pump propagates as skew rays, limiting the pump absorption. The D-shape breaks this symmetry, ensuring a higher absorption efficiency. The refractive index of the core n_{co}, inner cladding n_{cl1}, and outer cladding n_{cl2} at pump wavelength $\lambda_p = 1.55\ \mu m$ and signal wavelength $\lambda_s = 4\ \mu m$ is reported in Table 3.1, and has been taken from [131, 132]. According to the Le Verre Fluoré datasheet [131], the attenuation coefficient α depends on the wavelength; it is $0.08\ dB/m$ at the pump wavelength λ_p and $0.02\ dB/m$ at the signal wavelength λ_s.Table 3.1 reports also the attenuation coefficient for the pump and signal wavelength, equal to $\alpha = 0.2\ dB/m$. This value is higher than the actual one at the pump wavelength λ_p, thus chosen in precautionary way [131]. It is worth noting that higher propagation losses in the active fiber impact the laser performance by increasing the overall intracavity losses. This leads to a higher threshold power, a reduced slope efficiency, and a lower laser output power.

Fig. 3.2 shows the fiber cross-section geometry and the electric field norm $|E|$ of the fundamental mode HE_{11} at the signal wavelength λ_s. The FEM simulation confirms that the fiber is multimode at the pump wavelength λ_p. In particular, the LP_{01} and LP_{11} are both guided.

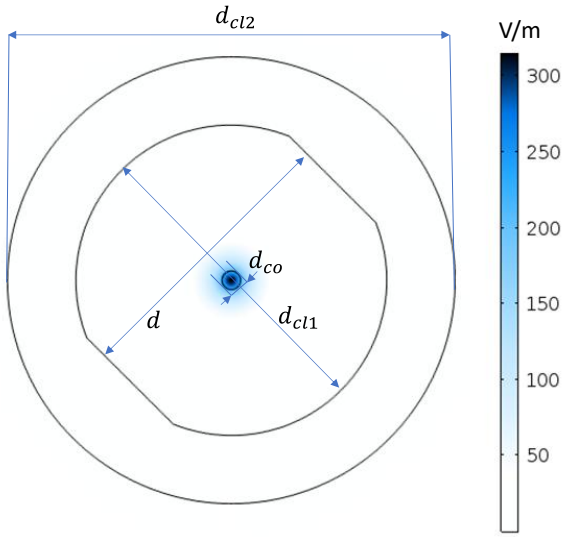

Figure. 3.2 Fiber cross-section geometry and the electric field norm $|E|$ of the fundamental mode HE_{11} at signal wavelength λ_S [24].

The electromagnetic investigation of the fiber has been performed via a Finite Element Method (FEM) software. In particular, the modal analysis of the fiber has been carried out to calculate the modal propagation constants, the electromagnetic field profiles, and the overlap coefficient for the pump Γ_p and the signal Γ_s. The fiber exhibits single-mode behavior at the signal wavelength $\lambda_s = 4\ \mu m$. The calculated pump overlap coefficient is $\Gamma_p = 0.899$ at wavelength $\lambda_p = 1.55\ \mu m$ and $\Gamma_s = 0.312$ at signal wavelength $\lambda_s = 4\ \mu m$. The overlap coefficient, around the central signal wavelength $\lambda_s = 4\ \mu m$, decreases almost linearly

TABLE 3.1 MODELING PARAMETERS EMPLOYED IN FEM SOFTWARE

Symbol	Value	Description
λ_p	$1550\ nm$	Pump wavelength
λ_s	$4000\ nm$	Signal wavelength
$\alpha(\lambda_{p,s})$	$0.2\ dB/m$	Glass attenuation at pump/signal wavelength
$n_{co}(\lambda_p)$	1.4881	Core refractive index at pump wavelength
$n_{co}(\lambda_s)$	1.4721	Core refractive index at signal wavelength
$n_{cl1}(\lambda_p)$	1.4746	Inner cladding refractive index at pump wavelength
$n_{cl1}(\lambda_s)$	1.4585	Inner cladding refractive index at signal wavelength
$n_{cl2}(\lambda_p)$	1.3872	Outer cladding refractive index at pump wavelength
$n_{cl2}(\lambda_s)$	1.3785	Outer cladding refractive index at signal wavelength

with the wavelength, from $\Gamma_s = 0.57$ at $\lambda_s = 3\ \mu m$ to $\Gamma_s = 0.21$ at $\lambda_s = 4.5\ \mu m$. Fig. 3.3 shows the absorption and emission cross section between the $F_{4,3} \rightarrow H_6$ levels (blue lines) and $G_4 \rightarrow F_{4,3}$ (black lines) levels for fluoroindate glass. The emission cross section (solid curves) is taken from literature [31], while the absorption cross sections (dashed curves) are calculated using the McCumber equation [31, 133]. The absorption cross-section calculated at the wavelength $\lambda_s = 4\ \mu m$ agrees with the value reported in [31].

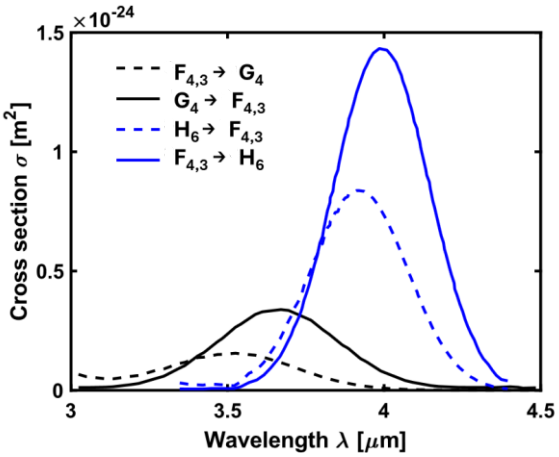

Figure. 3.3 Cross sections σ of Pr^{3+}:InF_3 glass as a function of the wavelength λ, for emission $F_{4,3} \rightarrow H_6$ (blue solid curve), and $G_4 \rightarrow F_{4,3}$ (black solid curve) [31], absorption $H_6 \rightarrow F_{4,3}$ (blue dashed curve), and absorption $F_{4,3} \rightarrow G_4$ (black dashed curve) calculated via McCumber equation [99].

The absorption cross section σ values for the pump between the $H_4 \rightarrow F_{4,3}$ levels, and the emission cross section for the ESA between the $G_4 \rightarrow H_5$ levels and the $D_2 \rightarrow G_4$ levels are taken from the literature [133-137]. The corresponding emission and absorption cross section σ are derived via the McCumber equation. Considering the absorption spectrum of Pr^{3+} ions [138], it can be observed that the effective pumping wavelength range is from 1.5 to 1.6 μm. At the boundaries of this band, the absorption is approximately 50% of the peak value, which is located at 1.55 μm.

The design has been performed with a home-made code solver, employing the spectroscopic parameters taken from the literature [31, 134, 138-140]. In the case of the fiber laser, the code solves the rate-equations system and power propagation equations for the pump, as well as for backward and forward components of the signal. In the case of the optical fiber amplifier, the code solves the rate-equations system and power propagation equations for the pump, the signal, and for the backward and forward ASE noise components.

Table 3.2 reports the spectroscopic parameters of the praseodymium-doped fluoroindate glass fiber employed for the six-level energy [31, 134, 138-140].

TABLE 3.2 SPECTROSCOPIC PARAMETERS: 6-LEVEL ENERGY DIAGRAM (PART I)

Symbol	Value	Description
$\sigma_{14}(\lambda_p)$	$1.2 \times 10^{-24}\ m^2$	Absorption cross section $H_4 \rightarrow F_{4,3}$
$\sigma_{41}(\lambda_p)$	$1.2 \times 10^{-24}\ m^2$	Emission cross section $F_{4,3} \rightarrow H_4$
$\sigma_{25}(\lambda_p)$	$2.0 \times 10^{-25}\ m^2$	Absorption cross section $H_5 \rightarrow G_4$
$\sigma_{52}(\lambda_p)$	$4.8 \times 10^{-25}\ m^2$	Emission cross section $G_4 \rightarrow H_5$
$\sigma_{34}(\lambda_s)$	$6.5 \times 10^{-25}\ m^2$	Absorption cross section $F_2, H_6 \rightarrow F_{4,3}$
$\sigma_{43}(\lambda_s)$	$14.4 \times 10^{-25}\ m^2$	Emission cross section $F_{4,3} \rightarrow F_2, H_6$
$\sigma_{45}(\lambda_s)$	$1.52 \times 10^{-25}\ m^2$	Absorption cross section $F_{4,3} \rightarrow G_4$
$\sigma_{45}(\lambda_s)$	$2.4 \times 10^{-25}\ m^2$	Emission cross section $G_4 \rightarrow F_{4,3}$
τ_6	$0.41\ ms$	Radiative lifetime D_2
τ_5	$2.35\ ms$	Radiative lifetime G_4
τ_4	$2.28\ ms$	Radiative lifetime $F_{4,3}$
τ_3	$57\ ms$	Radiative lifetime H_6
τ_2	$79\ ms$	Radiative lifetime H_5
A_{21}	$12.63\ s^{-1}$	Radiative rate $H_5 \rightarrow H_4$
A_{31}	$10.92\ s^{-1}$	Radiative rate $H_6 \rightarrow H_4$
A_{32}	$6.63\ s^{-1}$	Radiative rate $H_6 \rightarrow H_5$
A_{41}	$276.58\ s^{-1}$	Radiative rate $F_{4,3} \rightarrow H_4$

TABLE 3.2 SPECTROSCOPIC PARAMETERS: 6-LEVEL ENERGY DIAGRAM (PART II)

Symbol	Value	Description
A_{42}	$121.54\ s^{-1}$	Radiative rate$F_{4,3} \rightarrow H_5$
A_{43}	$40.53\ s^{-1}$	Radiative rate $F_{4,3} \rightarrow F_2, H_6$
A_{51}	$24.72\ s^{-1}$	Radiative rate $G_4 \rightarrow H_4$
A_{52}	$260.68\ s^{-1}$	Radiative rate $G_4 \rightarrow H_5$
A_{53}	$120.60\ s^{-1}$	Radiative rate $G_4 \rightarrow F_2, H_6$
A_{54}	$19.45\ s^{-1}$	Radiative rate $G_4 \rightarrow F_{4,3}$
A_{61}	$800\ s^{-1}$	Radiative rate $D_2 \rightarrow H_4$
A_{62}	$14\ s^{-1}$	Radiative rate $D_2 \rightarrow H_5$
A_{63}	$840\ s^{-1}$	Radiative rate$D_2 \rightarrow F_2, H_6$
A_{64}	$555\ s^{-1}$	Radiative rate $D_2 \rightarrow F_{4,3}$
A_{65}	$230\ s^{-1}$	Radiative rate$D_2 \rightarrow G_4$
W_{NR51}	$14514\ s^{-1}$	Non-radiative rate $G_4 \rightarrow H_4$
W_{NR43}	$7305\ s^{-1}$	Non-radiative rate $F_{4,3} \rightarrow H_6$
W_{NR32}	$6664\ s^{-1}$	Non-radiative rate $H_6 \rightarrow H_5$
W_{NR21}	$499987\ s^{-1}$	Non-radiative rate $H_5 \rightarrow H_4$
W_{CR1}	$1800\ s^{-1}$	Cross relaxation rate $H_4 \rightarrow F_{4,3}$, $G_4 \rightarrow H_5$
W_{CR2}	$2670 \times 10^4\ s^{-1}$	Cross relaxation rate $H_4 \rightarrow G_4$, $D_2 \rightarrow F_{4,3}$
W_{UP}	$47\ s^{-1}$	Up conversion rate $G_4 \rightarrow H_5$, $G_4 \rightarrow D_2$

3.3 Optical Laser Design and Discussion

In this chapter the Mid-IR optical laser based on praseodymium-doped fluoroindate fiber, employing a six-level energy scheme is presented. The simulations predict a slope efficiency η of about $\eta = 17.2\ \%$, and a pump power threshold P_{th} of about $P_{th} = 75\ mW$, when the fiber length L_{fiber} and output mirror reflectivity R_{out} are fixed at $L_{fiber} = 0.4\ m$ and $R_{out} = 50\ \%$, respectively.

3.3.1 Laser Design Employing 6-Level Energy Diagram

Numerical simulations have been carried out to study the laser output power P_s as a function of *i)* the fiber length L_{fiber}, and *ii)* the output mirror reflectivity R_{out}. The dopant concentration N_{Pr} is fixed at $N_{Pr} = 8000\ ppm$, while the input mirror reflectivity R_{in} is fixed at $R_{in} = 95\%$, representing a cautionary value to simulate a Fiber Bragg Grating (FBG) in an all-in-fiber setup. The fiber length L_{fiber} varies in the range $L_{fiber} = 0.3 \div 0.7\ m$, and the output mirror reflectivity R_{out} in the range $R_{out} = 30 \div 90\ \%$.

In the design of rare-earth-doped fiber devices, the accuracy of the model is crucial. It should take into account all the phenomena occurring in the real glass to ensure a realistic simulation of the device and be based on experimental spectroscopic parameters. The inclusion of ESA phenomena corresponding to the $H_5 \rightarrow G_4$ levels, and $G_4 \rightarrow D_2$ levels; as well as the second-order phenomena, such as the first CR phenomenon involving the $D_2 \rightarrow F_4$ and $H_4 \rightarrow G_4$ levels, the

second CR phenomenon involving the $G_4 \rightarrow H_5$ and $H_4 \rightarrow F_4$ levels, and the UP phenomenon between $G_4 \rightarrow D_2$ and $G_4 \rightarrow H_5$, enhances the accuracy of the model.

Fig. 3.4 shows the laser output power P_s as a function of the input pump power P_p, for different values of the fiber length L_{fiber}, with the output mirror reflectivity fixed at $R_{out} = 80\%$. The simulations show that the saturation pump power P_{sat} increases when the fiber length L_{fiber} increases. The simulations also show that a maximum laser output power $P_s = 303\ mW$ is achieved for a fiber length of $L_{fiber} = 0.7\ m$. On the other hand, the slope efficiency η slightly reduces as the fiber length L_{fiber} increases. The best slope efficiency $\eta = 14.8\%$ is obtained for $L_{fiber} = 0.3\ m$, limiting the maximum laser output power to $P_s = 135\ mW$. To find a trade-off, for a fiber length $L_{fiber} = 0.4\ m$, laser output power $P_s = 183\ mW$ and slope efficiency $\eta = 14.3\%$ have been chosen. For this case the pump power threshold is $P_{th} = 25\ mW$.

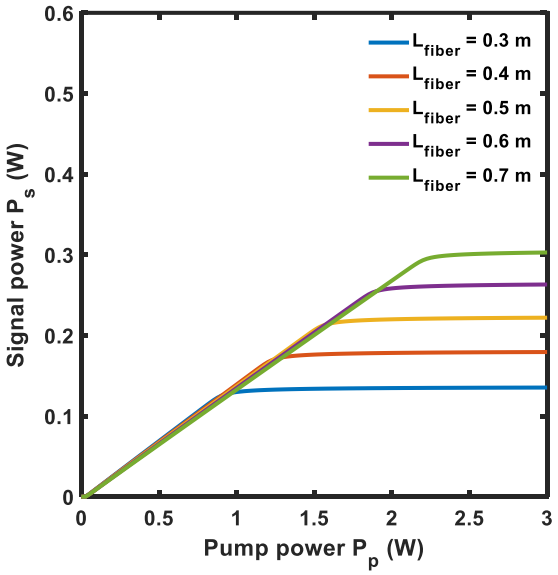

Figure. 3.4 Laser output power P_s versus input pump power P_p, for different values of the fiber length L_{fiber}, with input mirror reflectivity fixed at $R_{in} = 95\%$, and output mirror reflectivity at $R_{out} = 80\%$ [141].

Fig. 3.5 shows the laser output power P_s as a function of the input pump power P_p, for different values of the output mirror reflectivity R_{out}, with the fiber length fixed at $L_{fiber} = 0.4\,m$. As the output mirror reflectivity R_{out} decreases, the maximum laser output power P_s and the slope efficiency η increase, for the same saturation pump power P_{sat}, but the pump power threshold P_{th} increases too.

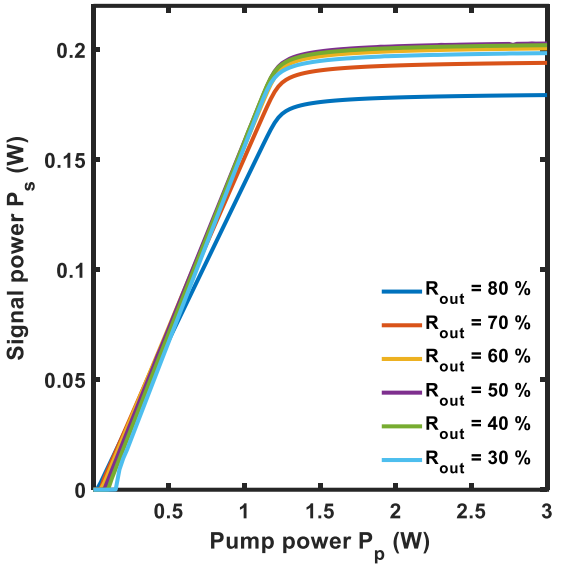

(a)

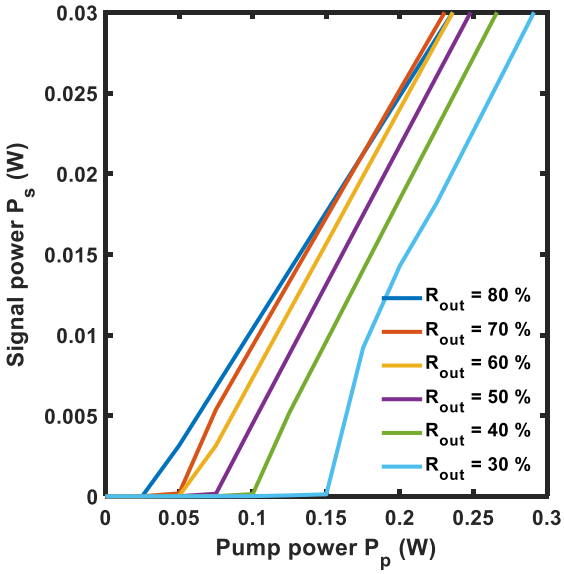

(b)

Figure. 3.5 (a) Laser output power P_s versus input pump power P_p, for different values of the output mirror reflectivity R_{out}, with input mirror reflectivity fixed at $R_{in} = 95\%$, and fiber length at $L_{fiber} = 0.4\ m$; (b) Enlarged view of the pump power threshold P_{th} [141].

The maximum laser output power $P_s = 204\ mW$ is obtained for $R_{out} = 30\ \%$, with a corresponding slope efficiency $\eta = 18\ \%$ and pump power threshold $P_{th} = 150\ mW$. To reduce the pump power threshold to $P_{th} = 75\ mW$, an output mirror reflectivity of $R_{out} = 50\ \%$ can be chosen, corresponding to a laser output power $P_s = 202\ mW$ and slope efficiency $\eta = 17.2\ \%$.

The numerical simulations presented in this section do not include a dedicated thermal model. The laser device is assumed to operate under ideal and isothermal conditions. Under high power operation, an adequate cooling system can be investigated in future experimental validation.

3.3.2 Comparison with State of the Art

Table 3.3 reports a comparison between the Pr^{3+}-doped fluoroindate fiber laser proposed in this work and other fluoroindate fiber lasers emitting in the Mid-IR [13-15,17-19, 22, 141]. In particular, the comparison with literature is performed in terms of doping ion, emission signal wavelength λ_s, pump wavelength λ_p, pump power threshold P_{th}, and slope efficiency η. The lasers reported in Table 3.3 emit between $\lambda_s = 3.4\ \mu m$ and $\lambda_s = 4.4\ \mu m$, when they are pumped in the visible or near-infrared (NIR) range. The lasers reported in [13,17,18] propose dual-wavelength pumping schemes to increase the slope efficiency and to reduce the pump power threshold. In comparison with the state-of-the-art of fiber lasers based on fluoroindate glasses, the designed fiber lasers, employing six-levels

energy system, exhibit a good slope efficiency and a low pump power threshold P_{th}, while achieving one of the longest emission wavelengths λ_s, using a single-wavelength pumping scheme. The use of a single- wavelength pumping scheme simplifies the construction of the laser system. The proposed optical laser, based on a commercially available praseodymium-doped fiber, can be pumped by a commercial erbium-doped fiber laser, and can be spliced to FBGs used as cavity mirrors, obtaining an all-in-fiber device.

TABLE 3.3 COMPARISON OF MID-IR OPTICAL LASERS BASED ON InF^3 FIBERS

Refer	**Dopant**	**Signal wavelength λ_s**	**Pump wavelength λ_p**	**Pump power threshold**	**Slope efficiency**
[13]	Er^{3+}	3.44 μm	972 nm 1976 nm	–	19 %
[14]	Er^{3+}	3.91 μm	635 nm	25 mW	1.6 %
[15]	Ho^{3+}	3.92 μm	888 nm	4.3 W	10.2 %
[17]	Ho^{3+}	3.92 μm	888 nm 962 nm	–	19 %
[18]	Ho^{3+}	3.92 μm	888 nm 1660 nm	2 W	12.1 %
[19]	Ho^{3+}/ Nd^{3+}	3.92 μm	808 nm	200 mW	16.7 %
[22]	Dy^{3+}	3.3 μm 4.4 μm	1700 nm	30 W	27 %
This work	Pr^{3+}	4 μm	1550 nm	75 mW	17.2 %

3.4 Optical Fiber Amplifier and Discussion

In this paragraph, a Mid-IR optical fiber amplifier based on praseodymium-doped fluoroindate fiber, employing the same energy system is presented. The designed optical amplifier is very promising, exhibiting high simulated gain $G = 32.6\ dB$ and a wide -3dB bandwidth of $BW_g = 115\ nm$ with noise figure $NF = 6\ dB$ around the central signal wavelength $\lambda_s = 4\ \mu m$, for input pump power $P_p = 2W$, input signal power $P_s = -30\ dBm$, and pump wavelength $\lambda_p = 1.55\ \mu m$. In the design of the optical amplifier, several simulations have been performed. Gain G and noise figure NF have been investigated as function of input signal power P_s, input pump power P_p, fiber length L_{fiber}, and signal wavelength λ_s. The pump wavelength λ_p is fixed at $\lambda_p = 1.55\ \mu m$, in order to consider a low-cost feeding diode intended for pumping an erbium doped fiber laser. The dopant concentration is fixed at $N_{Pr} = 2000\ ppm$. For the laser design, the Praseodymium concentration proposed by the Le Verre Fluoré catalog is considered. Conversely, for the optical amplifier, a lower concentration and a longer fiber are preferred because the simulations show that the noise figure improves. Fig. 3.6 reports the trend of gain G as a function of input signal power P_s for different values of input pump power $P_p = 0.5\ W$ (solid curve), $P_p = 1\ W$ (dashed curve), $P_p = 2\ W$ (dot-dashed curve) and $P_p = 3\ W$ (dotted curve), with the fiber length fixed at $L = 3\ m$, and the signal wavelength at $\lambda_s = 4\ \mu m$.

The saturation input signal power $P_{s,sat}^{in}$, limiting the amplifier linear behavior, is defined as the input signal power where the gain G drops by $-3dB$ below its unsaturated value [14, 129]. It decreases with increasing the input pump power P_p, resulting $P_{s,sat}^{in} = 8\ dBm$, $P_{s,sat}^{in} = -1.5\ dBm$, $P_{s,sat}^{in} = -14.7\ dBm$, and $P_{s,sat}^{in} = -14.8\ dBm$, for the input pump power of $P_p = 0.5\ W$, $P_p = 1\ W$, $P_p = 2\ W$, and $P_p = 3\ W$, respectively.

Fig. 3.7 reports the trend of gain G as a function of input signal power P_s for different values of fiber length $L = 1\ m$ (solid curve), $L = 2\ m$ (dashed curve), and $L = 3\ m$ (dot-dashed curve), with the input pump power fixed at $P_p = 2\ W$. The saturation input signal power decreases as the fiber length L increases. Since the behaviour becomes linear for $L > 3\ m$, a fiber length $L = 3\ m$ has been selected as the upper limit, and an input signal power of $P_s = -30\ dBm$ has been chosen in order to work in linear small-signal regime.

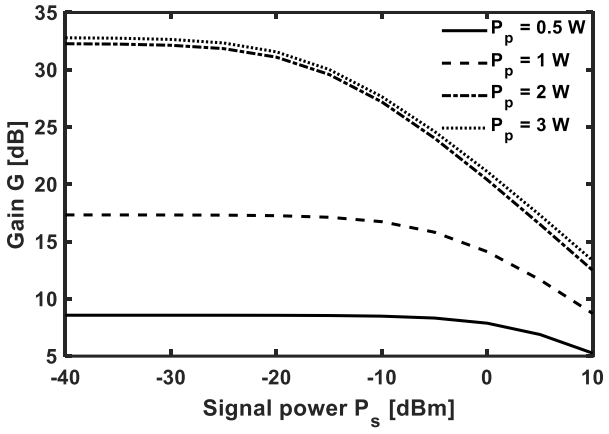

Figure. 3.6 Gain G versus input signal power P_s, for different values of input pump power P_p, with fiber length fixed at $L = 3\ m$, and signal wavelength at $\lambda_s = 4\ \mu m$ [99].

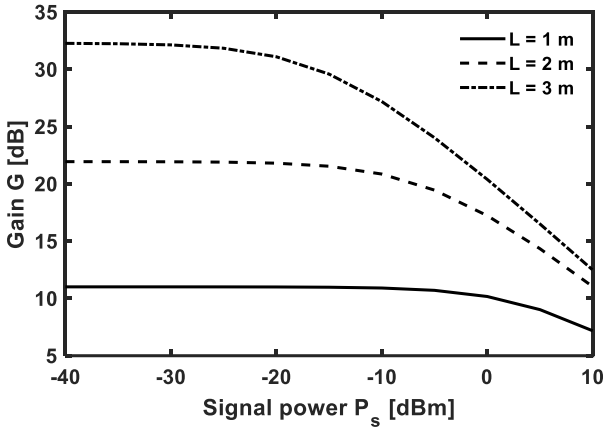

Figure 3.7 Gain G versus input signal power P_s, for different values of fiber length L, with the input pump power fixed at $P_p = \ 2\ W$, and signal wavelength at $\lambda_s = 4\ \mu m$ [99].

Fig. 3.8 reports the trend of gain G as a function of input pump power P_p for different values of fiber length $L = 1\ m$, (solid curve), $L = 2\ m$ (dashed curve), $L = 3\ m$ (dot-dashed curve), with the input signal power fixed at $P_s = -30\ dBm$. There are three pumping ranges: the under-pumped regime ($P_p < P_{p,inv}$) where the population inversion is not reached, the non-complete inversion regime ($P_p > P_{p,inv}$), and the complete inversion regime ($P_p \gg P_{p,inv}$) [133, 142, 143]. The simulations show that for a fiber length of $L = 1\ m$, the minimum pump power required to operate in the complete inversion regime is $P_p = 0.6\ W$.

Fig. 3.9 reports the trend of gain G as a function of fiber length L for different values of the input pump power $P_p = 0.5\ W$ (solid curve), $P_p = 1\ W$ (dashed curve), $P_p = 2\ W$ (dot-dashed curve), and $P_p = 3\ W$ (dotted curve), with the input signal power fixed at $P_s = -30\ dBm$. The gain reaches a maximum value and then slightly decreases for increasing fiber length.

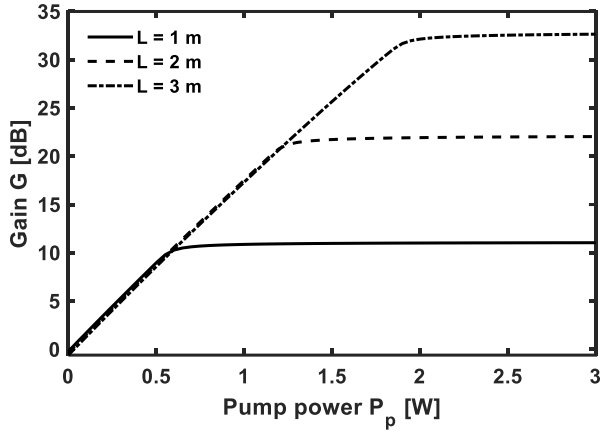

Figure 3.8 Gain G versus input pump power P_p, for different values of fiber length L, with the input signal power fixed at $P_s = -30\ dBm$, and signal wavelength at $\lambda_s = 4\ \mu m$ [99].

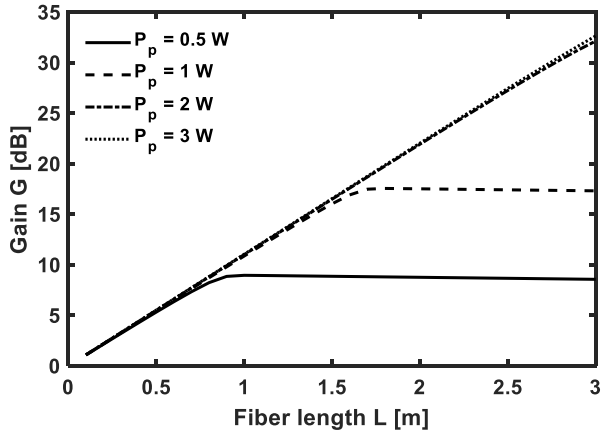

Figure 3.9 Gain G versus fiber length L, for different values of input pump power P_p, with the input signal power fixed at $P_s = -30\ dBm$, and signal wavelength at $\lambda_s = 4\ \mu m$. [99].

Fig. 3.10 reports the trend of (a) the gain G and (b) the noise figure NF as a function of the input signal wavelength λ_s for different values of the input pump power $P_p = 0.5\,W$ (solid curve), $P_p = 1\,W$ (dashed curve), $P_p = 2\,W$ (dot-dashed curve), and $P_p = 3\,W$ (dotted curve), with the fiber length fixed at $L = 3\,m$. At the central wavelength $\lambda_s = 4\,\mu m$, the maximum gain value is $G = 8.57\,dB$, $G = 17.32\,dB$, $G = 32.6\,dB$, and $G = 32.65\,dB$, when the input pump power is $P_p = 0.5\,W$, $P_p = 1\,W$, $P_p = 2\,W$, and $P_p = 3\,W$, respectively. Fig. 3.10 (a) shows that as the input pump power P_p increases from $P_p = 0.5\,W$ to $P_p = 3\,W$, the bandwidth calculated at $-3\,dB$, around the central wavelength $\lambda_s = 4\,\mu m$, narrows from $BW_G = 220\,nm$ to $BW_G = 95\,nm$.

Fig. 3.10 (b) shows that the noise figure NF decreases in the range $\lambda_s = 3.7 - 4.5\,\mu m$, and that for a fixed wavelength λ, as the input pump power P_p increases, the noise figure NF increases. In the wavelength range $\lambda_s = 3.5 - 3.8\,\mu m$, the spontaneous emission phenomenon between the levels $G_4 \rightarrow F_{4,3}$ dominates over other phenomena, and this increases the noise figure in this range. In the wavelength range $\lambda_s = 3.8 - 4.2\,\mu m$, the noise figure is about $NF = 6.3\,dB$. In the wavelength range $\lambda_s = 4.2 - 4.5\,\mu m$, the noise figure NF is less than the quantum limit ($NF < 3dB$) [133, 142, 143].

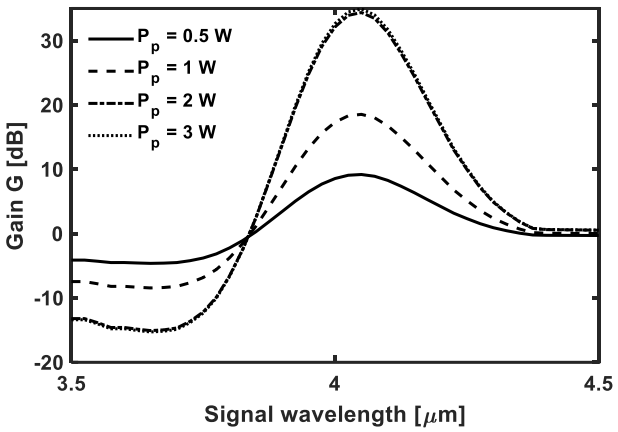

(a)

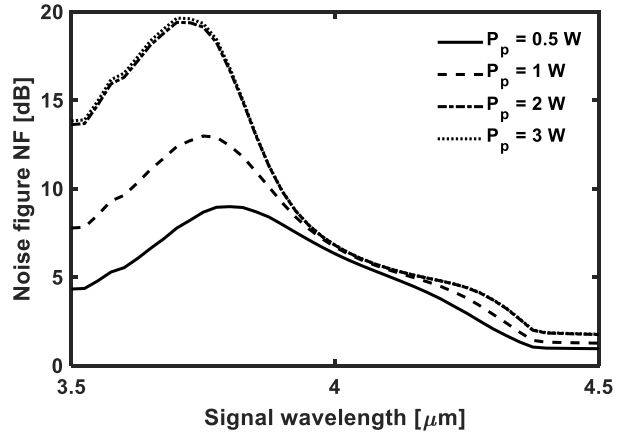

(b)

Figure. 3.10 (a) Gain G, and (b) noise figure NF versus input signal wavelength λ_s, for different values of the input pump power P_p, with the input signal power fixed at $P_s = -30\ dBm$, and fiber length at $L = 3\ m$ [99].

Fig. 3.11 reports the trend of (a) the gain G, and (b) the noise figure NF as function of input signal wavelength λ_s for different fiber lengths $L = 1\,m$ (solid curve), $L = 2\,m$ (dashed curve), and $L = 3\,m$ (dot-dashed curve). An input pump power $P_p = 2\,W$ is chosen in order to work with complete population inversion. At the central wavelength $\lambda_s = 4\,\mu m$, the maximum gain is $G = 11\,dB$, $G = 21.93\,dB$,and $G = 32.14\,dB$, when the fiber length is $L = 1\,m$, $L = 2\,m$, and $L = 3\,m$, respectively.

Fig. 3.11 (a) shows that as the fiber length L increases from $L = 1\,m$ to $L = 3\,m$, the bandwidth calculated at $-3\,dB$ around the central wavelength $\lambda_s = 4\,\mu m$, narrows from $BW_G = 165\,nm$ to $BW_G = 110\,nm$.

Fig. 3.11 (b) shows that the noise figure NF decreases in the range $\lambda_s = 3.7 - 4.5\,\mu m$. A gain of $G > 30\,dB$ is achieved in a wavelength range of over $B = 130\,nm$ with noise figure $NF = 6\,dB$.

The optimized amplifier exhibits a gain of $G = 32.6\,dB$, a bandwidth calculated at $-3dB$ around a central wavelength $\lambda_S = 4\,\mu m$, of $BW_G = 115\,nm$, and maintains a small signal regime up to an input signal power of $P_s^{in} = -14.7\,dBm$, when the input pump power P_P and the fiber length L are fixed at $P_p = 2\,W$ and $L = 3\,m$, respectively.

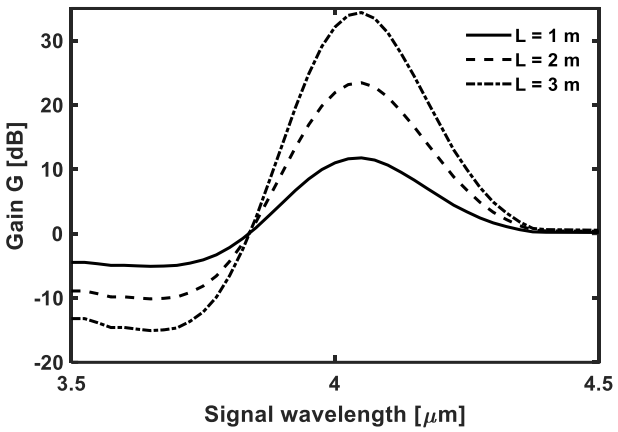

(a)

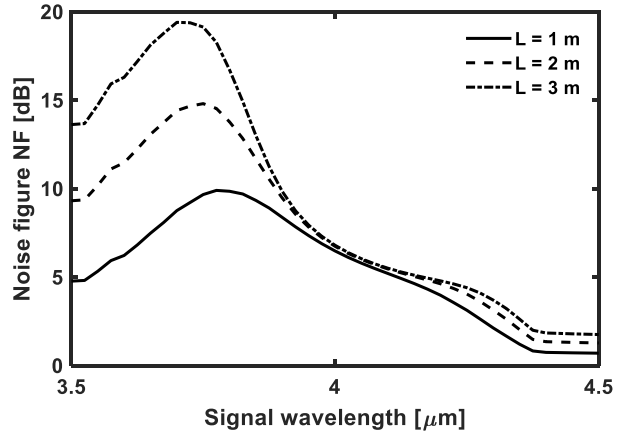

(b)

Figure. 3.11 (a) Gain G, and (b) noise figure NF versus input signal wavelength λ_s, for different values of the fiber length L, with the input signal power fixed at $P_s = -30\ dBm$, and input pump power at $P_p = 2\ W$ [99].

3.4.1 Comparison with State of the Art

Table 3.4 reports a comparison between the optical fiber amplifier proposed in this work, and other optical amplifiers taken from literature [32-38, 144, 145]. The comparison takes into account the dopant ion, the pump wavelength λ_p, the central emission wavelength λ_s, the input pump power P_p, the input signal power P_s, the gain G, and the bandwidth BW_G, calculated at $-3dB$ around a central wavelength λ_s. In comparison with state-of-the-art fluoride amplifiers, the proposed device exhibits one of the broadest bandwidths, the lowest pump power, high gain, and a higher operating central emission wavelength λ_s. Amplification at comparable central emission wavelengths λ_s is achieved exclusively using chalcogenide fibers which require much higher input pump powers.

TABLE 3.4 COMPARISON OF MID-IR OPTICAL FIBER AMPLIFIERS

Refer	**Glass**	**Dopant**	**Pump** λ_p	**Central** λ_s	**Input Pump** P_p	**Input Signal** P_s	**Gain** G	**Bandwidth** BW_G
[32]	ZBLAN	Er^{3+}	$0.98\mu m$	$2.7\ \mu m$	$12.5\ W$	$\sim 18\ dBm$	$\sim 15.4\ dB$	$250\ nm$
[33]	ZFG	Er^{3+}	$0.98\ \mu m$	$2.8\ \mu m$	$9.63\ W$	$\sim 13\ dBm$	$> 20\ dB$	$95\ nm$
[34]	ZFG	Er^{3+}	$0.98\ \mu m$	$2.79\ \mu m$	$5.8\ W$	$\sim 7.2\ dBm$	$20\ dB$	$22\ nm$
[35-36]	Chalc.	Pr^{3+}	$1.55\ \mu m$	$4.3\ \mu m$	$0.37\ W$	$-20\ dBm$	$> 30\ dB$	#
[36]	Chalc.	Dy^{3+}	$1.3\ \mu m$	$4.4\ \mu m$	$0.26\ W$	$-13\ dBm$	$> 15\ dB$	#
[36]	Chalc.	Tb^{3+}	$2.0\ \mu m$	$4.9\ \mu m$	$0.28\ W$	$-13\ dBm$	$> 25\ dB$	#
[37]	Chalc.	Dy^{3+}	$1.71\ \mu m$	$4.4\ \mu m$	$3\ W$	$0\ dBm$	$28\ dB$	#
[38]	Chalc.	Er^{3+}	$0.98\ \mu m$	$2.8\ \mu m$	$0.1\ W$	$-50\ dBm$	$33.7\ dB$	#
[144]	Fluoride	Dy^{3+}	$2.91\mu m$	$3.24\ \mu m$	$10.96\ W$	$\sim 5.6\ dBm$	$< 10\ dB$	#
[145]	Fluoride	Er^{3+}	$0.98\ \mu m$	$2.78\ \mu m$	12 W	$\sim 7.1\ dBm$	$\sim 7.1\ dB$	$60\ nm$
This work	InF_3	Pr^{3+}	$1.55\ \mu m$	$4.0\ \mu m$	$2\ W$	$-30\ dBm$	$> 30\ dB$	$130\ nm$

* The gain bandwidth BW_G is defined at $-3dB$ for [32, 33, 34] and for the proposed Mid-IR Optical Amplifier.
**The gain bandwidth BW_G is defined at $-20dB$ for [145].

3.5 Conclusion

A Mid-IR fiber laser and an optical fiber amplifier based on a praseodymium-doped fluoroindate glass, operating at wavelength $\lambda_s = 4\ \mu m$, when pumped at $\lambda_p = 1550\ nm$, have been designed and optimized, by considering spectroscopic parameters taken from the literature. Compared to state-of-the-art fluoroindate fiber lasers, the designed lasers, based on six-level energy diagrams, exhibit a good slope efficiency η and a low pump power threshold P_{th} while achieving one of the longest emission wavelengths λ_s, via a single-wavelength pumping scheme. Specifically, the six-level model shows a slope efficiency $\eta = 17.2\ \%$, and a pump power threshold $P_{th} = 75\ mW$.

Furthermore, the performance of the optical fiber amplifier has been investigated as a function of different input parameters. It proves high gain $G = 32.1\ dB$, a noise figure $NF = 6 \pm 0.2\ dB$ and a wide bandwidth $BW_G = 130\ nm$, when the input pump power P_p, the fiber length L and input signal power P_s are set to $P_p = 2\ W$, $L = 3\ m$, and $P_s = -30\ dBm$, respectively. NIR pumping for both devices can be implemented using a commercial erbium-doped fiber laser, spliced to the praseodymium fluoroindate fiber, obtaining an all-in-fiber device operating in Mid-IR range.

4 Mid-IR ZBLAN Fiber Temperature Sensor

In this chapter, the design, a fabrication and characterization of optical fiber sensors operating in the Mid-IR are presented, using a commercial ZBLAN optical fiber. The design is carried out via Finite Element Method (FEM) and Beam Propagation Method (BPM) software tools, while the fabrication is performed using the pulling and heating technique with a Vytran GPX-2400 glass processing station. The characterization of the non-adiabatic tapering demonstrates good agreement with the simulations, suggesting good potential for the next generation of optical fiber sensors operating in the Mid-IR.

4.1 Non-Adiabatic Taper Design and Analysis

The non-adiabatic taper design employs a single-mode ZBLAN optical fiber, model ZFG SM [1.95] 6.5/125 produced by Le Verre Fluoré (Bruz, France) [146]. The core and cladding diameters are $d_{co} = 6.5\ \mu m$, and $d_{cl} = 125\ \mu m$, respectively. The core and cladding refractive indices are $n_{co} = 1.4954$, and $n_{cl} = 1.4776$, respectively. A 3D-BPM simulation is exploited to calculate the sensor output spectrum. The mesh grid size is set to $M_x = M_y = 0.25\ \mu m$ for

the optical fiber cross-section and $M_z = 0.5\ \mu m$ is set for the longitudinal direction. To obtain a non-adiabatic transition, the designed down-taper L_{dt} and the up-taper L_{ut} lengths are $L_{dt} = L_{ut} = 2\ mm$ (refer to Fig. 2.3). Moreover, to prevent the adjacent minima of the interferogram from being too close, the designed waist length is $L_w \simeq 8\ mm$ [147, 148]. The simulations are here reported for $L_w = 8.05\ mm$, according to the fabricated proof of concept and the experimental findings. The waist diameter is $d_w = 25\ \mu m$. By means of a pathway monitor, the excitation of the LP_{02} mode in the down-taper region is verified.

Fig. 4.1 reports the normalized output power P_{out} as a function of the wavelength λ for different temperature changes $\Delta T = 0\ K$ (solid curve), $\Delta T = 50\ K$ (dashed curve), and $\Delta T = 100\ K$ (dot-dashed curve). A blueshift of the dips is observed with increasing temperature T, and the simulated temperature sensitivity at the wavelength $\lambda \simeq 3310$ nm is $S_T = -85.3$ pm/K. This value has been calculated as the ratio between the wavelengths λ where the normalized output power $P_{out} = 1$ and the associated temperature variation ΔT.

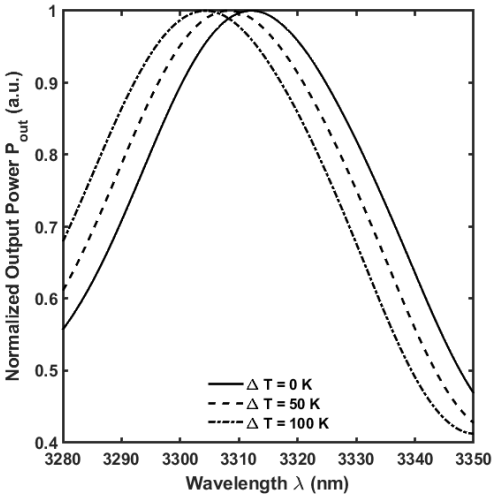

Figure. 4.1 Normalized output power P_{out} as a function of the wavelength λ for different temperature changes $\Delta T = 0\ K$ (solid curve), $\Delta T = 50\ K$ (dashed curve), and $\Delta T = 100\ K$ (dot-dashed curve), simulated via BPM software [7].

The temperature sensitivity is affected by the thermo-optic effect and the thermal expansion coefficient [48]. In particular, the refractive index change is given by $\delta n = dn/dT\ \times \Delta T$, while the length change is given by $\delta L = \alpha L \Delta T$ [149]. The quantities dn/dT, α, and ΔT are the thermo-optic coefficient, the thermal expansion coefficient, and the temperature variation ΔT, respectively [150].

For the zirconium fluoride glass, the thermo-optic coefficient is $dn/dT = -1.475 \times 10^{-5}\ K^{-1}$, and the thermal expansion coefficient is $\alpha = 1.72 \times 10^{-5}\ K^{-1}$ [151]. For the silica glass the thermo-optic coefficient is $dn/dT = 1.2 \times 10^{-5}\ K^{-1}$ and the thermal expansion coefficient is $\alpha = 5.5 \times 10^{-7}\ K^{-1}$

[152]. The blueshift of the spectral response, reported in Fig. 4.1, appears counterintuitive with respect to the attenuation peak λ_m of the *m*-th Mach-Zehnder interference, expressed as $\lambda_m = \left(2 \times \Delta n_{eff} \times L\right)/(2m + 1)$ [46], especially considering the high positive coefficient of thermal expansion α that increases the waist length L. [48, 49]. In silica tapers, the red shift of the *m*-th interference dip is generally explained in terms of the positive variation of Δn_{eff} and of the length L, which is small due to the low thermal expansion coefficient α [48-50,153]. Furthermore, in silica optical fiber SMF-28 at the wavelength $\lambda \simeq 1550\, nm$, FEM simulations show that the positive thermo-optic coefficient dn/dT leads to a lower value of Δn_{eff} with temperature increasing. Therefore, a deeper electromagnetic analysis using a commercial FEM software is performed to better understand the described effect, and to predict the behaviour of the comb-like output spectral pattern as a function of temperature variation ΔT. The 2-D electromagnetic modal analysis simulation is computed in the waist region of the commercial optical fiber, produced by Le Verre Fluoré [146]. The core diameter d_{co} and cladding diameter d_w in the waist section are $d_{co} = 1.3\, \mu m$, and $d_w = 25\, \mu m$ respectively. The simulation considers temperature variations $\Delta T = 0\, K$, $\Delta T = 50\, K$, $\Delta T = 100\, K$, in the wavelength range from $\lambda = 3280\, nm$ to $\lambda = 3350\, nm$, with a step of $\Delta\lambda = 0.1\, nm$. The effective refractive indices n_{eff} of the fundamental LP_{01} and of the cladding mode LP_{02} are

calculated considering the influence of the fluoride glass thermo-optic coefficient dn/dT on the core and cladding refractive indices.

Fig. 4.2 reports the simulated effective refractive index difference Δn_{eff} between the LP_{01} mode and the LP_{02} mode as a function of the wavelength λ for different temperature changes $\Delta T = 0\ K$ (solid curve), $\Delta T = 50\ K$ (dashed curve), $\Delta T = 100\ K$ (dot-dashed curve). The effective refractive index difference Δn_{eff} between the LP_{01} mode and the LP_{02} mode increases with temperature T. The inset shows the normalized electric field norm *E* is reported for *x*-polarized and *y*-polarized components of both modes at the wavelength $\lambda = 3.34\ \mu m$, and the temperature variation $\Delta T = 0\ K$.

Fig. 4.3 reports the phase delay ϕ of the modes as a function of the wavelength λ for different temperature changes $\Delta T = 0\ K$ (solid curve), $\Delta T = 50\ K$ (dashed curve), $\Delta T = 100\ K$ (dot-dashed curve). The phase delay is influenced by two factors: *i)* the variation of the effective refractive index difference Δn_{eff} between the LP_{01} mode and the LP_{02} mode with temperature changes, and *ii)* the change in length of the waist region *L* due to the fluoride glass thermal expansion coefficient α.The spectral positions of the minima are determined by satisfying the phase condition $\phi = 2\pi/\lambda \times \Delta n_{eff} \times L = (2m + 1)\pi$. Graphically, the intersection between the horizontal line $\phi = (2m + 1)\pi$ and the curve $\phi = 2\pi/\lambda \times \Delta n_{eff} \times L$ shifts to shorter wavelengths λ, i.e. blueshift, for increasing temperature *T*.

The formula shows that an increase in both the effective refractive index difference Δn_{eff} and fiber length L, the latter depending on a positive expansion coefficient α, creates an increase of the phase ϕ for a positive temperature variation. Qualitatively, Fig. 4.2 shows that the negative thermo-optic coefficient of the ZBLAN glass modifies the modal effective indices. By keeping the fiber length fixed at the initial condition (i.e. $L_0 = 8mm$), the differential effective index Δn_{eff} increases from $1.388 \cdot 10^{-2}$ to $1.389 \cdot 10^{-2}$ when the temperature difference changes from $\Delta T = 0\ K$ to $\Delta T = 100\ K$. According to the formula of the phase ϕ, considering an initial fiber length $L_0 = 8\ mm$, this variation produces a phase increase $\Delta\phi = 0.152\ rad$. Moreover, when the temperature difference changes from $\Delta T = 0\ K$ to $\Delta T = 100\ K$, the fiber undergoes a physical elongation of $\Delta L = L_0 \cdot a \cdot \Delta T = 13.76\ \mu m$ due to the thermal expansion effect α. This elongation causes an overall phase increase of $\Delta\phi = 2\pi/\lambda \times \Delta n_{eff} \times \Delta L = 0.364\ rad$. Finally, Fig. 4.3 confirms that the phase increases from $212.7\ rad$ to $213.3\ rad$ when the temperature difference changes from $\Delta T = 0\ K$ to $\Delta T = 100\ K$, demonstrating the overall phase shift when the two effects work together.

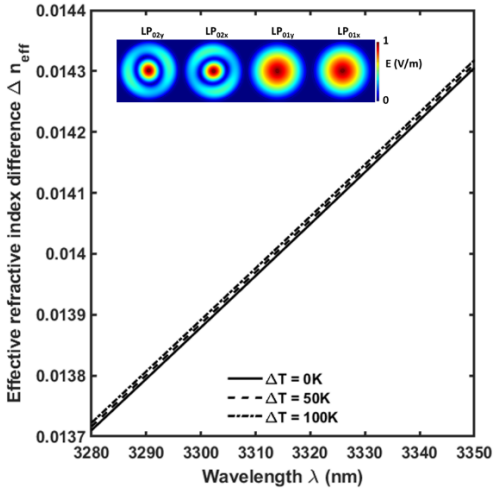

Figure. 4.2 Effective refractive index difference Δn_{eff} between the LP_{01} mode and the LP_{02} mode as a function of the wavelength λ for temperature changes $\Delta T = 0\ K$ (solid curve), $\Delta T = 50\ K$ (dashed curve), $\Delta T = 100\ K$ (dot-dashed curve), simulated via FEM software. Inset: normalized electric field distribution (E-norm) for x-polarized and y-polarized components of both modes at the wavelength $\lambda = 3.34\ \mu m$, and the temperature variation $\Delta T = 0\ K$, simulated via FEM software [7].

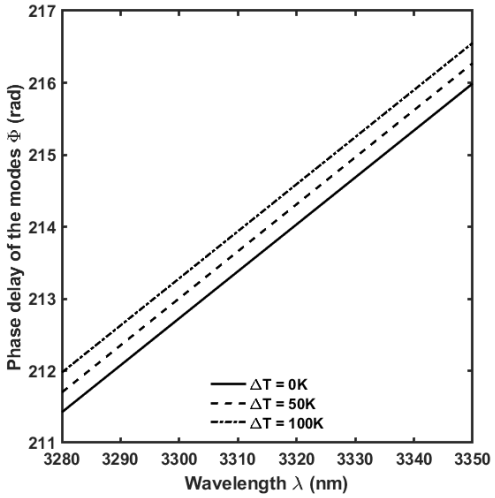

Figure. 4.3 Phase delay of the modes ϕ as a function of the wavelength λ for different temperature changes $\Delta T = 0\ K$ (solid curve), $\Delta T = 50\ K$ (dashed curve), and $\Delta T = 100\ K$ (dot-dashed curve), simulated via FEM software [7].

Fig. 4.4 reports the cosine of the phase delay ϕ as a function of the wavelength λ for different temperature changes ΔT=0 K (solid curve), ΔT=50 K (dashed curve), ΔT=100 K (dot-dashed curve). Fig. 4.4 confirms a blueshift of the output comb-like spectral pattern. Specifically, if a positive temperature change is considered in zirconium fluoride glass*: i)* the negative thermo-optic coefficient dn/dT leads to an increase of the effective refractive index difference Δn_{eff} between both modes; and *ii)* the positive thermal expansion coefficient α leads to an increase of the cavity length L. Both these effects cause the simulated blueshift. The simulated temperature sensitivity, calculated at the wavelength

$\lambda \sim 3310\ nm$, via FEM software is $S_T = -85.3\ pm/K$. This value is in good agreement with a BPM simulation. The BPM simulations also give information about the intensity I of the LP_{01} and LP_{02} modes, allowing the calculation of output intensity I_{out}. Typically, in silica optical fibers, the observed redshift is due to a decrease of Δn_{eff} with an increase in temperature (positive thermo-optic coefficient), which dominates over the length increasing effect ΔL, depending on the small thermal expansion α. Conversely, in zirconium fluoride fiber the increase of Δn_{eff} and L gives a blueshift by increasing the temperature.

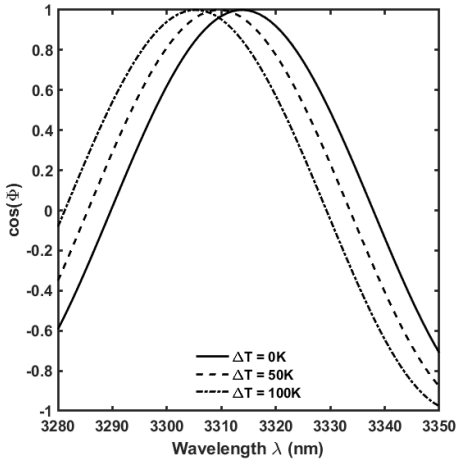

Figure. 4.4 Cosine of the phase delay of the modes ϕ as a function of the wavelength λ for different temperature changes $\Delta T = 0\ K$ (solid curve), $\Delta T = 50\ K$ (dashed curve),and $\Delta T = 100\ K$ (dot-dashed curve), simulated via FEM software [7].

4.2 Fabrication

The next step involved the fabrication of the optical fiber sensor using a ZBLAN optical fiber produced by Le Verre Fluoré [146]. The polyacrylate coating is removed from the fiber segment intended for tapering using a chemical stripping gel. The optical fiber is then cleaned with isopropyl alcohol and cleaved with Vytran LDC-400, with 95g tension. Then, the optical fiber is mounted on the fiber holding blocks of the Vytran GPX-2400. Pretension F_T is applied before starting the process, by moving one fiber holding block. A commercial graphite filament is chosen by considering the cladding diameter d_{cl} of the optical fiber. It is used for heating the fiber close to the glass softening point $T_g = 265\ °C$. This value of temperature is accurately maintained during the entire fabrication process, otherwise an increase in heating temperature may lead to crystallizations and induce losses. Conversely, an inadequate heating of glass could lead to either fiber breakage or the formation of a thicker waist.

Table 4.1 reports the fabrication parameters employed for the fabrication process using the Vytran GPX-2400, including the initial filament power P_f, the pulling speed v_b, and pretension F_T. The initial filament power P_f required fine tuning, as it is slightly dependent on ambient temperature especially when working with soft glasses [154].

TABLE 4.1 PARAMETERS EMPLOYED FOR FABRICATION

Parameters	**Value**	**Description**
$P_f\ (W)$	10	Initial filament power
$v_B\ (mm/s)$	0.5	Pulling speed
$F_T\ (g)$	18	Pretension

To prevent reactions with ambient air due to the hygroscopic nature of fluoride glass [50], the heating process employed the non-reactive Argon gas with a flow rate $F_{Ar} = 0.35\ L/min$. The preheating, applied prior to the movement of the fiber holding block, has been optimized to avoid optical fiber bending due to gravity. The room temperature and the room humidity are $T = 25\ °C$, and $RH \simeq 30\%$, respectively. The tapering process takes about *30 s.*

Fig. 4.5 shows the micrographs of the fabricated non-adiabatic taper, with a length of 800 μm each, captured with the Vytran GPX-2400 CCD camera, revealing a smooth transition. A good agreement between the designed sensor geometry and the measured one is apparent. The output power P_{out} is measured during the fabrication process to investigate the quality of the device. The optical fiber is excited via a laser source Thorlabs HLS635, emitting at wavelength $\lambda = 635\ nm$ (i.e. red light).

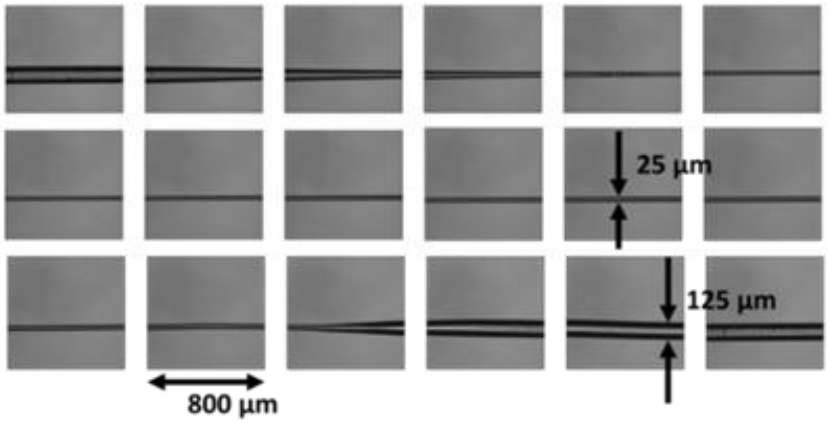

Figure. 4.5 Micrographs of the longitudinal section of the non-adiabatic tapered optical fiber, captured with the Vytran GPX-2400 CCD camera [7].

Fig. 4.6 reports the output power P_{out} (left axis) and tension F (right axis) as a function of drawing time t, measured during the fabrication process. The down-taper region and non-adiabatic taper are completed at $t \approx 17\,s$, and at $t \approx 37\,s$, respectively. Most losses are attributed to the down-taper: power meter data and visual inspection of red-light scattering confirm that this region is the primary source of loss. The measured insertion loss $IL \approx 0.8\,dB$ at the wavelength $\lambda = 635\,nm$ indicating good taper quality.

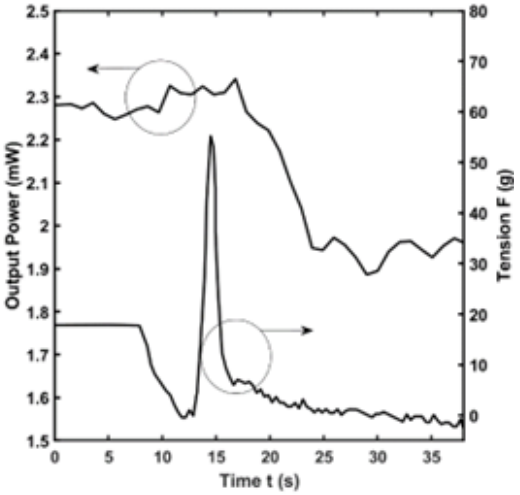

Figure. 4.6 Output power P_{out} (left axis) and tension F (right axis) as a function of drawing time t, measured during the fabrication process [7].

4.3 Characterization

The excitation source is an Interband Cascade Laser (ICL) emitting at the wavelength $\lambda = 3.34\ \mu m$, coupled to the fabricated non-adiabatic optical fiber sensor using a Bare Fiber Terminator (BFT). Fig. 4.7 shows the measured farfield beam profile, captured with Pyrocam IIIHR at the wavelength $\lambda = 3.34\ \mu m$; *a)* before the down-taper, and *b)* in the waist region. As confirmed by 3D-BPM simulation, also in the waist region the LP_{01} mode is the one with the highest intensity, see Fig. 4.7 (b).

Fig. 4.8 illustrates the experimental setup used to evaluate the sensing performance as a function of temperature T. The fabricated sensor is placed in an electric furnace and the output power at the wavelength $\lambda = 3.34\ \mu m$ is recorded by a Power Meter (PM), at fixed values of temperature $T = 20\ °C$, $T = 40\ °C$, $T = 60\ °C$, and $T = 80\ °C$. A three-minute waiting time is observed to stabilize the temperature T, before acquiring each measurement.

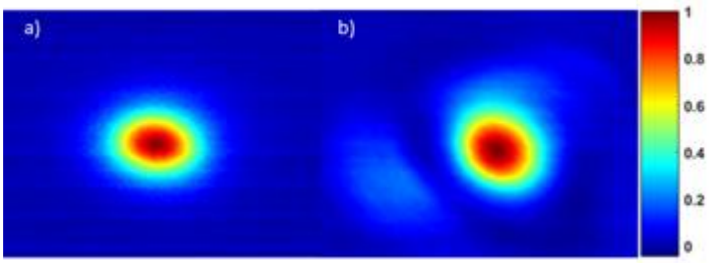

Figure. 4.7 Measured farfield beam profile, captured with Pyrocam IIIHR at the wavelength $\lambda = 3.34\ \mu m$, *a)* before the down-taper, *b)* in the waist region [7].

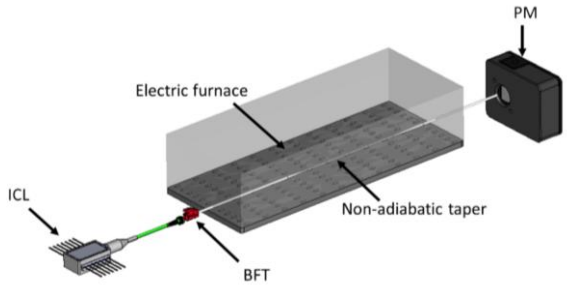

Figure. 4.8 Experimental setup used to evaluate the sensing performance as a function of temperature T, composed of the ICL, non-adiabatic fiber sensor, PM and electric furnace. [7].

Fig. 4.9 compares the experimental results (circle markers) and the BPM simulations (cross markers), demonstrating a good agreement between both results. The output powers of the BPM simulation have been normalized considering a reference power $P_{out} = 1.1\ mW$, at $T = 20\ °C$. The best fit line of the measured points (dash-dotted line) is also reported.

Fig. 4.10 shows a second experimental setup used to demonstrate interferometry between the LP_{01} and LP_{02} modes. The setup consists of a broadband halogen lamp, a monochromator Horiba iHR550 to sample the wavelength λ, an InSb detector cooled with liquid nitrogen, and a lock-in amplifier. The measurements cover the wavelength range $\lambda = 3.00 \div 4.00\ \mu m$ with a resolution step of $\Delta\lambda = 10\ nm$. Firstly, the power guided by the ZFG 6.5/125 optical fiber is measured. Then, the ZFG 6.5/125 optical fiber is aligned with the non-adiabatic tapered optical fiber based on zirconium fluoride glass and the power at the output port is measured.

Fig. 4.11 shows the measured comb-like spectrum at the output of the non-adiabatic tapered optical fiber.

The temperature sensitivity depends on the operating wavelength. In principle, the simulated sensitivity could be experimentally verified by performing measurements around $\lambda \approx 3310\ nm$ using a broadband source in combination with

an optical spectrum analyzer. However, at the time of the experiments, broadband measurements were carried out using a monochromator with a spectral resolution of $5\ nm$, which is insufficient to accurately resolve the sensor sensitivity. The measurement reported in Fig. 4.9 should therefore be considered qualitative; nevertheless, it can be employed to justify the blue shift of the spectral peak. In conclusion, a broadband spectral interrogation approach is preferable to intensity-based measurements at a fixed wavelength. It is worth noting that the dynamic response (response time) of the sensor has not been characterized.

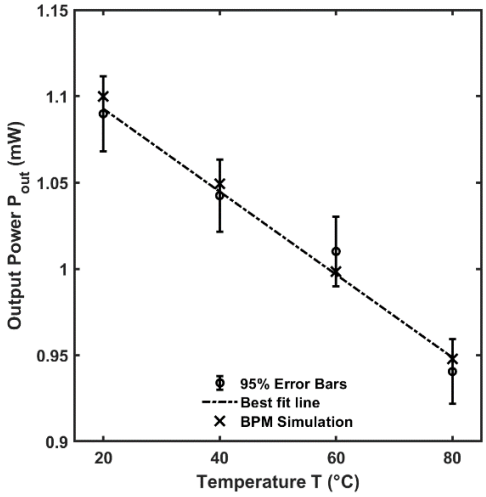

Figure. 4.9 Output power P_{out} at the wavelength $\lambda = 3.34\ \mu m$, for different temperatures T; measurements (circle markers), best fit line of the measured points (dash-dotted line), and BPM simulation (cross markers) [7].

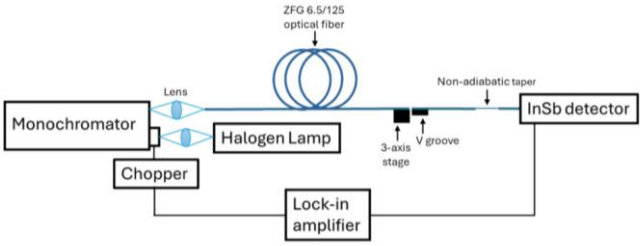

Figure. 4.10 Experimental setup used to evaluate the comb-like spectrum at the output of the optical fiber sensor, composed of a broadband halogen lamp, a monochromator, an InSb detector, and a lock-in amplifier [101].

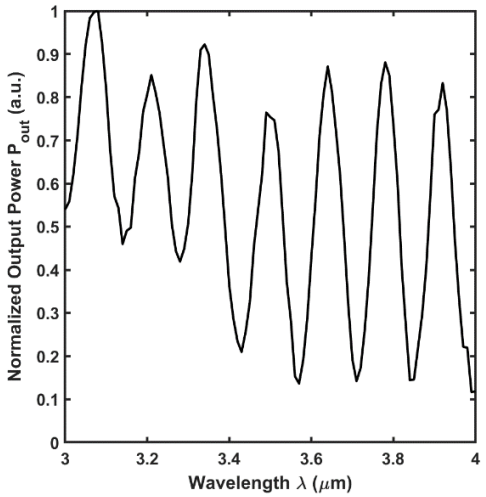

Figure. 4.11 Measured normalized output power P_{out} as a function of the wavelength λ for the optical fiber sensor [101].

4.4 Comparison with State of the Art

A comparison between the proposed device and other temperature optical fiber sensors reported in the literature is summarized in Table 4.2. For multiparameter devices, only the temperature sensitivity values are listed. The proposed non-adiabatic optical fiber taper sensor exhibits temperature sensitivity S_T performance higher than several silica sensors, even when based on more complex structures. The proposed sensor exhibits a negative temperature sensitivity S_T (blueshift) unlike the positive sensitivity (redshift) typically observed. This feature can be fundamental for multiparameter sensing: the condition number can be lowered, leading to a better-conditioned problem [155]. In addition, the proposed sensor is low-cost compared to most of the devices reported in Table 4.2, which are often based on more sophisticated geometries. Although fluoride glass cannot be employed for high-temperature sensing like silica, it represents a promising candidate for cryogenic temperature measurements. Specifically, silica glass exhibits a low coefficient of thermal expansion α even at room temperature, and its thermo-optic coefficient dn/dT drops at cryogenic temperatures, rendering the temperature sensitivity unsuitable for such applications. Conversely, fluoride glass could offer a valid alternative to improve temperature sensitivity in the cryogenic regime without the need to attach external materials with high thermal expansion coefficients α to the fiber, a common technique employed to enhance the sensitivity of sensors based on silica glass.

TABLE 4.2 PERFORMANCE COMPARISON WITH STATE OF THE ART

Ref.	**Sensitivity S_T**	**Description**
[46]	77.0 pm/°C	Double taper Mach-Zender interferometer
[48]	48.8 pm/°C	Core offset multimode fiber spliced with two single mode fibers
[148]	16.5 pm/°C	Inner air cavity Fabry-Perot interferometer with double direction offset
[152]	14.7 pm/°C	Step-structured fiber inline Michelson interferometer
[153]	63.9 pm/°C	Taper and lateral shifted junction
[156]	13.92 pm/°C	Core-offset single mode, multimode, single mode fiber
[157]	59.1 pm/°C	Long-period grating and misaligned fusion splicing point
[158]	81.7 pm/°C	Two-point CO_2 laser irradiations
[159]	41.9 pm/°C	Hollow-core fiber segment spliced between two single-mode fibers
[160]	67.4 pm/°C	Two cascaded Fabry-Perot interferometers
[161]	706.9 pm/°C	Vernier effect based on Fabry-Perot interferometer cascaded with FBG on hollow-core fiber
[162]	−790 pm/°C	Polymer-overlaid two-mode microfiber knot resonator
This work	−85.3 pm/°C	Non-adiabatic taper on zirconium fluoride optical fiber

4.5 Conclusion

A single-mode non-adiabatic tapered optical fiber has been designed and fabricated based on zirconium fluoride glass, offering a low-cost solution for Mid-IR sensing. Specifically, the proposed sensor exhibits higher sensitivity than equivalent silica devices due to specific thermo-optic and thermal expansion coefficients of fluoride glass, and the capability to operate at longer wavelengths. The sensitivity principle is investigated via FEM and BPM simulations, and a comprehensive explanation is proposed. A blueshift of the dips is simulated for increasing temperature value. The simulated sensitivity $is\ S_T = -85.3\ pm/K$. The characterization is performed in the Mid-IR range, by observing the output power variation versus temperature. The experimental results show good agreement with the simulations. Finally, broadband characterization confirmed the expected comb-like spectral pattern at the output of the tapered fiber.

5 Design and Fabrication of Antipodal Vivaldi Antenna with MTMs

In this chapter, a wideband AVA is designed, fabricated using a standard and low-cost Printed Circuit Board (PCB) fabrication process, and characterized. The design is carried out via CST Studio Suite® Software, while measurements are performed using the N5224A PNA Microwave Network Analyzer and the Satimo StarLab Antenna Pattern Measurement System. To maximize the gain G, the AVA is enhanced by employing multiple metalenses, based on a modified version of circular Split Ring Resonators (SRRs). Three configurations of metalenses have been designed, fabricated and characterized; the third one achieved a measured peak gain of $G_{max} = 12\ dB$ at operating frequency $f = 8.6\ GHz$, and operative bandwidth $f = 3 - 13\ GHz$. A good agreement is obtained between the simulated and the measured results. The AVA is designed to operate in the *X*-Band range to facilitate fabrication and characterization, employing the instrumentation available in the MOE Laboratory of Politecnico di Bari.

5.1 Antipodal Vivaldi Antenna Design

The AVA is designed using a commercial substrate Rogers RO4350B, with a dielectric permittivity $\varepsilon_r = 3.66$ and a loss tangent $tan\delta = 0.0037$. The commercial substrate thickness is $t_{sub} = 0.762\ mm$ and the standard copper cladding has a thickness $t_c = 0.035\ mm$. The layout of the designed AVA is shown in Fig. 2.4. The AVA has three-flares and an operating bandwidth $f = 3 - 13\ GHz$. To minimize the antenna size, two tapered slots have been optimized [112]. The multiparametric optimization has been carried out using CST Studio Suite® Software. The simulations are performed via parametric sweeps of the key degrees of freedom, namely: *i)* the flare widths w_1, w_2, and w_3, and *ii)* the distances between the flares d_1 and d_2. During the optimization, the profile of each flare was geometrically constrained by equations (2.35) - (2.36), and the parameters were bounded to maximize the realized gain while preserving a $-10\ dB$ impedance matching. Table 5.1 lists the optimized geometric parameters that maximize the gain over the whole operating bandwidth.

Fig. 5.1 shows the reflection magnitude $|S_{11}|$ (right axis) and the gain G (left axis) as a function of the frequency f, considering the geometrical parameters reported in the Table 5.1.

TABLE 5.1 GEOMETRIC PARAMETERS OF THE AVA

Parameters	**Value**	**Description**
$L_{viv}(mm)$	73.7	Antenna length
$W_{viv}(mm)$	48	Antenna width
$P_{x1}(mm)$	15	*x*-position of the inner point of the first tapered slot
$P_{y1}(mm)$	22	*y*-position of the inner point of the first tapered slot
$P_{x2}(mm)$	19	*x*-position of the inner point of the second tapered slot
$P_{y2}(mm)$	58.4	*y*-position of the inner point of the second tapered slot
$w_1(mm)$	5	First flare width
$w_2(mm)$	5	Second flare width
$w_3(mm)$	8.7	Third flare width
$d_1(mm)$	5	Distance between the first and the second flares
$d_2(mm)$	10	Distance between the second and the third flares

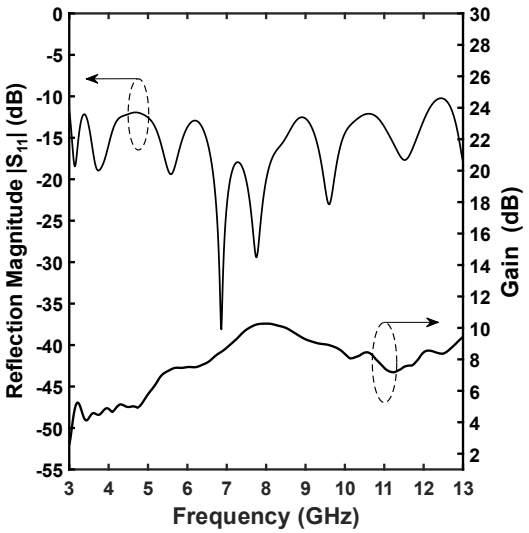

Figure. 5.1 Reflection magnitude $|S_{11}|$ (right axis) and realized gain G (left axis) as a function of the frequency f of the AVA [113].

5.2 Unit Cell Design and Simulation

Fig. 5.2 shows the geometry of the unit cell with the geometrical parameters considered for the modelling and the simulations. It consists of a modified version of an SRR. The unit cell geometry has been optimized by numerical simulations in planar array configurations integrated on the AVA substrate. During the optimization phase, geometries characterized by the presence or absence of a central dot have been considered by varying: *i)* the ring radius r_c; *ii)* the angular

aperture of the split α; *iii)* the strip width w; and *iv)* the unit cell lattice lengths d_x, d_y, and d_z. Table 5.2 lists the geometrical parameters of the UC.

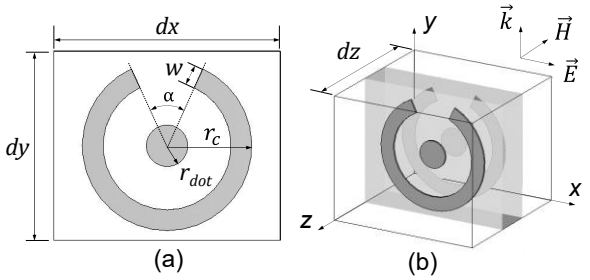

Figure. 5.2 Schematic of the modified SRR unit cell with geometrical parameters: a) Top and bottom views, and b) 3D view [113].

TABLE 5.2 GEOMETRIC PARAMETERS OF THE UNIT CELL

Parameters	**Value**	**Description**
$d_x(mm)$	3	Unit cell lattice length along *x*-axis
$d_y(mm)$	2.5	Unit cell lattice length along *y*-axis
$d_z(mm)$	3	Unit cell lattice length along *z*-axis
$r_c(mm)$	1.125	Ring radius
$r_{dot}(mm)$	0.275	Dot radius
$\alpha\ (deg)$	50	Angular aperture of the split
$w(mm)$	0.275	Strip width

Fig. 5.3 shows the equivalent resonant circuit of the modified SRR unit cell. When a unit cell is traversed by an electromagnetic wave, inductive and capacitive effects are induced in the unit cell, resulting in currents and local charges. These phenomena depend on the electric field orientation of the traveling wave with respect to the unit cell orientation. The equivalent capacitor, namely C_{split}, represents the capacitive effects occurring at the non-parallel capacitive gap. A metal dot, placed in the center of the circular ring, induces a coupling capacitive effect C_{coup} with the ring, which increases the global effective capacitance of the metalens. The equivalent inductor, namely L_{ring}, represents the self-inductance effects occurring along the circular ring. The metal inclusions are placed on both sides of the substrate, resulting in strong mutual coupling effects between the top and bottom layers of the unit cell.

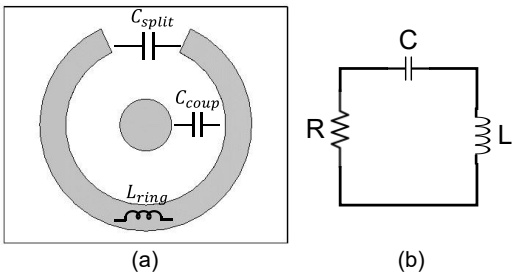

Figure. 5.3 a) Schematic of the modified SRR unit cell with main inductive and capacitive effects: b) equivalent circuit [113].

The transmission properties of the designed unit cell are investigated using two distinct numerical approaches. In the first step, a single unit cell is analysed under specific boundary conditions, as shown in Fig. 5.4. Port 1 acts as the excitation port, with open boundary conditions applied along the propagation direction, and Perfect Electric Conductor (PEC) and Perfect Magnetic Conductor (PMC) boundary conditions applied to the lateral walls.

Fig. 5.5 shows the simulated reflection $|S_{11}|$ and transmission $|S_{21}|$ magnitude, and the retrieved effective parameters of the unit cell, based on the geometric values listed in Table 5.2.

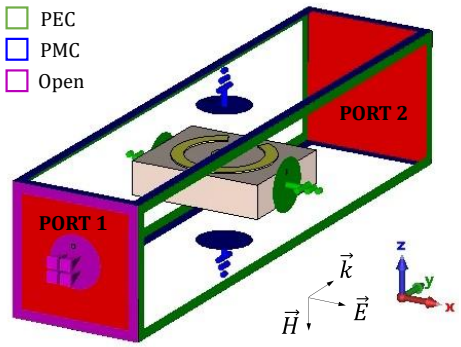

Figure. 5.4 Simulation setup and boundary conditions of the unit cell [113].

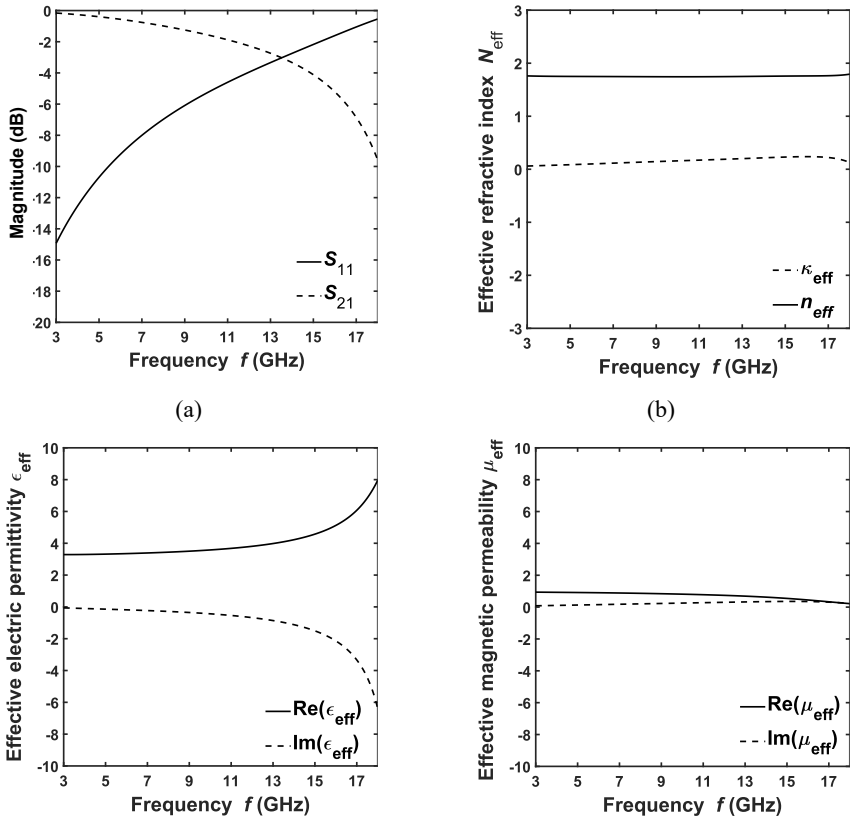

Figure. 5.5 Simulated reflection $|S_{11}|$ and transmission $|S_{21}|$ magnitude and retrieved effective parameters of the unit cell as a function of the frequency f: (a) Simulated *S*-parameters; (b) complex refractive index (N_{eff}); (c) effective electric permittivity (ε_{eff}); and (d) effective magnetic permeability (μ_{eff}) [113].

In particular, Fig. 5.5 (a) shows the simulated reflection $|S_{11}|$ and transmission $|S_{21}|$ magnitude obtained by CST Studio Suite Software; while Fig. 5.5 (b), 5.5 (c), and 5.5 (d) show the retrieved effective parameters for complex refractive index (N_{eff}), effective electric permittivity (ε_{eff}), and effective magnetic permeability (μ_{eff}), respectively. The unit cell effective parameters have been calculated using the S-Parameter Retrieval Method [88, 114, 115]. Fig. 5.5 (a) shows that the modulus of the reflection magnitude $|S_{11}|$ is smaller than $-4\ dB$ for frequencies below $f < 13\ GHz$. Fig. 5.5 (b) shows that the complex effective refractive index $N_{eff} = n_{eff} + jk_{eff}$ is a constant non-resonant value over the whole bandwidth. These results, even if approximated, give valuable information regarding a non-resonant and promising good behavior for all the considered metalenses over the bandwidth of interest [163,164].

5.3 Antipodal Vivaldi Antenna Simulation with Unit Cells

Different unit cell configurations with AVA have been considered and simulated. Fig. 5.6 shows three of the most interesting and optimized antenna configurations. Fig. 5.6 (a) shows the layout of the first configuration, denoted as AVA SRR#1. The unit cells, placed between the flares of the antenna in the end-fire direction, consist of a triangular array of fifteen SRR elements. Fig. 5.6 (b) shows

the second layout configuration, denoted as AVA SRR#2, derived from AVA SRR#1 by introducing a rectangular unit cell array at a distance h_1 from the triangular one, separated by an air gap. The rectangular metalens consists of sixty elements arranged in a $N \times M = 4 \times 15$ array. Fig. 5.6 (c) shows the third layout configuration, denoted as AVA SRR#3. This design is similar to the AVA SRR#2 configuration, but variable unit cell sizes have been exploited to achieve a good behaviour for different frequencies. The optimization of the AVA integrated with the three proposed SRR metalenses has been performed in the frequency range $f = 3 - 13\ GHz$, varying: *i)* the metalens position; *ii)* the number of unit cells for both triangular and rectangular arrays; *iii)* the distance between triangular and rectangular metalenses h_1; *iv)* the scaling factor k of the unit cells in the case of alternate rows, i.e. for AVA SRR#3.

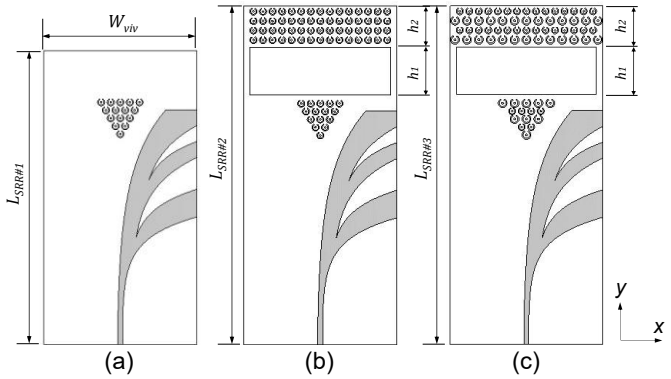

Figure. 5.6 Layout of the designed AVA with metalenses: (a) AVA SRR#1, (b) AVA SRR#2, and (c) AVA SRR#3 [113].

Table 5.3 reports the optimized geometric parameters of the AVA SRR antennas. An optimized scaling factor of $k = 1.125$ has been identified, after several simulations, to scale up the unit cells of the alternate rows for both triangular and rectangular metalenses of AVA SRR#3.

Fig. 5.7 shows the simulated input reflection coefficient $|S_{11}|$ as a function of the frequency f. The optimized AVA SRR#1 (dashed line) maintains the wideband pristine behavior of AVA. For the optimized AVA SRR#2 (dash-dotted line) and AVA SRR#3 (dotted line), the introduction of the rectangular metalens in addition to the triangular one slightly reduces the -10 dB bandwidth at high frequencies.

TABLE 5.3 GEOMETRIC PARAMETERS OF THE AVA SRR

Parameters	**Value**	**Description**
$L_{SRR\#1}(mm)$	92.15	AVA SRR#1 length
$L_{SRR\#2}(mm)$	106.7	AVA SRR#2 length
$L_{SRR\#3}(mm)$	106.7	AVA SRR#3 length
$h_1(mm)$	15	Distance between triangular and rectangular metalens
$h_2(mm)$	13	Rectangular metalens length

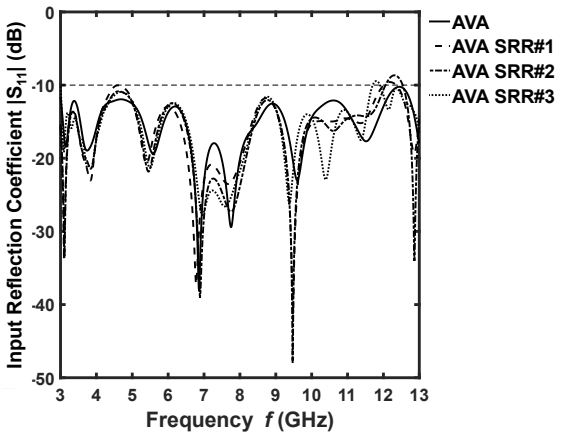

Figure. 5.7 Simulated input reflection coefficient $|S_{11}|$ as a function of the frequency f, for AVA without metalens (solid line), AVA SRR#1 (dashed line), AVA SRR#2 (dash-dotted line), and AVA SRR#3 (dotted line) [113].

Fig. 5.8 reports the simulated gain G (black lines) and gain increase ΔG (red lines) as a function of frequency f. Specifically, simulations of AVA SRR#1 indicate a peak gain of $G_{max} = 10.8\, dB$ and a maximum gain increase of $\Delta G_{max} = 1.7\, dB$ at the frequency $f = 12.9\, GHz$, compared to AVA without the metalenses. Improved gain performance is observed for AVA SRR#2 across the entire operative bandwidth, with a peak gain $G_{max} = 11.2\, dB$ at the frequency $f = 8.1\, GHz$ and a maximum gain increase $\Delta G_{max} = 2\, dB$ at the frequency $f = 11.8\, GHz$. AVA SRR#3 exhibits the highest gain only for $f < 10.3\, GHz$, achieving a peak gain $G_{max} = 11.4\, dB$ at $f = 8.2\, GHz$ and a maximum gain increase of $\Delta G_{max} = 2.1\, dB$ at the frequency $f = 10.1\, GHz$.

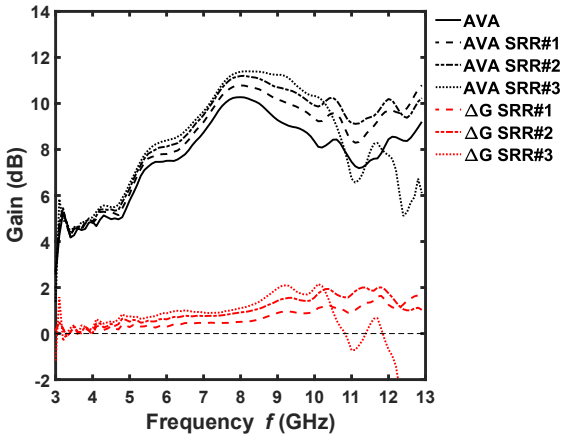

Figure. 5.8 Simulated gain G (black lines) and gain increase ΔG (red lines) as a function of frequency f, for AVA without metalens (solid line), AVA SRR#1 (dashed line), AVA SRR#2 (dash-dotted line), and AVA SRR#3 (dotted line) [113].

5.4 Antipodal Vivaldi Antenna Fabrication and Characterization

Fig. 5.9 shows the four AVA prototypes realized on a Rogers RO4350B dielectric substrate via a standard and low-cost PCB fabrication process. The geometrical parameters used for the fabrication are listed in Tables 5.1–5.3. Experimental characterization is performed using the N5224A PNA Microwave Network Analyzer and the Satimo StarLab Antenna Pattern Measurement System.

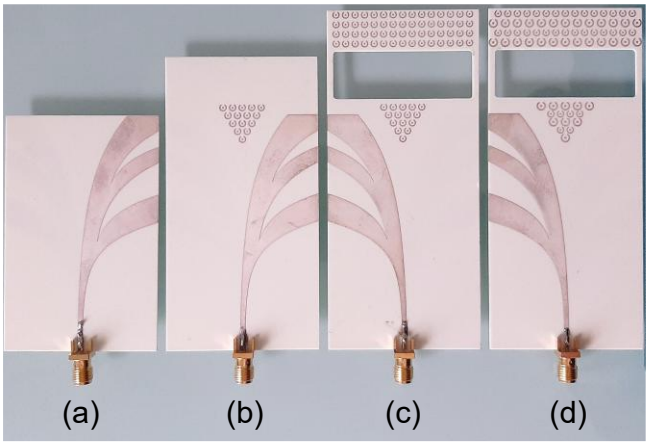

Figure. 5.9 AVA Prototypes: a) AVA without metalens, b) AVA SRR#1, c) AVA SRR#2, and d) AVA SRR#3.

Fig. 5.10 shows the measured input reflection coefficient $|S_{11}|$ as a function of frequency f for the four AVA prototypes. The measurements confirm the simulated result; in fact, across the band $f = 3\ GHz - 13\ GHz$, the scattering parameter $|S_{11}|$ remains below $-10dB$.

Fig. 5.11 shows the comparison between simulated (solid lines) and measured (dotted lines) gain G as a function of frequency f for the four AVA antennas. The experimental results agree with the simulations, confirming that the designed metalenses allow a gain improvement over the entire band in the case of AVA SRR#1 and AVA SRR#2 and at low frequencies for AVA SRR#3. A peak gain of $G_{max} = 11.5\ dB$ at a frequency of $f = 13\ GHz$ has been measured for the AVA SRR#1 prototype. Furthermore, peak gains of $G_{max} = 11.4\ dB$, and

$G_{max} = 12\ dB$ have been measured at the frequency $f = 8.6\ GHz$ for AVA SRR#2 and AVA SRR#3, respectively.

Fig. 5.12 shows the gain increase ΔG of the three AVAs with metalens compared to the AVA without metalens as a function of the frequency f, comparing the simulated (solid lines) and measured (dotted lines) results. The measured curves are close enough to the simulated ones.

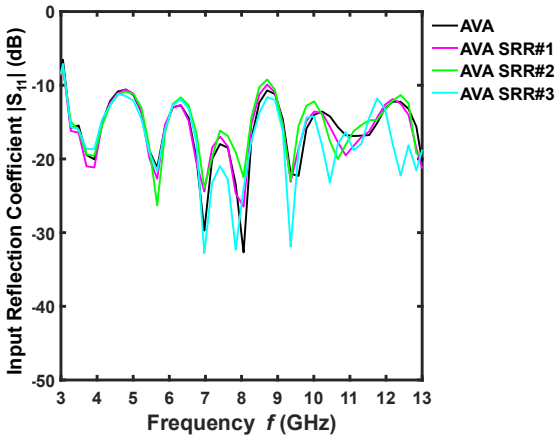

Figure. 5.10 Measured input reflection coefficient $|S_{11}|$ as a function of the frequency f, for AVA without metalens (black line), AVA SRR#1 (magenta line), AVA SRR#2 (green line), and AVA SRR#3 (cyan line) [113].

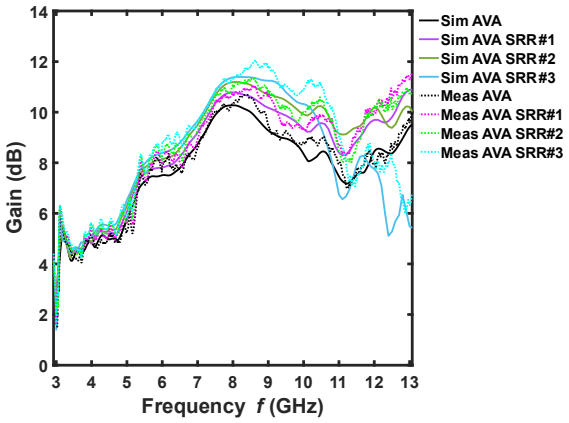

Figure. 5.11 Simulated (solid lines) and measured (dotted lines) gain G as a function of frequency f, for AVA without metalens (black line), AVA SRR#1 (magenta line), AVA SRR#2 (green line), and AVA SRR#3 (cyan line) [113].

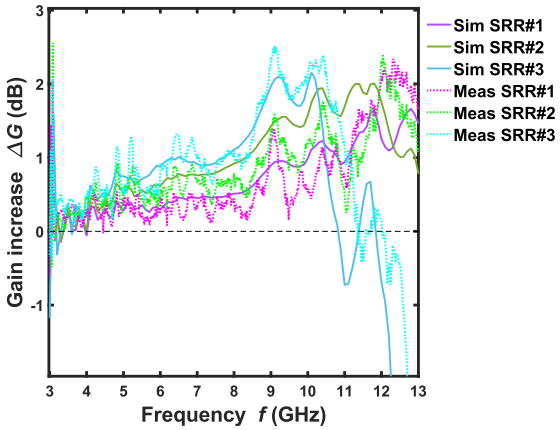

Figure. 5.12 Simulated (solid lines) and measured (dotted lines) gain increase ΔG as a function of frequency f, for AVA without metalens (black line), AVA SRR#1 (magenta line), AVA SRR#2 (green line), and AVA SRR#3 (cyan line) [113].

Table 5.4 lists the simulated and measured peak gain G_{max} and the respective frequencies f. Table 5.5 reports the simulated and measured gain increase ΔG of the AVA with metalens compared to AVA without metalens at the respective frequencies f.

Fig. 5.13 plots the measured *E*- (left column) and *H*-plane (right column) radiation patterns of the AVA with metalens compared to that of the AVA without metalens as a function of the elevation angle θ. These measurements are performed at the frequencies where the maximum gain increase ΔG occurs. The measured Half-Power Beamwidth (HPBW) of the AVA is reduced over the entire band when the metalenses are integrated on the antenna. For AVA SRR#1, the measured $-3\,dB$ beamwidth in *H*-plane decreases from $HPBW_{AVA} = 46.36°$ to $HPBW_{SRR\#1} = 40.70°$ at frequency $f = 12.3\,GHz$; for AVA SRR#2 from $HPBW_{AVA} = 51.27°$ to $HPBW_{SRR\#2} = 33.6°$ at frequency $f = 12\,GHz$, and finally for AVA SRR#3 from $HPBW_{AVA} = 62.91°$ to $HPBW_{SRR\#3} = 43.29°$ at frequency $f = 9\,GHz$.

TABLE 5.4 SIMULATED AND MEASURED PEAK GAIN

	Simulated		**Measured**	
	$Freq.$ (GHz)	G_{max} (dB)	$Freq.$ (GHz)	G_{max} (dB)
SRR#1	12.9	10.8	13	11.5
SRR#2	8.1	11.2	8.6	11.4
SRR#3	8.2	11.4	8.6	12

TABLE 5.5 SIMULATED AND MEASURED GAIN INCREASE ΔG

	Simulated		**Measured**	
	$Freq.$ (GHz)	G_{max} (dB)	$Freq.$ (GHz)	G_{max} (dB)
SRR#1	12.9	1.7	12.3	2.3
SRR#2	11.8	2	12	2.4
SRR#3	1.1	2.1	9	2.5

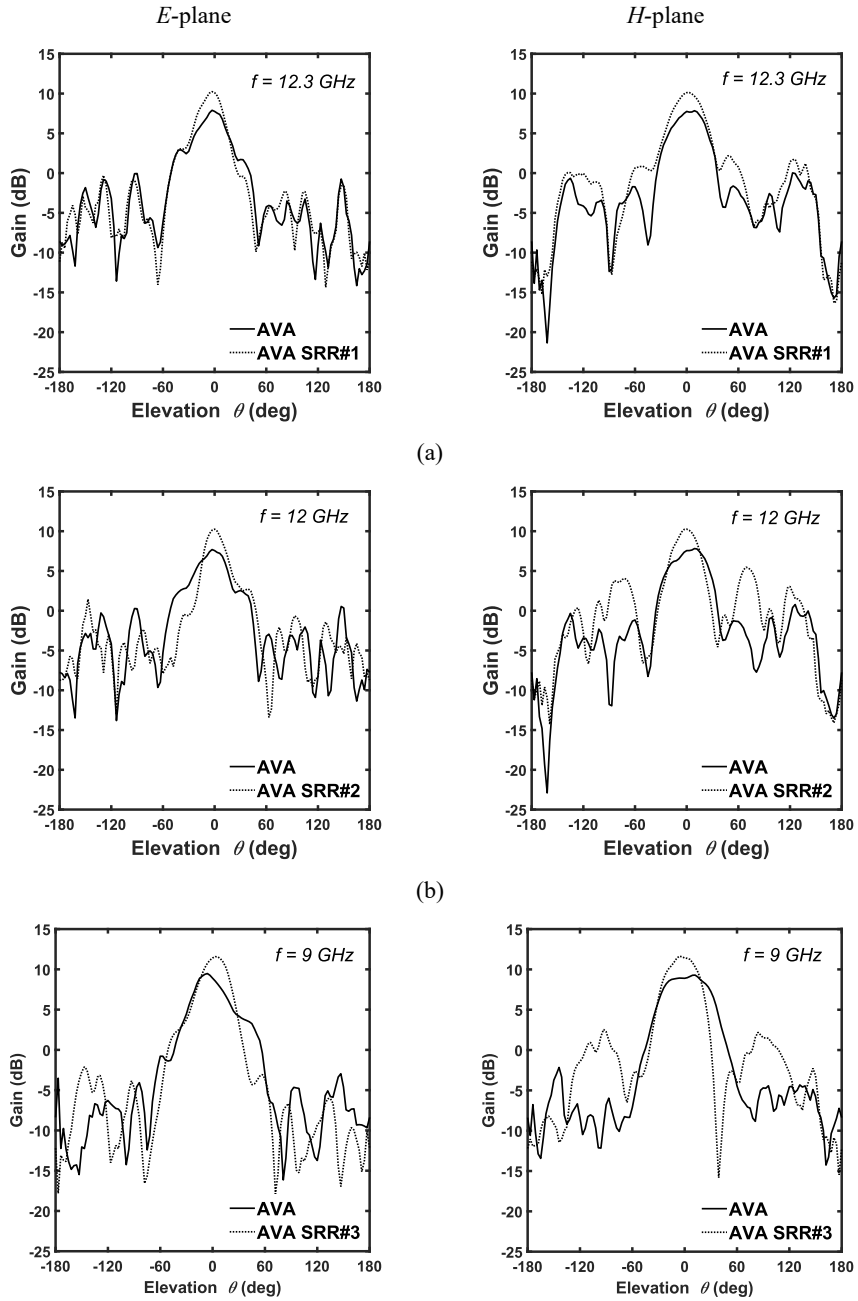

Figure. 5.13 Measured *E*-plane (left column) and *H*-plane (right column) radiation patterns as a function of the elevation angle θ for AVA without metalens (solid line), compared to AVAs with metalens (dotted lines): a) AVA SRR#1, b) AVA SRR#2, and c) AVA SRR#3 [113].

5.5 Conclusion

In this chapter, microstrip antipodal Vivaldi antennas integrated with metalenses have been designed, fabricated, and characterized in the frequency band $f = 3 - 13\ GHz$. Good agreement between simulated and measured performance has been observed, confirming the gain enhancement over a wide frequency range, while preserving the operating bandwidth. The measurements revealed a peak gain of about $G_{max} = 12\ dB$ at the operating frequency $f = 8.6\ GHz$, and a maximum gain increase of about $\Delta G = 2.5\ dB$ at the operating frequency $f = 9\ GHz$ for AVA SRR#3.

6 Design and Fabrication of Fabry-Perot Antenna

In this chapter an unconventional fabrication technique for FPA is proposed. The prototype is fabricated via a hybrid manufacturing process that integrates inkjet printing and 3D printing. The measured results are in good agreement with the design. The antenna exhibits a maximum measured gain of $G_{max} = 13.2\ dB$ at frequency $f = 8.2\ GHz$, a measured impedance bandwidth of $BW = 31.3\ \%$, and a -3 dB gain bandwidth of $BW_G = 24.5\%$ inside the impedance bandwidth. The obtained results allow for low-cost fabrication of conformal antennas exhibiting good performance, even when compared to expensive and sophisticated manufacturing technologies. The FPA is designed to operate in the *X*-Band range to facilitate fabrication and characterization, employing the instrumentation available in the MOE Laboratory of Politecnico di Bari.

6.1 Design of the Partially Reflective Surface

The UC design of PRS aims to achieve the required phase response ϕ_{PRS}, and an appropriate magnitude of the reflection coefficient ρ. These conditions are crucial to obtain a good improvement of the directivity. A positive phase gradient can be achieved in a frequency band around the PRS resonance frequency, where the steepness of the gradient is directly proportional to the strength of the resonance [120]. However, strong resonances are not desirable; the reflection coefficient magnitude ρ decreases, thereby reducing the directivity D_{PRS}, as indicated by eq. (2.44).

Fig. 6.1 shows the geometry of the proposed FPA, detailing the architecture, the UC composition, and the feeding element. In particular, Fig. 6.1 (a) shows the schematic of the FPA architecture, comprising a V-slot loaded patch and a double-layer PRS. The double-layer PRS is formed by two PRS surfaces PRSs, denoted as PRS1 and PRS2. Fig. 6.1 (b) details the UC structure of one of the two layers of the double-layer PRS. Each layer features a sandwich structure wherein a thicker PETG substrate is interposed between two ultra-thin PET substrates with a mesoporous coating, i.e., Novele™ IJ-220. The conductive ink is deposited on Novele™ IJ-220 substrates with a printed periodic array of square apertures (inductive element) on one side, and a periodic array of square patches (capacitive element) on the other side, constituting a complementary FSS [120, 165, 166]. In this way, both PRS1 and PRS2 contribute to the antenna operation

by inducing a resonance. The inclusion of the 3D-printed PETG inside the two single-sided Novele™ IJ-220 substrates allows for fine-tuning and optimization of the PRS reflection phase ϕ. Fig. 6.1 (c) shows the top layer of the V-slot feed antenna with the main geometrical parameters considered in the design.
It consists of a patch radiator featuring a V-shaped slot aperture. Fig. 6.2 shows the equivalent circuit of the double-layer PRS [118].

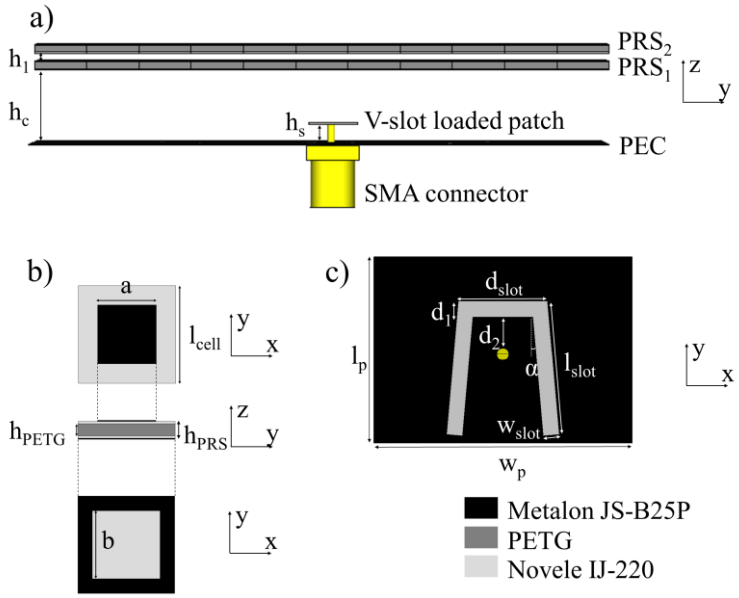

Figure 6.1 a) Schematic of the FPA, comprising a feed antenna and a double-layer PRS. b) Schematic of the square patches (top) and square apertures (bottom) of a single layer of the double-layer PRS. c) Sketch of the V-slot feed antenna [167].

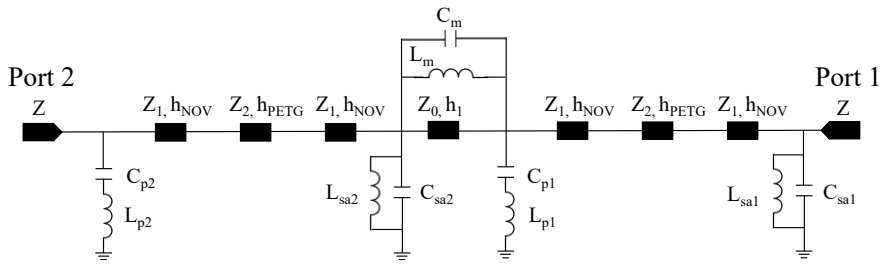

Figure. 6.2 Equivalent circuit of the double-layer PRS [167].

The optimization of the double-layer PRS UC has been performed using the frequency-domain solver of CST Microwave Studio Suite, applying periodic boundary conditions to the four walls of the UC. The antenna is designed to operate in the considered frequency range from about 7 GHz to about 9.5 GHz. The target of the unit cell optimization in CST Microwave Studio was to achieve a positive reflection phase gradient over the entire operating frequency range ($7 - 9.5\ GHz$) and to maintain the reflection coefficient magnitude $\rho > 0.5$, ensuring high antenna directivity D_{FPA}, according to equation (2.44).

Consequently, the frequency region exhibiting a positive phase gradient must include the aforesaid range. In order to accurately evaluate the reflection phase, de-embedding for the Floquet ports is taken into account, with the phase referenced at the closest surface of PRS1, corresponding to the square aperture of PRS1. The Novele™ IJ-220 PET-based substrate is characterized by a substrate thickness of $h_{NOV} = 0.14\ mm$, dielectric constant $\epsilon_r = 2.95$, and loss tangent $tan\delta = 0.025$ [167, 168]. Similarly, PETG is modelled with dielectric constant

$\epsilon_r = 2.85$, and loss tangent $tan\delta = 0.025$ [167, 169], and since this material is 3D-printed, its thickness can be freely optimized. The conductive ink is Metalon JS-B25P with a silver content of 25 $wt\%$.

Table 6.1 lists the parameters considered in the design of the UC.

TABLE 6.1 GEOMETRICAL PARAMETERS OF THE PRS UNIT CELLS

Parameters	**Value**	**Description**
$a_1\ (mm)$	8.6	lengths of the square apertures
$a_2\ (mm)$	7.7	lengths of the square apertures
$b_1(mm)$	8.8	lengths of square patches
$b_2(mm)$	9.2	lengths of square patches
$h_{PETG}(mm)$	1.2	PETG thickness
$h_{PRS}(mm)$	1.48	PRS thickness (PETG+PET)
$h_1(mm)$	2.52	distance between PRS1 and PRS2
$l_{cell}(mm)$	11.2	length of the unit

Fig. 6.3 shows the simulated reflection coefficient magnitude ρ and phase ϕ_{PRS} of the double-layer PRS for incidence angles $\theta = 0°$ (solid line), and $\theta = 20°$ (dashed line) as a function of the frequency f. For comparison, the plot also includes the ideal reflection coefficient magnitude ρ and the ideal reflection phase ϕ_{PRS} (dotted line) calculated by eq. (2.42), considering a cavity height $h_{cav} = 19.70\ mm$ (corresponding to a half wavelength at the frequency $f = 7.6\ GHz$). Additionally, the reflection coefficient magnitude ρ and the reflection phase ϕ_{PRS} obtained through equivalent circuit analysis (dotted line) are reported. The positive phase slope of PRS reflection coefficient and the reflection amplitude coefficient higher than 0.5 ensure that the FPA can resonate with high directivity D_{FPRA} also in case of angled incidence. The figure highlights a slight discrepancy between the simulated phase response and the ideal phase slope. The ideal phase represents the theoretical condition required to maintain a constant resonance across the entire spectral band, as defined by Eq. (2.42). Although the simulated phase exhibits a non-linear slope, it preserves a positive phase gradient over the design range. As a result, the Fabry–Pérot resonance condition is satisfied, still leading to the expected gain enhancement.

Table 6.2 lists the optimized parameters of the equivalent circuit model for the double-layer PRS, which yield a good agreement with the full-wave simulations.

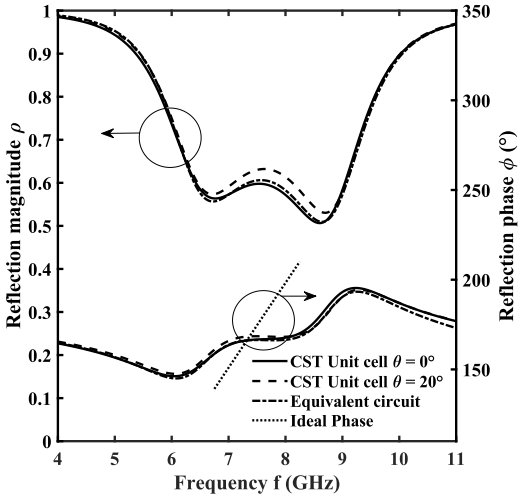

Figure. 6.3 Reflection magnitude ρ and reflection phase ϕ of the double-layer PRS obtained via i) CST Microwave Studio full-wave unit cell simulation for incidence angle $\theta = 0°$ (solid line) and $\theta = 20°$ (dashed line); ii) equivalent circuit model (dash-dotted line); and iii) ideal reflection phase for a FPA with cavity height $h_c = 19.7\ mm$ (dotted line) [167].

TABLE 6.2 OPTIMIZED PARAMETERS OF THE EQUIVALENT CIRCUIT MODEL

Parameters	**Value**	**Description**
$Z\ (\Omega)$	377	Free-space impedance
$Z_1\ (\Omega)$	219.5	Novele substrate impedance
$Z_2\ (\Omega)$	223.3	PETG substrate impedance
$C_{sa1}(pF)$	0.055	PRS1 square aperture capacitance
$C_{p1}\ (pF)$	0.1	PRS1 square patches capacitance
$L_{sa1}\ (nH)$	1.97	PRS1 square aperture inductance
$L_{p1}\ (nH)$	0.31	PRS1 square patches inductance
$C_{sa2}\ (pF)$	0.019	PRS2 square aperture capacitance
$C_{p2}\ (pF)$	0.074	PRS2 square patches capacitance
$L_{sa2}\ (nH)$	2.76	PRS2 square aperture inductance
$L_{p2}\ (nH)$	0.4	PRS2 square patches inductance
$C_m\ (pF)$	0.039	Inter-layer coupling capacitance
$L_m\ (nH)$	4	Inter-layer coupling inductance

6.2 Design of the V-Slot Feed Antenna and the Fabry-Perot Cavity

For a practical implementation, a realistic finite-size antenna configuration has been designed. The primary source is an optimized pin-fed rectangular patch that incorporates a V-slot to improve bandwidth enhancement [170]. This component is fabricated via inkjet printing on two ultra-thin PET substrates serving as the ground plane and the patch, respectively. Table 6.3 lists the geometrical dimensions considered in the design of the V-slot feed antenna.

TABLE 6.3 GEOMETRICAL PARAMETERS OF THE V-SLOT FEED ANTENNA

Parameters	**Value**	**Description**
$d_1\ (mm)$	1.15	V-slot base width (y-axis)
$d_2\ (mm)$	1.65	Feed position offset (y-axis)
$d_{slot}\ (mm)$	6.45	V-slot base length (x-axis)
$\alpha\ (deg)$	5	V-slot angle
$w_{slot}\ (mm)$	1.15	Slot arm width
$l_{slot}\ (mm)$	9.7	Slot arm length
$w_p\ (mm)$	18.7	Patch width
$l_p\ (mm)$	13.5	Patch length

The PRS is composed of a 7×7 element array and considering a UC size of $l_{cell} = 11.2\ mm$, the total dimensions of the array are 78.4 mm×78.4 mm. The same dimensions are chosen for the ground plane. The cavity height is $h = 19.7\ mm$, while the optimized distance between the patch and the ground plane is $h_s = 3.3\ mm$. Fig. 6.4 shows the input reflection coefficient $|S_{11}|$ and the realized gain G as a function of the frequency f for the antenna without PRS (solid line) and with PRS, i.e. the FPA (dashed line). The results demonstrate that the bandwidth of the primary radiator is preserved, and an improvement of the realized gain G, due to the Fabry-Pérot resonance, is obtained.

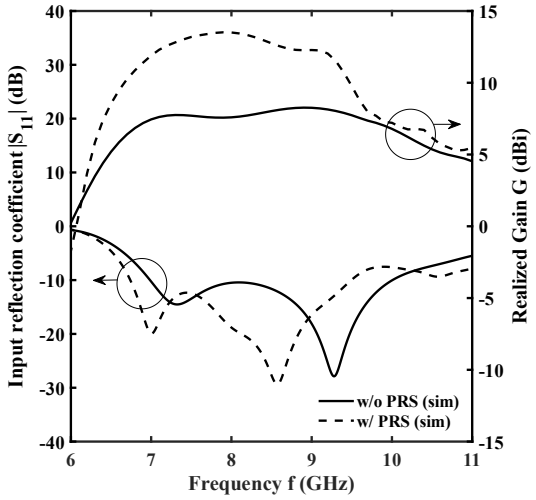

Figure. 6.4 Simulated input reflection coefficient $|S_{11}|$ and realized gain G of the antenna as a function of the frequency f without PRS (solid line) and with the 7×7 PRS array size (dashed line) [167].

6.3 Fabrication of the Fabry-Perot Antenna

Fig. 6.5 shows the fabricated prototype. Specifically, Figs. 6.5 (a) and (b) show the V-slot loaded patch antenna, and a zoom of the antenna taken with Dine-Lite Digital Microscope; Figs. 6.5 (c) and (d) detail the periodic array of square apertures, and square patches of PRS2, respectively; and Fig. 6.5 (e) shows the assembled FPA in the anechoic chamber.

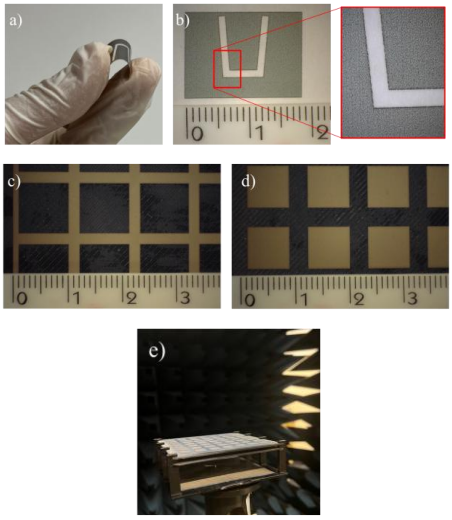

Figure. 6.5 a) Fabricated V-slot loaded patch via conductive inkjet printing, b) Zoom of the fabricated V-slot loaded patch via conductive inkjet printing, c) Periodic array of square apertures, bottom layer of PRS2, d) Periodic array of square patches, top layer of PRS2, e) Assembled FPA with V-slot loaded patch and double-layer PRS in the anechoic chamber [167].

An EPSON Ecotank ET-M1170 printer is employed to deposit the Metalon JS-B25P conductive inkjet on the Novele™ IJ-220 substrate. The SMA connector is glued via MG Chemicals 8331S silver conductive epoxy adhesive and cured for 2 hours at $65°C$. A low-cost Creality K1C 3D printer is employed to fabricate the PETG components, serving as the PRS and spacer. The printing process utilizes a $0.2\ mm$ nozzle and 100% infill density. The fabricated FPA prototype features a total weight of $52\ g$ and an estimated total material cost of $6.50, representing a significant cost reduction compared to conventional manufacturing technologies.

6.4 Characterization of the Fabry-Perot Antenna

The input reflection coefficient $|S_{11}|$ of the antenna without and with the PRS has been measured using the Agilent Technologies N5224A PNA Network Analyzer. The radiation performance measurement of the antenna without and with the PRS has been characterized in the anechoic chamber StarLab SATIMO.

Fig. 6.6 (a) shows the simulated (solid lines) and measured (dashed lines) input reflection coefficient $|S_{11}|$ as a function of the frequency f for the antenna without PRS (black line) and with PRS (red line). The plot demonstrates a good agreement between simulation and measurement, despite a slight shift toward higher frequencies. This frequency shift is likely attributed to a combination of manufacturing and assembly tolerances such as the 3D-printing process, the

manual assembly of the double-layer PRS structure, and the connector gluing. Since the resonance frequency of the Fabry-Perot Cavity is dependent on the cavity height, small variations in the PETG spacer thickness or the alignment of the substrates can result in the measured frequency offset. The measured impedance bandwidth of the FPA covers the frequency range $f = 7.0\,GHz - 9.6\,GHz$.

Fig. 6.6 (b) shows the simulated (solid line) and measured (circle markers) realized gain G and total efficiency η of the antenna as a function of the frequency f without PRS (black) and with PRS (red). The plot reveals a peak gain of $G_{max} = 13.2\,dBi$ at the frequency $f = 8.2\,GHz$, and a measured $-3\,dB$ gain bandwidth of $BW_G = 24.5\%$ within the impedance bandwidth of the FPA. Furthermore, the measured aperture efficiency is approximately 35.3%.

Fig. 6.7 shows the (a) *H*-plane, and the (b) *E*-plane of the simulated and measured radiation patterns for the antenna with PRS, at the frequency $f = 8\,GHz$. The radiation patterns demonstrate that the antenna generates a well-defined broadside beam, maintaining adequate side-lobe levels and cross-polar discrimination.

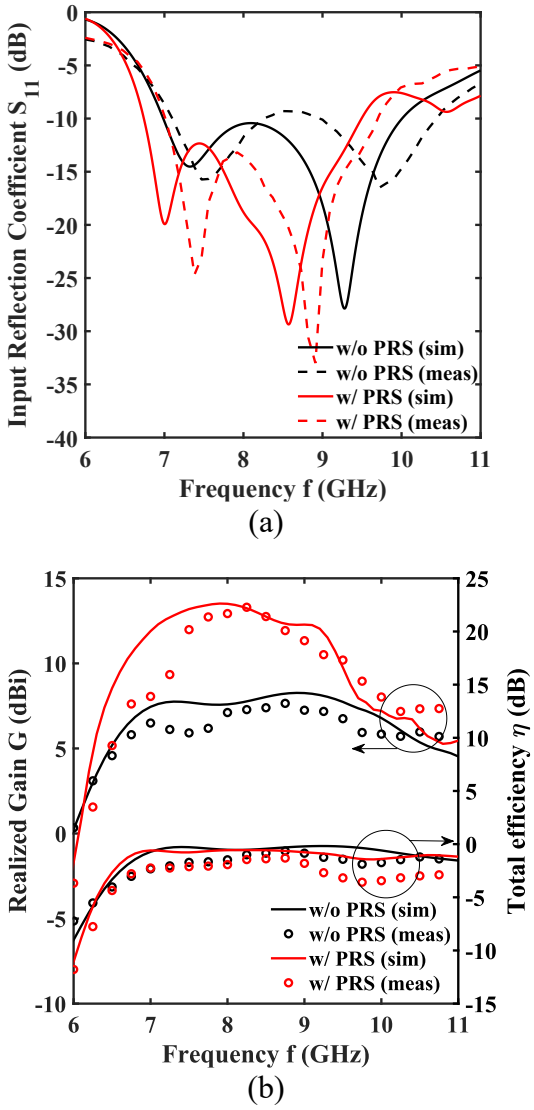

Figure. 6.6 a) Simulated (solid line) and measured (dashed line) input reflection coefficient $|S_{11}|$ as a function of the frequency f for the antenna without PRS (black line) and with PRS (red line); b) simulated (solid line) and measured (circle markers) realized gain G and total efficiency η as a function of the frequency f for the antenna without PRS (black) and with PRS (red) [167].

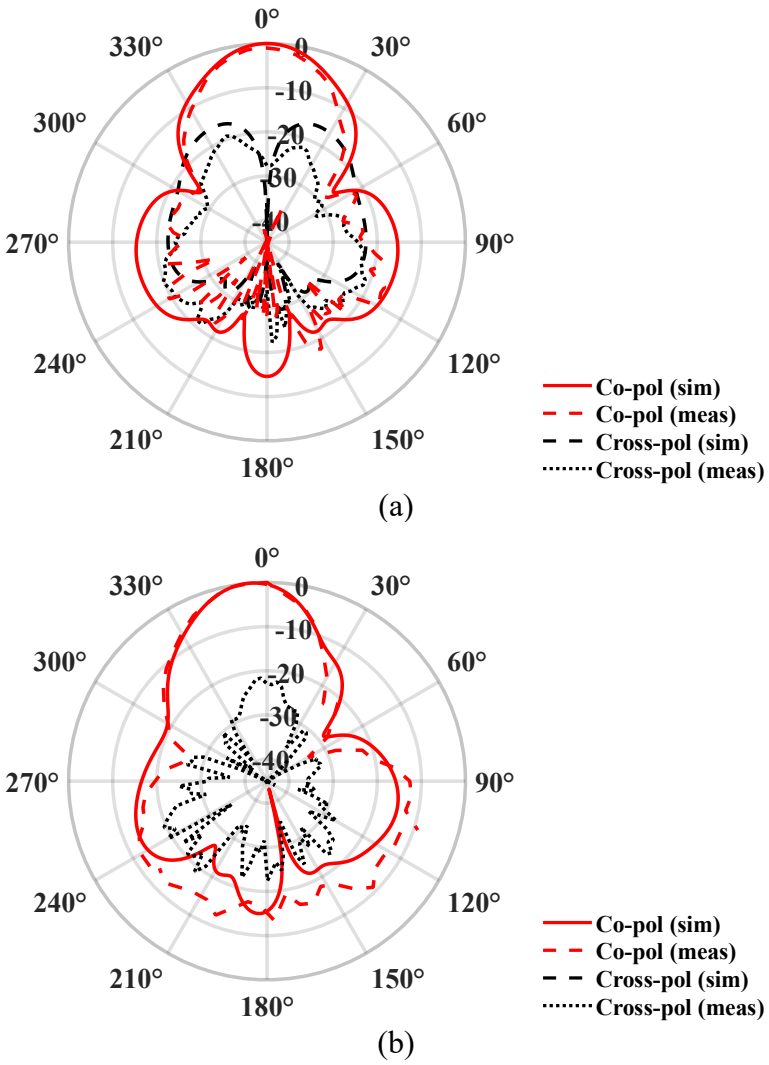

Figure. 6.7 Simulated and measured normalized radiation patterns at the frequency $f = 8\ GHz$ for the antenna with PRS in a) *H*-plane, b) *E*-plane [167].

6.5 Comparison with State of the Art

A comparison between simulation and measurement reveals slight deviations. These are likely attributed to fabrication tolerances, including factors such as inkjet printing precision, SMA pin position accuracy, alignment of the PRS layers, potential tilting of the top layer, and the use of conductive glue for connector attachment. Table 6.4 reports a comparison between the proposed FPA, and other conductive inkjet-printed antennas [89, 90, 171, 172]. Compared to [89], the proposed solution exhibits a smaller planar area and does not require a complex feed structure. With reference to [90] and [171], the wideband performance is traded for higher gain.

TABLE 6.4 COMPARISON WITH STATE-OF-THE-ART INKJET-PRINTED ANTENNAS

Ref.	**Size** $\boldsymbol{W \times L \times Z}$	**Imped.** $\boldsymbol{BW}(\%)$	**-3dB** $\boldsymbol{BW_G}$ (%)	**Max Gain** $\boldsymbol{G_{max}}$ $\boldsymbol{(dBi)}$	**Ap. Ef.** $\boldsymbol{\eta_{ap}}(\%)$
[89]	$2.5\lambda_0 \times 2.5\lambda_0 \times 0.05\lambda_0$	7.5	7.5	16.7	59.6
[90]	$1.6\lambda_0 \times 1.9\lambda_0 \times N.A.$	133	> 90	7.8	7.0
[171]	$1.3\lambda_0 \times 1.2\lambda_0 \times 0.01\lambda_0$	> 34	> 42	8.5	36.1
[172]	$1.0\lambda_0 \times 1.0\lambda_0 \times 0.04\lambda_0$	11.6	12	9.2	54.6
This work	$2.2\lambda_0 \times 2.2\lambda_0 \times 0.70\lambda_0$	31.3	24.7	13.2	36.2

6.6 Conclusion

In this chapter the design of a high-gain antenna based on Fabry-Pérot resonance is presented. The prototype is realized using a hybrid fabrication technique that combines inkjet printing and 3D printing. In particular, the PRS elements (square apertures and square patches) and the V-slot feed antenna are obtained by depositing conductive ink onto ultra-thin PET substrates with a mesoporous coating; while the dielectric PETG layers used for the PRS, and as spacers were fabricated via fused deposition modelling 3D printing. The measured results are in good agreement with the simulations. The maximum measured gain is $G_{max} = 13.2\ dBi$ at the frequency $f = 8.2\ GHz$. The measured impedance bandwidth is $BW_{\%} = 31.3\ \%$ and the -3 dB gain bandwidth is $BW_G = 24.5\%$ inside the impedance bandwidth. The obtained results are particularly promising, showing the possibility to construct complex antennas by employing low-cost and fast prototyping techniques, offering a valid alternative to expensive and rigid conventional manufacturing methods.

7 Design and Fabrication of a Transmitarray for Beam Steering

In this chapter, a low-profile dual-polarized Transmitarray Antenna (TA), made of three identical layers, is designed, fabricated, and characterized for the *Ku*-band range for beam-steering applications. The TA consists of 22×22 symmetrical Unit Cells (UCs). A 3-bit phase compensation layer with less than $\alpha_T = 1.3\,dB$ transmission loss and 2π transmission phase coverage for both linear polarized components at the central frequency $f_0 = 12\,GHz$ is designed. The fabricated TA exhibits a measured peak gain of $G_{m0} = 21\,dB$ and an aperture efficiency of $\eta_{ap,0} = 17\%$ at the frequency $f_0 = 12\,GHz$. The measured $-1\,dB$ gain bandwidth is $BW_G = 10.8\%$, covering the frequency range $f = 11.1 - 12.4\,GHz$. The TA can be used for beam steering up to an angle of $\gamma_{max} = \pm 30°$ with a measured scan loss $\triangle G_1 = 2.73\,dB$ at frequency $f_1 = 12.4\,GHz$.

7.1 Unit Cell Design

Rogers RT/duroid 5880 ($\varepsilon_r = 2.2$, and $tan\delta = 0.0009$) is used to design the UC with a substrate and metal thickness of $t_{sub} = 1.575\,mm$ and $t_{met} = 35\,\mu m$, respectively. The UC has a square shape with a periodicity of $P = 8.65\,mm$. Fig. 7.1 shows the top and side views of the proposed UC. The substrate and the metallization are represented in green and yellow colours, respectively. The UC is composed of three layers that are optimized to compensate the phase of the incident beam from the feed. A symmetric geometry is chosen to operate in a dual-polarization regime. The metallic layer consists of a ring with an outer radius R_1 and inner radius R_2, and an inner circle of radius R_3. Table 7.1 lists the ranges for optimizing the dimensions of the UC. Eight UCs are designed by changing the values of R_1, R_2, and R_3 to achieve a 3-bit phase compensation with low transmission loss. Table 7.2 reports the specific dimensions of the eight UCs with their corresponding transmission magnitude and phase.

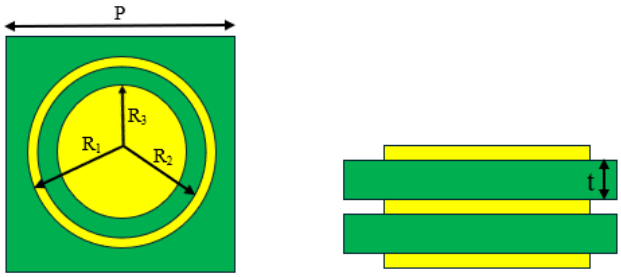

Figure. 7.1 a) Top and b) side views of the proposed UC [173].

TABLE 7.1 RANGES FOR GEOMETRICAL PARAMETER OPTIMIZATION.

Parameters	**Value**	**Description**
$P(mm)$	8.65	UC periodicity
$R_1(mm)$	$3.8 - 4.325$	Outer radius of metal ring
$R_2(mm)$	$3.7 - 4.225$	Inner radius of metal ring
$R_3(mm)$	$2.55 - 4.11$	Radius of inner circle
$t_{sub}(mm)$	1.575	Substrate thickness

TABLE 7.2 GEOMETRICAL DIMENSIONS FOR 3-BIT PHASE COMPENSATION.

UC No.	$\boldsymbol{R_1}$ $\boldsymbol{(mm)}$	$\boldsymbol{R_2}$ $\boldsymbol{(mm)}$	$\boldsymbol{R_3}$ $\boldsymbol{(mm)}$	$\boldsymbol{\lvert S_{2,1}\rvert}$ $\boldsymbol{(dB)}$	$\boldsymbol{\angle S_{2,1}}$ $\boldsymbol{(deg)}$
UC_1	4.325	4.225	4.11	-0.86	46
UC_2	4.325	4.225	4.07	-0.58	89
UC_3	4.325	4.225	3.96	-0.92	136
UC_4	4.20	4.10	3.83	-0.20	179.3
UC_5	4.25	4.15	3.60	-0.71	225
UC_6	4.325	4.20	3.07	-1.23	270.6
UC_7	4.20	4.10	2.63	-0.17	314
UC_8	3.80	3.70	2.55	-1.16	359.6

The CST Studio Suite Software is employed to design the UC and simulate the magnitude and the phase of the transmission coefficient for co-polarized components. The transmission coefficients correspond to the scattering parameter magnitude $|S_{2,1}|$ and phase $\angle S_{2,1}$ between ports 1 and 2. Due to the symmetry of the structure, the *x*- and *y*-polarized transmission coefficients are identical.

The Frequency-Domain Solver in CST Microwave Studio Suite has been used for the simulations, applying periodic boundary conditions along the *x*- and *y*-directions to simulate an infinite array, while open boundaries are imposed along the *z*-direction. The Floquet ports along the z-axis are used to excite the incident plane waves.

Fig. 7.2 plots a) the transmission magnitude $|S_{2,1}|$ and b) transmission phase $\angle S_{2,1}$ as a function of the frequency f for co-polarized components. The highest transmission loss, obtained at the frequency $f_0 = 12\ GHz$, is $\alpha_T = 1.23\ dB$, corresponding to UC_6. Fig 7.2 b) shows that the eight UCs cover the 3-bit phases required for co-polarized components at the frequency f_0. Fig. 7.2 c) plots the transmission magnitude $|S_{2,1}|$ as a function of the frequency f for cross-polarized components. The highest transmission magnitude value among all these cross-polarized components is about $-51\ dB$.

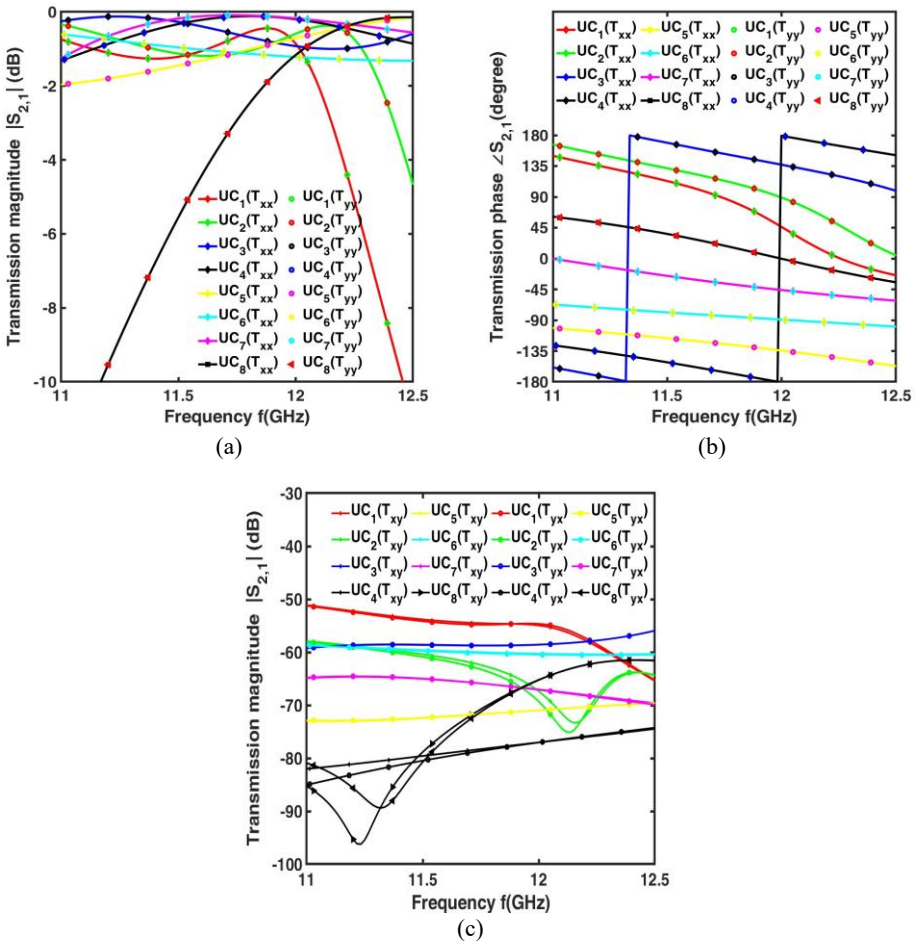

Figure 7.2 (a) Transmission magnitude $|S_{2,1}|$, and (b) transmission phase $\angle S_{2,1}$ as a function of frequency f for co-polarized components; (c) Transmission magnitude $|S_{2,1}|$ as a function of frequency f for cross-polarized components [173].

In TAs designed for beam steering purposes, it is crucial to investigate the UC behaviour when subjected to oblique incidence angles θ. For this purpose, the transmission magnitude and phase for the co-polarized components are simulated for different incidence angles θ. Fig. 7.3 plots a) the transmission magnitude $|S_{2,1}|$ and b) transmission phase $\angle S_{2,1}$ as a function of the frequency f for co-polarized components when an incident wave hits a UC at an incidence angle $\theta = 30°$. For $\theta = 30°$, the transmission phase is close to the value obtained at $\theta = 0°$ with a maximum simulated displacement of about $\triangle P = 20°$. Furthermore, the UCs will transmit the incidence ray in the proper direction with low transmission loss.

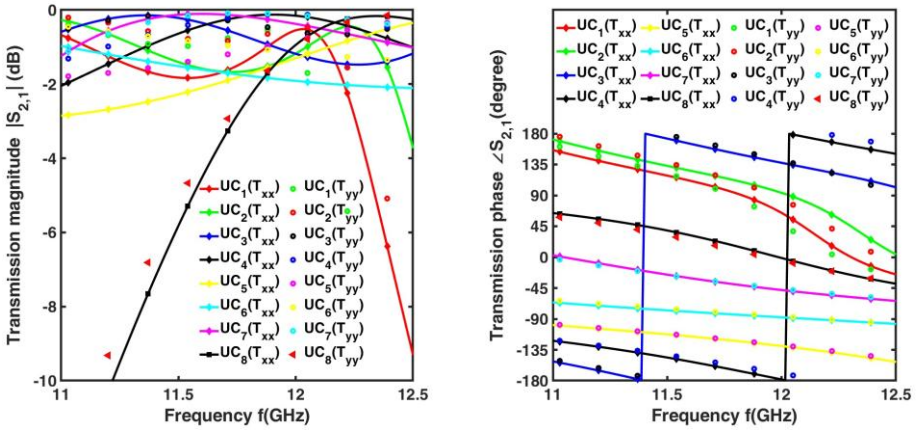

(a) (b)

Figure 7.3 (a) Transmission magnitude $|S_{2,1}|$, and (b) transmission phase $\angle S_{2,1}$ as a function of frequency f for co-polarized components for incident angle of $\theta = 30°$ [173].

An Equivalent Circuit Model (ECM) of the UC was developed using the same principle followed in the literature [174] for a better understanding of its operation. It was simulated with Advanced Design System (ADS) software, and the simulated S-parameters from ADS software were compared with those obtained by the CST simulations. Fig. 7.4 shows two adjacent UCs together with their ECM.

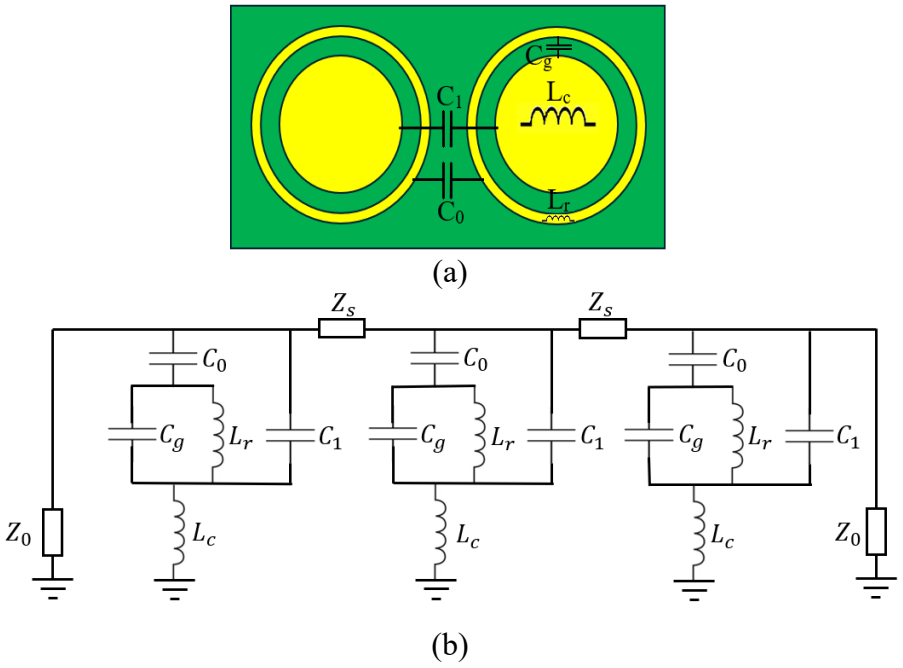

Figure 7.4 (a) Top layer of the two adjacent UCs and (b) ECM of the UC [173].

The inductive and capacitive properties of the metallic structure are represented by discrete components, such as capacitors and inductors. More specifically, the gap slot between the metal circle and the outer ring is represented by a capacitor C_g. The capacitive coupling between the metallic circles of two adjacent cells is represented by C_1. Similarly, the capacitive coupling between the outer metal rings of neighbouring UCs is modeled as C_0. Furthermore, the inductances of the inner circular patch and the outer ring are modeled by inductors L_c and L_r, respectively. The substrate is treated according to transmission line theory. It is modeled as a transmission line with a substrate impedance of $Z_S = Z_0/\sqrt{\varepsilon_r} = 255\ \Omega$, where $Z_0 = 377\ \Omega$ is the free-space impedance, and $\varepsilon_r = 2.2$ is the substrate dielectric constant.

UC_6 is chosen for computing the circuit component values of ECM. Table 7.3 lists the circuit component values of the ECM used to simulate the UC_6. These values are computed using a gradient-based optimization method by ADS software. The optimization aims to match the magnitude $|S_{2,1}|$, and the phase $\angle S_{2,1}$ of the scattering parameters obtained from CST by tuning the values of the circuit components, in the same frequency range. Fig. 7.5 plots a) the transmission magnitude $|S_{2,1}|$ and b) transmission phase $\angle S_{2,1}$ of UC_6 as a function of the frequency f obtained by CST (red solid curve) and ECM (blue dashed curve) simulations, confirming a good agreement between the two methods.

TABLE 7.3 CIRCUIT COMPONENTS VALUES OF THE ECM FOR UC_6

Parameters	**Value**	**Description**
$C_0\ (pF)$	0.323	adjacent ring coupling
$C_g\ (pF)$	0.042	gap capacitance
$C_1\ (pF)$	0.019	adjacent patch coupling
$L_r\ (nH)$	3.727	ring inductance
$L_c\ (nH)$	1.729	patch inductance

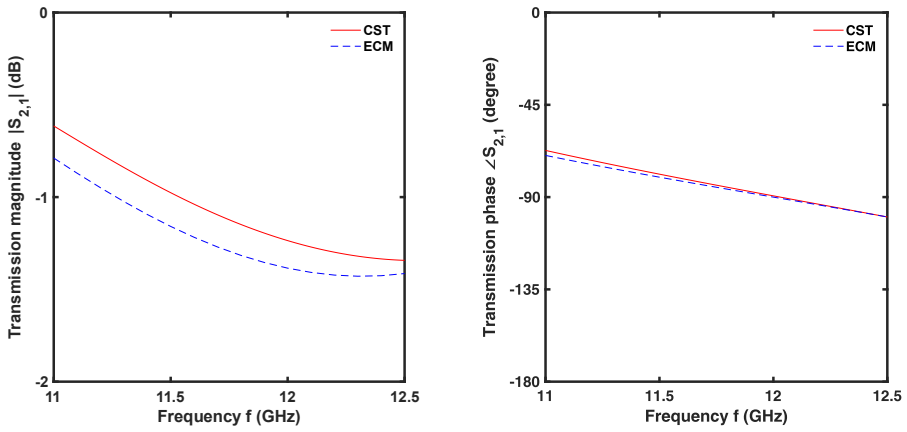

Figure 7.5 a) Transmission magnitude $|S_{2,1}|$, and b) transmission phase $\angle S_{2,1}$ of UC_6 as a function of frequency f obtained by CST (red solid curve) and ECM (blue dashed curve) simulation [173].

7.2 Transmitarray Antenna Design

The eight designed UCs are employed to implement a 22×22 element TA. Considering a UC periodicity of $P = 8.65\ mm$, and a focal length-to-diameter ratio of $F/D = 0.6$, the aperture size D and focal distance F of the TA are $D = 190.3\ mm$ and $F = 114.18\ mm$ respectively.

A Substrate Integrated Waveguide (SIW)-based 2×2 array antenna is selected as primary feed [175]. Fig. 7.6 shows a stack-up of the SIW feed antenna array. The SIW feed antenna array has been designed using two Rogers RT/duroid 5880 substrates ($\varepsilon_r = 2.2,\ tan\delta = 0.0009$) with thicknesses $T_1 = 0.381\ mm$, and $T_2 = 1.575\ mm$, respectively. The length and width of the substrates are $L = 35\ mm$, and $W = 35\ mm$, respectively. The complete list of parameters considered in the design is listed in [175].

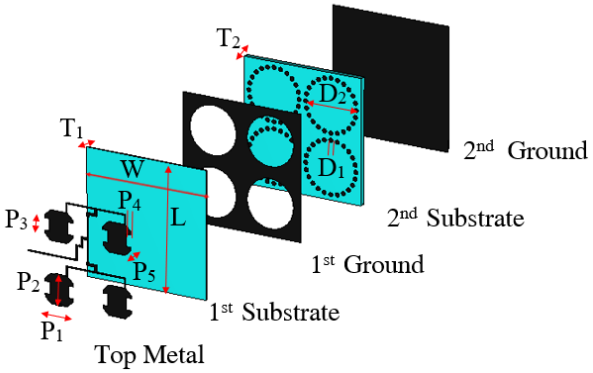

Figure 7.6 SIW feed antenna array stack-up [173].

This antenna has been chosen as the primary feed due to its $-10\ dB$ beamwidth of approximately $66°$, which aligns with the chosen F/D ratio and the target aperture size D. The SIW feed antenna array exhibits a bandwidth of $BW = 2.5\ GHz\ (10 - 12.5\ GHz)$ with an impedance bandwidth of $BWz = 20.83\%$. The peak gain values are $G_{f_0} = 12.93\ dB$ and $G_{f_1} = 12.83\ dB$ at frequencies $f_0 = 12\ GHz$ and $f_1 = 12.4\ GHz$, respectively [175].

A home-made software is used to calculate the 3-bit phase distribution of the TA. Fig. 7.7 shows the phase compensation profile required to achieve the broadside pointing direction $(\theta_0, \varphi_0) = (0°, 0°)$ assuming a focal distance of $F = 114.18\ mm$ and an operative frequency $f_0 = 12\ GHz$.

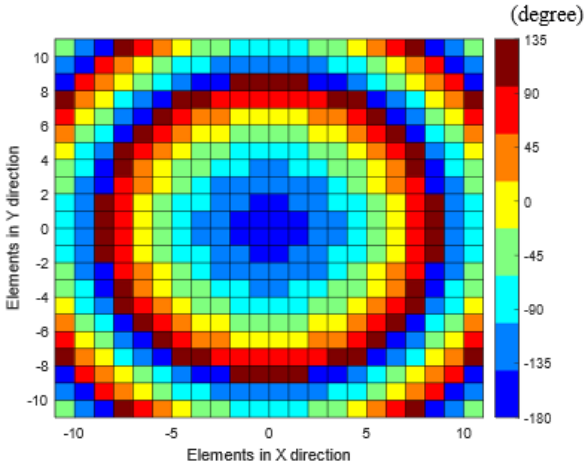

Figure 7.7 Phase compensation profile for the broadside pointing direction assuming a focal distance of $F = 114.18\ mm$ and operative frequency $f_0 = 12\ GHz$ [173].

7.3 Characterization and Discussion

The TA antenna has been fabricated and characterized. Fig. 7.8 shows the fabricated prototype in the anechoic chamber. Fig. 7.9 plots the simulated (red solid line) and measured (red dashed curve) peak gain G, along with the measured aperture efficiency (green solid line) as a function of frequency f. The figure shows that the simulated and measured realized peak gain values are $G_{s0} = 23.35\,dB$, and $G_{m0} = 21\,dB$, respectively, at frequency $f_0 = 12\,GHz$. Furthermore, at frequency $f_1 = 12.4\,GHz$, the simulated and measured peak gain values are $G_{s1} = 22.46\,dB$ and $G_{m1} = 19.97\,dB$, respectively.

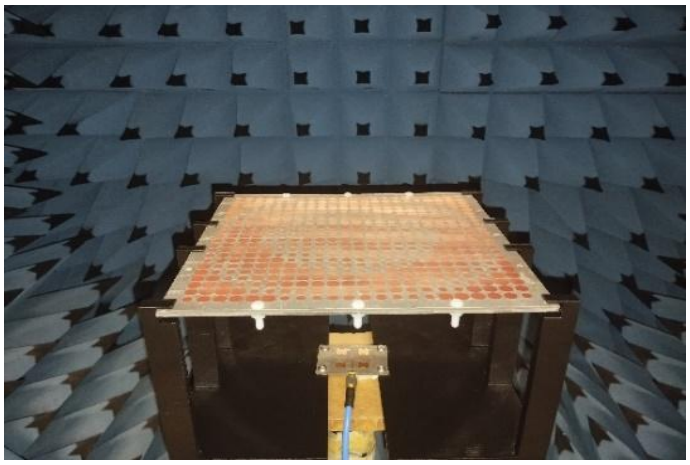

Figure 7.8 Fabricated prototype in the anechoic chamber [173].

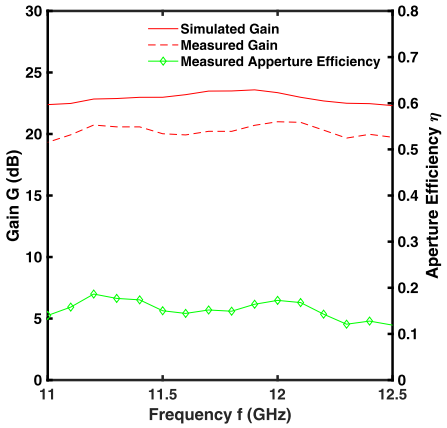

Figure 7.9 Simulated (red solid line) and measured (red dashed curve) peak gain G, along with the measured aperture efficiency η_{ap} (green solid line) as a function of frequency f [173].

The $-1\,dB$ gain bandwidth is $BW_G = 10.8\%$ in the frequency range $f = 11.1 - 12.4\,GHz$. Finally, the figure indicates that the measured aperture efficiency is $\eta_{ap,0} = 17\%$ and $\eta_{ap,1} = 13\%$ for frequencies $f_0 = 12\,GHz$ and $f_1 = 12.4\,GHz$, respectively, and that the highest measured aperture efficiency $\eta_{ap,max} = 19\%$ is reached at frequency $f_{max} = 11.2\,GHz$.

Fig. 7.10 shows the a) *E*- and b) *H*-plane of the simulated (green solid line) and measured (violet dashed line) radiation pattern as a function of the elevation angle θ at frequency $f_0 = 12\,GHz$.

Fig. 7.11 shows the a) *E*- and b) *H*-plane of the simulated (green solid line) and measured (violet dashed line) radiation pattern as a function of the elevation angle θ at frequency $f_1 = 12.4\,GHz$.

The measured peak gains at frequencies $f_0 = 12\ GHz$ and $f_1 = 12.4\ GHz$ are lower than the simulated ones by $\triangle G_0 = 2.35\ dB$ and $\triangle G_1 = 2.03\ dB$, in both *E*- and *H*- plane, respectively. The measured peak side lobe levels are $SLL_0 = -20.8\ dB$ and $SLL_1 = -18.5\ dB$ at frequencies $f_0 = 12\ GHz$ and $f_1 = 12.4\ GHz$, respectively.

This discrepancy can be attributed to higher insertion losses, due to a thin air layer between the substrates, which were not bonded together with prepreg, and other fabrication tolerances. Regarding the first aspect, it is worth noting that, in the design, the substrates are considered perfectly bonded, while in the prototype fabrication they were assembled with Teflon screws [173]. Consequently, the influence of an airgap with a thickness $t_{air} = 50\ \mu m$ between substrates in the UC has been investigated. Regarding the second aspect, to evaluate the effects of the fabrication tolerances, several simulations have been performed by slightly varying the optimized geometrical parameters of the eight UCs and the displacement of the focal distance F of the feed antenna along the z direction. All these variations confirmed a reduction in the realized gain [173].

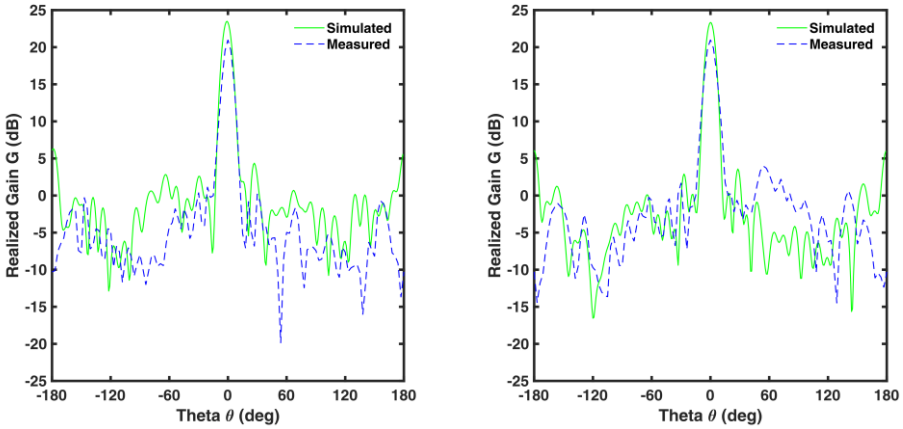

Figure 7.10 a) *E*- and b) *H*-plane of the simulated (green solid line) and measured (violet dashed line) radiation pattern as a function of the elevation angle θ at frequency $f_0 = 12\ GHz$ [173].

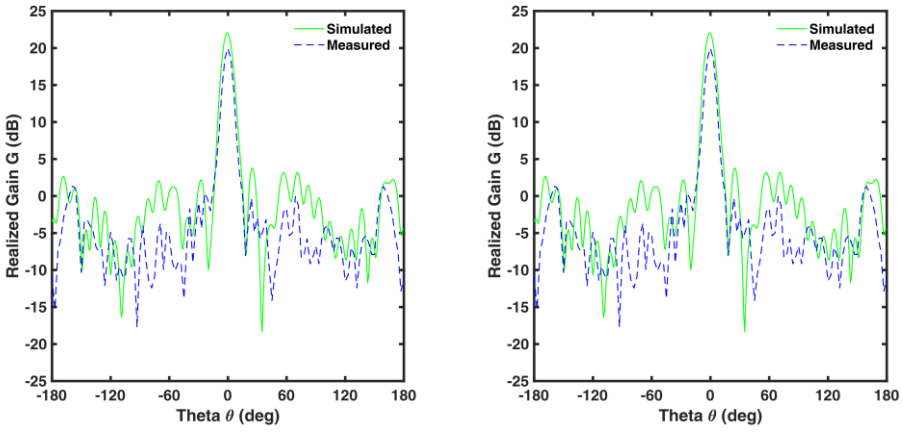

Figure 7.11 a) *E*- and b) *H*-plane of the simulated (green solid line) and measured (violet dashed line) radiation pattern as a function of the elevation angle θ at frequency $f_0 = 12.4\ GHz$ [173].

7.3.1 Beam Steering Performance

The beam-steering performance of the TA is investigated by moving the SIW feed antenna array. The feed antenna is shifted along the x-axis by discrete Feed Shifting Lengths (FSLs) in both positive and negative directions.

Fig. 7.12 plots the simulated (solid line) and measured (dashed line) farfield gain patterns G as a function of the elevation angle θ for different FSL values at frequencies a) $f_0 = 12\ GHz$,and b) $f_1 = 12.4\ GHz$. The figure shows good agreement between the simulated and measured patterns.

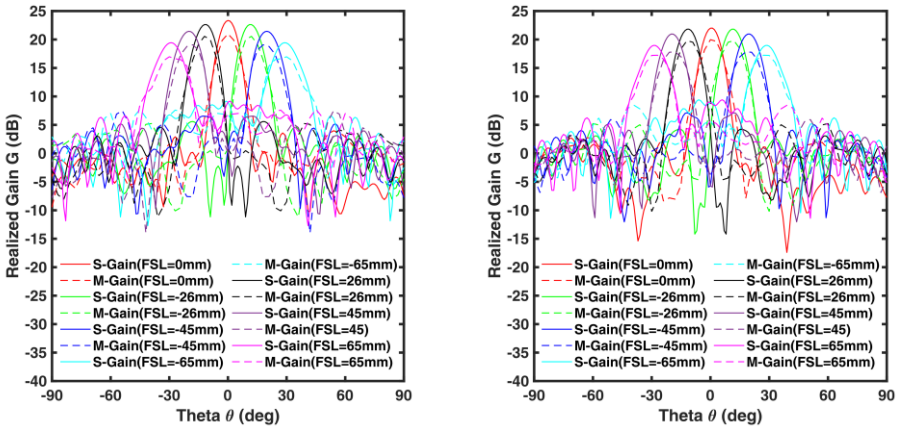

(a) (b)

Figure 7.12 Beam-steering performance: Simulated (solid lines) and measured (dashed lines) Farfield gain patterns G as a function of elevation angle θ for different FSL values at frequencies a) $f_0 = 12\ GHz$, and b) $f_1 = 12.4\ GHz$ [173].

It is worth noting that the required transverse displacement of the SIW feed is not related to the size of the TA unit cell. The FSL values were selected for the system characterization, in order to obtain specific steering angles, i.e. $\gamma_1 = \pm 10°$, $\gamma_2 = \pm 20°$, and $\gamma_3 = \pm 30°$.

Experimental results indicate that, for a steering angle of $\gamma_3 = \pm 30°$, the scan loss is $\triangle G_0 = 4.03\, dB$ and $\triangle G_1 = 2.73\, dB$ at frequencies $f_0 = 12\, GHz$ and $f_1 = 12.4\, GHz$, respectively. Furthermore, the figure shows that in all cases the measured gain is slightly lower than the simulated one, as previously observed and discussed. This discrepancy may be attributed to fabrication errors, and to the air gap between the adjacent layers.

7.4 Comparison with State of the Art

Table 7.4 presents a comparison between the proposed TA and the state of the art. The proposed structure exhibits a competitive trade-off in terms of low profile, reduced array size, and a low F/D ratio, compared to the state of the art [51, 79, 176-178]. Unlike [79, 176], the proposed design does not require an air gap, ensuring improved mechanical robustness. Moreover, the 3-bit phase quantization with less than $\alpha_T = 1.3\,dB$ transmission loss with dual-linear polarized components transmission capability is not achieved in [51, 176, 177]. Regarding the beam-steering capabilities, the proposed TA offers a scanning range of $\gamma_{max} = \pm 30°$, which is greater than [51] and [176], while achieving a lower scan loss compared to [79, 176-178], with a measured scan loss of $\triangle G_1 = 2.73\,dB$ at frequency $f_1 = 12.4\,GHz$. However, the aperture efficiency η_{ap} is not better in comparison with the reference papers reported in Table 7.4, except [53].

TABLE 7.4 COMPARISON WITH STATE-OF-THE-ART BEAM-STEERING TAs

Ref.	**[51]**	**[79]**	**[176]**	**[177]**	**[178]**	**This work**	
Freq. $f(GHz)$	12.5	15	27.5	10	12	12	12.4
No. of Layers	3	3	2	3	5	3	3
Thickness ρ (λ_0)	0.083	0.165	0.18	0.133	0.582	0.126	0.13
Array Size A (λ_0^2)	90.9	38.48	86.06	16.0	64.0	57.9	62.35
Gain G (dB)	22.7	23.06	24.2	19.3	23.0	21.0	19.97
Scan Range γ_{max} (deg)	± 21	± 30	± 27	$+60$	± 35	± 30	± 30
Scan Loss ΔG (dB)	2.7	3.6	3.7	4.15	3.0	4.03	2.73
F/D	0.59	0.75	0.50	0.60	0.78	0.60	0.60
Polarization	*Single LP*	*Dual LP/CP*	*Dual LP*	*Single CP*	#	*Dual LP*	*Dual LP*
Side Lobe Level SLL (dB)	-15.0	-35.0	-18.4	-17.7	-15.0	-20.8	-18.5
Phase States	360°	360°	240°	180°	360°	360°	360°
Air Gap	*No*	*Yes*	*Yes*	*No*	*No*	*No*	*No*
Aperture Efficiency $\eta_{ap}(\%)$	15.2	42.3	24.5	40.2	34.64	17.0	13.0

7.5 Conclusion

This chapter presents the design, fabrication, and characterization of a TA for beam-steering applications. The proposed structure features a low profile ($0.126\lambda_0$), dual-polarized operation, and efficient beam steering up to $\gamma_{max} = \pm 30°$. Specifically, low scan losses of $\triangle G_0 = 4.03\,dB$ and $\triangle G_1 = 2.73\,dB$ have been measured at frequencies $f_0 = 12\,GHz$ and $f_1 = 12.4\,GHz$, respectively. Furthermore, the measured peak gain is $G_{m0} = 21\,dB$ at frequency $f_0 = 12\,GHz$ with an aperture efficiency of $\eta_{ap,0} = 17\%$, reaching a maximum aperture efficiency of $\eta_{ap,max} = 19\%$ at frequency $f_{max} = 11.2\,GHz$. Finally, the $-1\,dB$ gain bandwidth of $BW_G = 10.8\%$ is achieved in the frequency range $f = 11.1 - 12.4\,GHz$, and a measured peak side lobe level $SLL_1 = -20.8\,dB$ at frequency $f_0 = 12\,GHz$ is obtained. These characteristics render the proposed TA suitable for Ku-band satellite and 5G communications.

8 Dual-Linear-Polarized Folded Transmitarray Antenna Operating in *Ka*-Band

This chapter illustrates the design and optimization of a compact DLP-FTA operating in the *Ka*-band. The proposed system consists of a TA layer, a reflector plane, and a horn feed antenna embedded within the reflector plane. The TA layer is composed of 14×14 symmetrical UCs, and each of them is designed to operate in the DLP regime at the same frequency. The proposed UCs provide a transmission coefficient of about $-3dB$ and full 2π phase coverage. The complete DLP-FTA exhibits a simulated maximum realized gain of $G = 23.2\ dB$ and an aperture efficiency of $\eta_{ap} = 58.8\ \%$ at the frequency $f = 26\ GHz$. Furthermore, the proposed DLP-FTA exhibits a relative impedance bandwidth of $BW = 14\%$, and a $-3dB$ gain bandwidth of $BW_G = 7.3\%$. These radiative characteristics are particularly promising, making this device a competitive candidate for high-performance applications, including *Ka*-band satellite links and 5G networks. The DLP-FTA fabrication will be completed by assembling different parts of the structure obtained via LPKF ProtoLaser U3 prototyping equipment. A proper characterization will be performed to test the actual performance.

8.1 Unit Cell Design

For the design a Rogers Duroid RT 5880 substrate ($\epsilon = 2.2$, $tan\ (\delta) = 0.0009$ @10 GHz) with a thickness of $h_{sub} = 0.787\ mm$ and a copper metallic layer with a thickness of $h_{cop} = 35\ \mu m$ is considered. The CST Studio Software has been employed for simulations. A multilayer solution has been proposed for the design of the UCs employed in the TA layer, see Fig. 2.7. Fig. 8.1 shows the stack-up composed of three dielectric layers with four metallic elements.

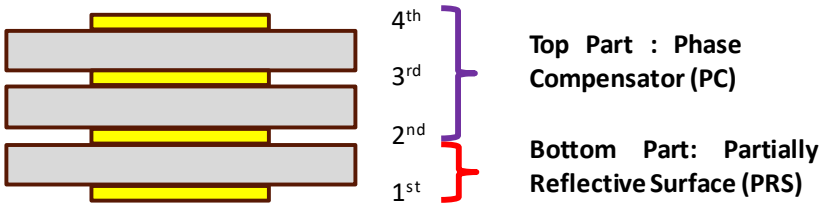

(b)

Figure. 8.1 a) Stack-up of the UC employed in TA layer.

The bottom part of the UC is a PRS, implemented as a metasurface based on DSRRs [68] coupled with a Modified Double Cross Dipole (MDCD). The DSRR-MDCD allows to divide the power of the x-polarized (or y-polarized) incident wave into reflected and transmitted co-polarized components, ensuring that the cross-polarized components are negligible. The geometry was optimized through a trial-and-error process until the amplitude of the co-polarized transmission and reflection coefficients reached equal levels of approximately -6 dB,

while the cross-polarized components were minimized. The top part of the UC is a PC, and it is designed employing the method reported in [70]. The shape of the metamaterial is based on the Jerusalem cross [70].

8.1.1 Bottom Part: Partially Reflective Surface

Fig. 8.2 shows the PRS geometry of the UC with the pertaining geometrical parameters. It is composed of one dielectric and one metallic layer. The PRS geometry is the same for the four UCs for 2-bit phase compensation. This novel and sophisticated pattern allows a higher degree of freedom in the design, and a stronger inductive and capacitive coupling between the different metallic parts. Table 8.1 lists the optimized values of the geometrical parameters of the PRS layer.

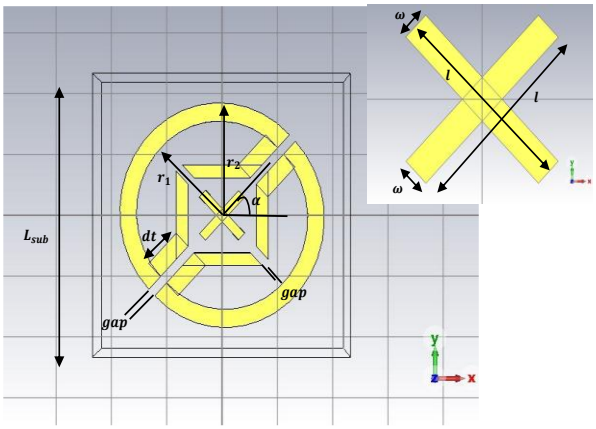

Figure. 8.2 Geometry of PRS layer of the UC with the pertaining geometrical parameters including a zoom of the central part (in the corner).

TABLE 8.1 PRS LAYER OF UC: GEOMETRICAL PARAMETERS

Parameters	**Value**	**Description**
$L_{sub}\ (mm)$	4.5	Length substrate
$gap\ (mm)$	0.15	Split ring resonator gap
$\alpha\ (deg)$	45	Rotation angle
$r_1\ (mm)$	1.50	Inner radius
$r_2\ (mm)$	1.85	Outer radius
$dt\ (mm)$	0.70	Inset length
$\omega\ (mm)$	0.15	Cross width
$l\ (mm)$	1	Cross length

Fig. 8.3 (a) shows the simulated transmission and reflection magnitudes of the co-polarized components for the PRS of the UC. In particular, the reflection magnitude $|S_{11}|$ (red curves) and the transmission magnitude $|S_{21}|$ (black curves) as a function of the frequency f for the co-polarized components are reported, for both the *x*-polarized incident wave (solid curves) and the *y*-polarized incident wave (dashed curves) At the frequency $f = 27\ GHz$, the reflection and transmission magnitudes are about $|S_{21}| \simeq |S_{11}| = -3dB$ for both co-polarized components.

Fig. 8.3 (b) shows the simulated transmission and reflection magnitudes of the cross-polarized components for the PRS of the UC. In particular, the reflection magnitude $|S_{11}|$ (red curve) and $|S_{12}|$ transmission magnitude (black curves) as a function of the frequency f for the cross-polarized components are reported, for both the *x*-polarized incident wave (dash-dotted curve), and the *y*-polarized incident wave (dotted curve). At the frequency $f = 27\ GHz$, the cross-polarized components are less than $-20\ dB$, indicating that they are negligible.

Fig. 8.3 (c) shows the simulated transmission phase $\phi(S_{21})$ of the co-polarized components as a function of the frequency f for the PRS of the UC, for the *x*-polarized incident wave (solid green curve) and the *y*-polarized incident wave (dashed blue curve). The figure shows an excellent overlap in the range of interest. At the frequency $f = 27\ GHz$, the transmission phase is $\phi(S_{21}) = -72°$ for both co-polarized components.

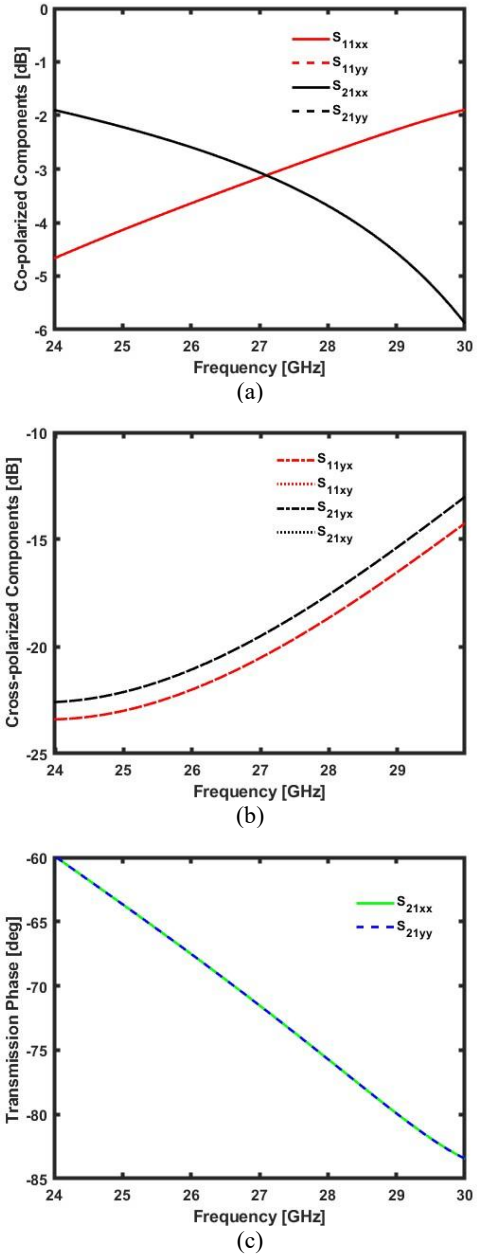

Figure 8.3 Reflection magnitude $|S_{11}|$ (red curves) and transmission magnitude $|S_{21}|$ (black curves) as a function of the frequency f for: a) co-polarized components for *x*-polarized (solid curves) and *y*-polarized (dashed curves) incident waves; and b) cross-polarized components for *x*-polarized (dash-dotted curves) and *y*-polarized (dotted curves) incident waves. c) Transmission phase $\phi(S_{21})$ as a function of the frequency f for co-polarized components for *x*-polarized (solid green curve) and *y*-polarized (dashed blue curve) incident waves.

8.1.2 Top Part: Phase Compensator

The shape of the metasurface is based on the Jerusalem cross [70]. Equations (2.62) - (2.63) are implemented in a home-made software, providing the theoretical values of admittance Y_{s1}, and Y_{s2}, see Fig 2.7.

Fig. 8.4 shows the transmission (a) magnitude and (b) phase as a function of admittances Y_{s1} and Y_{s2}, at the frequency $f = 27\ GHz$. These theoretical values allow obtaining the desired phase of the transmitted waves by indicating an inductive or capacitive effect of each metallic layer. As previously underlined, in Fig. 8.3 (c) the PRS of the UC introduces a transmitted phase $\phi(S_{21}) = -72°$ at the frequency $f = 27\ GHz$. This value is taken into account for obtaining the total phase of the complete UC.

Table 8.2 reports the theoretical values of admittances Y_{s1} and Y_{s2} in order to obtain the transmission magnitude $|S_{21}| \cong 1$, and the desired phase for 2-bit phase compensation for *x*-polarized and *y*-polarized incident waves, taking into account the PRS phase contribution of $\phi(S_{21}) = -72°$.

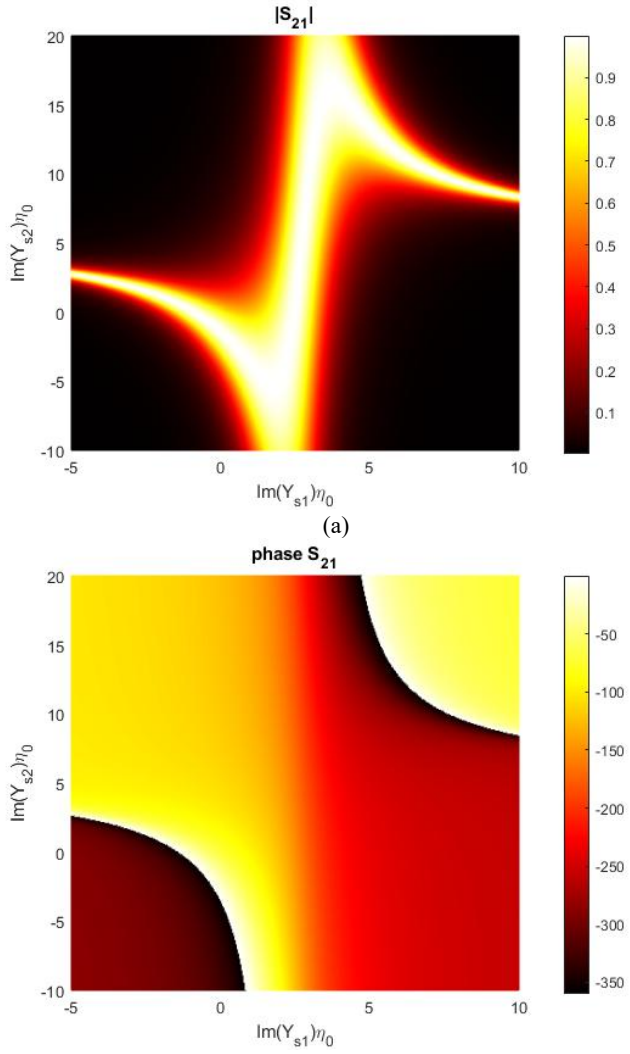

Figure 8.5 Transmission a) magnitude and b) phase as a function of admittance Y_{s1} and Y_{s2} at the frequency $f = 27\ GHz$.

Fig. 8.5 (a) illustrates the geometry and geometrical parameters under optimization in the design of the PC of the UCs. Fig. 8.5 (b) shows the shape of the metamaterial employed in PC of the UCs for transmitted phases $\phi = 0°$ and $\phi = -270°$. Fig. 8.5 (c) shows the shape of metamaterial employed in the PC of the UCs for transmitted phases $\phi = -90°$ and $\phi = -180°$. In particular for transmitted phase $\phi = -90°$ and $\phi = -180°$, a single Jerusalem cross has been considered in Y_{s1}, and Y_{s2} layers; for transmitted phases $\phi = 0°$ and $\phi = -270°$, a single Jerusalem cross has been considered in the layer Y_{s2}, and four Jerusalem Crosses in the layer Y_{s1}, due to the high capacitance required, see Table 8.2.

TABLE 8.2 STACK-UP #02 PC: THEORETICAL Y_{s1} AND Y_{s2} VALUES FOR 2-BIT PHASE COMPENSATION

Desired Phase $(\boldsymbol{deg})$	$\boldsymbol{Im(Y_{s1}^{ii})\eta}$	$\boldsymbol{Im(Y_{s2}^{ii})\eta}$	$\boldsymbol{\lvert S_{21}^{ii}\rvert}$ $(\boldsymbol{linear})$	$\angle S_{2,1}^{ii}(\boldsymbol{deg})$
$\mathbf{0°}$	3.26	9.48	0.99	-288
$\mathbf{-90}$	-3.39	1.67	0.99	-18
$\mathbf{-180°}$	1.23	-2.24	0.99	-108
$\mathbf{-270°}$	2.06	6.22	0.99	-200

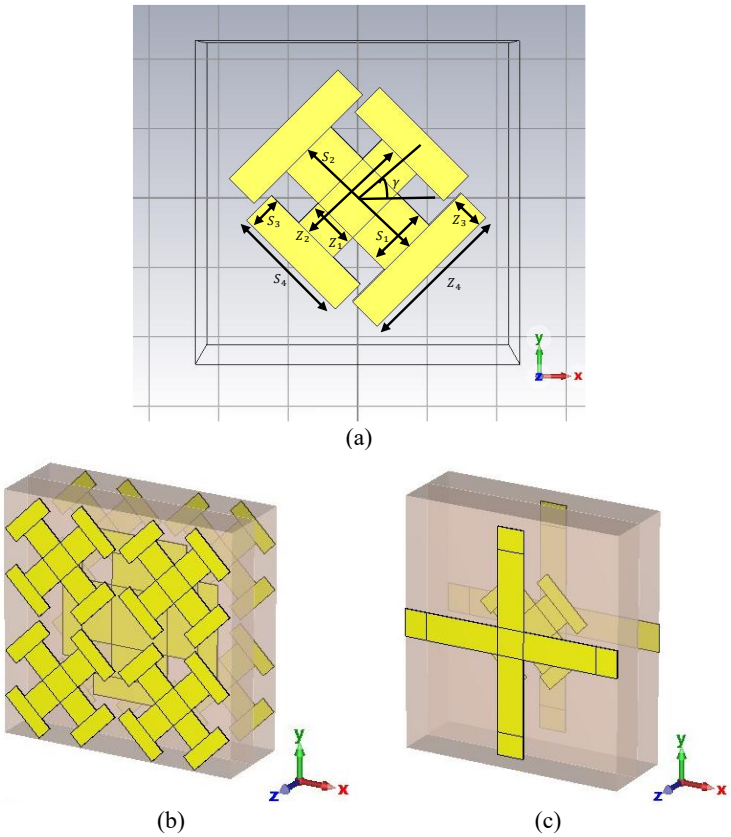

(a)

(b) (c)

Figure 8.5 a) Jerusalem cross employed in the Y_{s1} and Y_{s2} layers of the PC of UC with geometrical parameters. Shape of the metamaterial employed in PC of UC for transmitted phases b) $\phi = 0°,\ \phi = -270°$; and c) $\phi = -90°, \phi = -180°$.

This geometry has been preliminarily optimized via UC simulations, considering only the presence of the PC (neglecting the PRS), according to Grbic theory [70]. A set of preliminary geometrical dimensions has been obtained for each PC of the four UCs in order to balance the phase contribution of the PRS. The results are not presented here for the sake of shortness. These preliminary geometrical parameters were further tuned to obtain the required phases, by considering UC simulations, including the PRS and the PC.

8.1.3 Complete UC Design

Table 8.3 reports the optimized geometrical parameters for the complete UC, including the PRS and the PC for 2-bit phase compensation. For each transmitted phase ϕ, the optimized values are reported for the PRS and two sub-columns corresponding to Y_{s1} and Y_{s2} layers for the PC. In the following paragraph, the four UCs will be referred to as UC_{0}, UC_{-90}, UC_{-180},and UC_{-270}, the subscript indicating the transmission phase (0°, -90°, - 180°, -270°) of the scattering parameters $\phi(S_{21})$ for the co-polarized components.

TABLE 8.3 OPTIMIZED VALUES FOR STACK-UP #02: PRS-PC FOR 2 BIT PHASE COMPENSATION

Symbol	$\boldsymbol{UC_0}$ $(\boldsymbol{\phi = 0°})$		$\boldsymbol{UC_{-90}}$ $(\boldsymbol{\phi = -90°})$		$\boldsymbol{UC_{-180}}$ $(\boldsymbol{\phi = -180°}$		$\boldsymbol{UC_{-270}}$ $(\boldsymbol{\phi = -270°})$	
	$\boldsymbol{Y_{s1}}$	$\boldsymbol{Y_{s2}}$	$\boldsymbol{Y_{s1}}$	$\boldsymbol{Y_{s2}}$	$\boldsymbol{Y_{s1}}$	$\boldsymbol{Y_{s2}}$	$\boldsymbol{Y_{s1}}$	$\boldsymbol{Y_{s2}}$
$L_{sub}(mm)$	4.5		4.5		4.5		4.5	
$gap(mm)$	0.15		0.15		0.15		0.15	
$\alpha(deg)$	45°		45°		45°		45°	
$r_1(mm)$	1.5		1.47		1.46		1.38	
$r_2(mm)$	1.8		1.82		1.81		1.78	
$dt(mm)$	0.7		0.7		0.6		0.6	
$\omega(mm)$	0.15		0.15		0.15		0.15	
$l(mm)$	1		1		1		1	
$S_1(mm)$	0.25	0.73	0.45	0.85	0.8	0.2	0.55	1.07
$S_2(mm)$	1.27	2.55	3.6	1.20	1.7	3.3	1.52	2.3
$S_3(mm)$	0.36	0.57	0.45	0.3	0.4	0.4	0.3	0.39
$S_4(mm)$	1.14	3.69	0.45	0.85	1.75	0.75	0.94	1.84
$Z_1(mm)$	0.25	0.73	0.45	0.65	0.5	0.2	0.5	1.07
$Z_2(mm)$	1.27	2.55	3.6	1.20	1.5	3.3	1.52	2.3
$Z_3(mm)$	0.36	0.57	0.45	0.3	0.4	0.4	0.3	0.39
$Z_4(mm)$	1.14	3.69	0.45	1	1.3	0.75	0.94	1.84
$\gamma(deg)$	0°	0°	0°	45°	45°	0°	45°	0°

Fig. 8.6 (a) shows the simulated transmission and reflection magnitudes of the co-polarized components for UC_0. In particular, the reflection magnitude $|S_{11}|$ (red curves) and the transmission magnitude $|S_{21}|$ (black curves) as a function of the frequency f for the co-polarized components are reported, for both the *x*-polarized incident wave (solid curves) and the *y*-polarized incident wave (dashed curves). At the frequency $f = 27\ GHz$, the reflection and transmission magnitudes are about $|S_{21}| \simeq |S_{11}| = -3.3dB$ for both co-polarized components.

Fig. 8.6 (b) shows the simulated transmission and reflection magnitudes of the cross-polarized components for UC_0. In particular, the reflection magnitudes $|S_{11}|$ (red curve) and the transmission magnitude $|S_{21}|$ (black curves) as a function of the frequency f for the cross-polarized components are reported, for both the *x*-polarized incident wave (dash-dotted curve), and the *y*-polarized incident wave (dotted curve). At the frequency $f = 27\ GHz$, the cross-polarized components are about $-15\ dB$, indicating that they are negligible.

Fig. 8.6 (c) shows the simulated transmission phase $\phi(S_{21})$ of the co-polarized components as a function of the frequency f for UC_0, for the *x*-polarized incident wave (solid green curve) and the *y*-polarized incident wave (dashed blue curve). The figure shows an excellent overlap in the range of interest. At the frequency $f = 27\ GHz$, the transmission phase is $\phi(S_{21}) = -14°$ for both co-polarized components.

Figs. 8.7-8.9 report the same physical quantities for the UC_{-90}, UC_{-180}, UC_{-270}. Specifically, the co-polarized components (panel 'a' in each figure) show that the reflection and transmission magnitudes are about $|S_{21}| \simeq |S_{11}| = -3dB$ at the frequency $f = 27\ GHz$. Regarding the cross-polarized components (panel 'b' in each figure), the reflection and transmission magnitudes are kept below $-12\ dB$ at the frequency $f = 27\ GHz$, confirming that the cross-polarization components are negligible. Finally, the transmission phase $\phi(S_{21})$ (panel 'c' in each figure) shows the required progressive phase shifts, i.e. $\phi(S_{21}) = \{-90°; -180°; -270°\}$. Together, the four UCs provide a full 2π phase coverage.

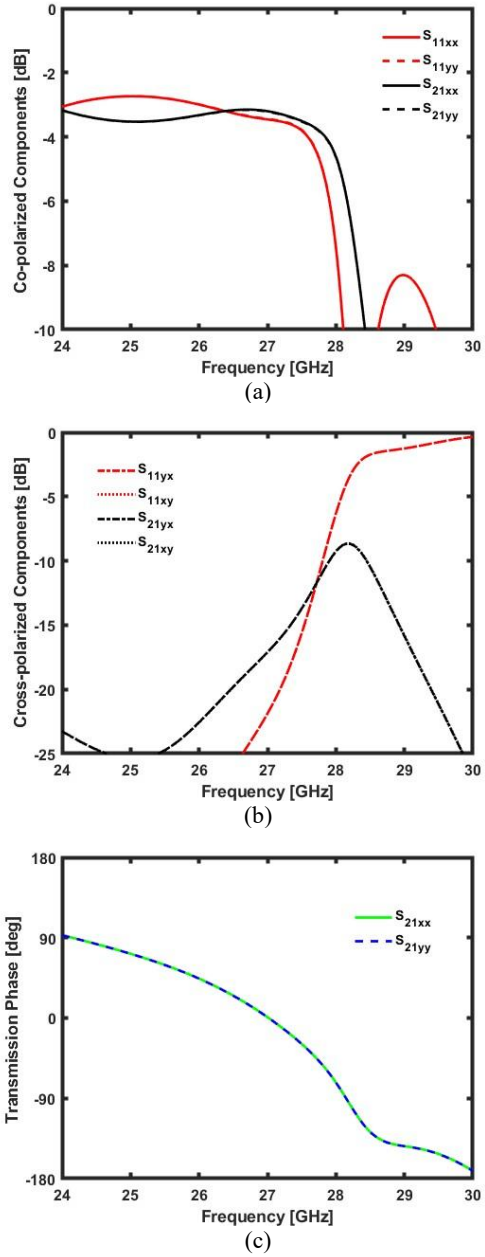

Figure 8.6 UC_0 simulation. Reflection magnitude $|S_{11}|$ (red curves) and transmission magnitude $|S_{21}|$ (black curves) as a function of the frequency f for: a) co-polarized components for *x*-polarized (solid curves) and *y*-polarized (dashed curves) incident waves; and b) cross-polarized components for *x*-polarized (dash-dotted curves) and *y*-polarized (dotted curves) incident waves. c) Transmission phase $\phi(S_{21})$ as a function of the frequency f for co-polarized components for *x*-polarized (solid green curve) and *y*-polarized (dashed blue curve) incident waves.

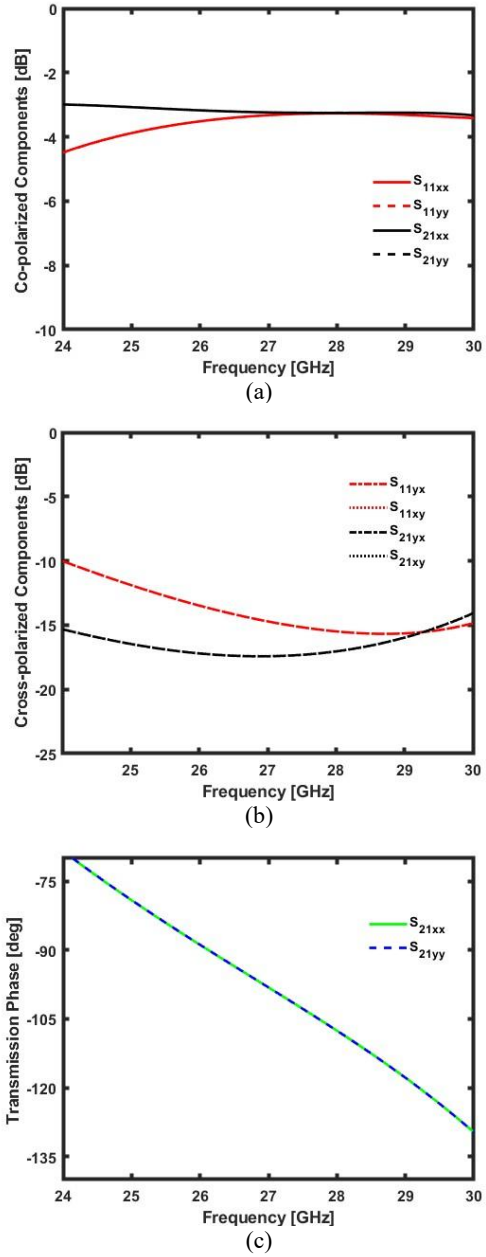

Figure 8.7 UC_{-90} simulation. Reflection magnitude $|S_{11}|$ (red curves) and transmission magnitude $|S_{21}|$ (black curves) as a function of the frequency f for: a) co-polarized components for *x*-polarized (solid curves) and *y*-polarized (dashed curves) incident waves; and b) cross-polarized components for *x*-polarized (dash-dotted curves) and *y*-polarized (dotted curves) incident waves. c) Transmission phase $\phi(S_{21})$ as a function of the frequency f for co-polarized components for *x*-polarized (solid green curve) and *y*-polarized (dashed blue curve) incident waves.

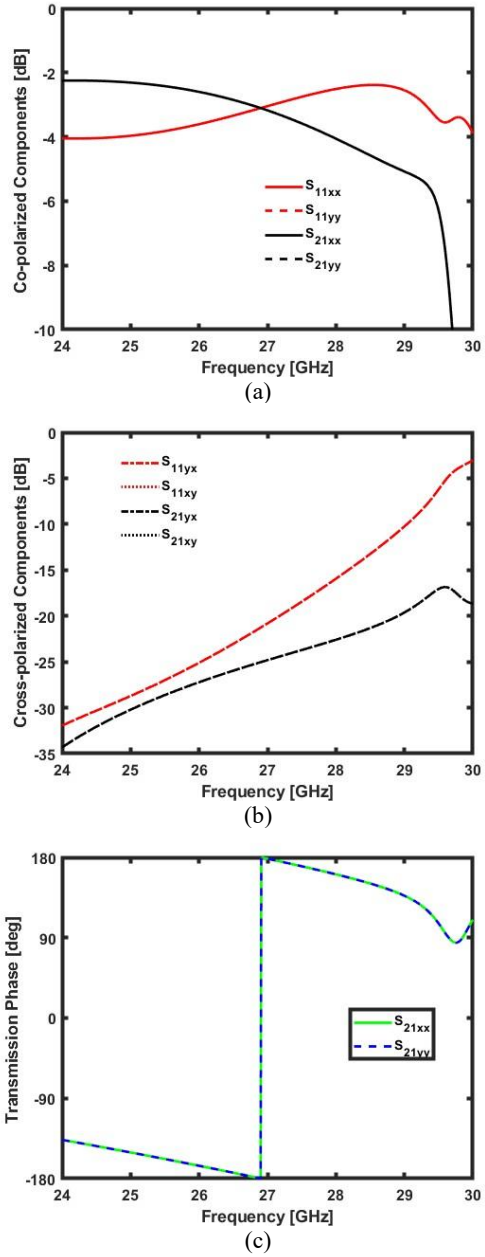

Figure 8.8 UC_{-180} simulation. Reflection magnitude $|S_{11}|$ (red curves) and transmission magnitude $|S_{21}|$ (black curves) as a function of the frequency f for: a) co-polarized components for *x*-polarized (solid curves) and *y*-polarized (dashed curves) incident waves; and b) cross-polarized components for *x*-polarized (dash-dotted curves) and *y*-polarized (dotted curves) incident waves. c) Transmission phase $\phi(S_{21})$ as a function of the frequency f for co-polarized components for *x*-polarized (solid green curve) and *y*-polarized (dashed blue curve) incident waves.

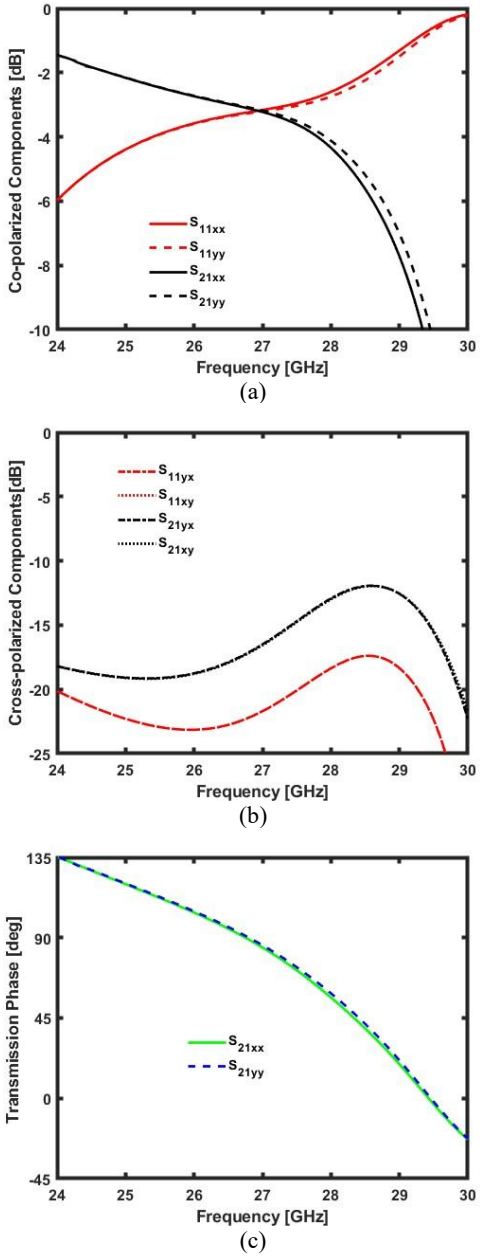

Figure 8.9 UC_{-270} simulation. Reflection magnitude $|S_{11}|$ (red curves) and transmission magnitude $|S_{21}|$ (black curves) as a function of the frequency f for: a) co-polarized components for *x*-polarized (solid curves) and *y*-polarized (dashed curves) incident waves; and b) cross-polarized components for *x*-polarized (dash-dotted curves) and *y*-polarized (dotted curves) incident waves. c) Transmission phase $\phi(S_{21})$ as a function of the frequency f for co-polarized components for *x*-polarized (solid green curve) and *y*-polarized (dashed blue curve) incident waves.

8.2 Folded Transmitarray Antenna

A horn antenna Narda ATM-28-441 has been considered as feed. The actual geometrical dimensions of the feed [179] and of the rectangular waveguide WR28 [180] are considered for the modelling in CST Studio Software.

Fig. 8.10 (a) shows a comparison between the normalized simulated gain G_N of the horn antenna (dashed blue curve) and the function $cos^q\ \theta$ (solid black curve) as a function of the elevation angle θ for azimuth angle $\phi = 90°$. The optimal exponent to obtain a closed form approximation of G_N is $q_{opt} = 13.3$.

Fig. 8.10 (b) shows the spillover efficiency η_{spill}, the illumination efficiency η_{ill} and the total efficiency η_{tot} as a function of the ratio F/D, for the optimum exponent $q_{opt} = 13.3$, obtained via equations (2.52) - (2.54). The ratio F/D that maximizes the total efficiency is the range $F/D = 1.1 \div 1.3$. The maximum total efficiency is $\eta_{tot} = 0.74$ for $F/D = 1.2$.

Fig. 8.11 shows the scheme of the DLP-FTA with dual phase compensation regions. The 2-bit phase compensation for both *x*-polarized and *y*-polarized incident waves has been obtained using the equation (2.50).

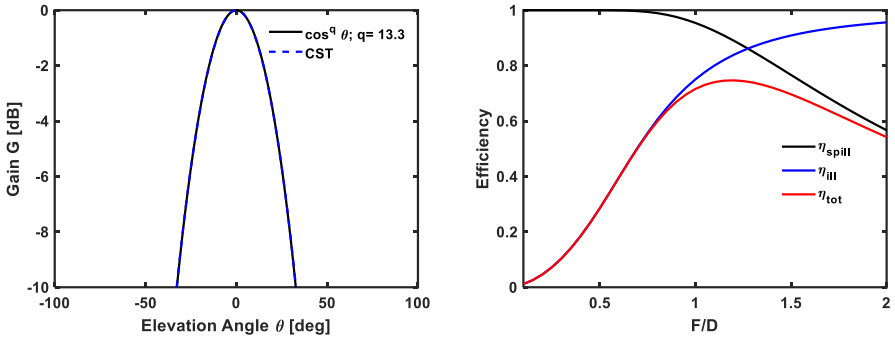

(a) (b)

Figure 8.10 a) Comparison between the normalized simulated gain G_N of the horn antenna (dashed blue curve) and the function $cos^q\,\theta$ (solid black curve) as a function of the elevation angle θ in dB scale, for azimuth angle $\phi = 90$. b) Spillover η_{spill} (black curve), illumination η_{ill} (blue curve), and total η_{tot} (red curve) efficiencies as function of the ratio F/D, for the optimum exponent $q_{opt} = 13.3$.

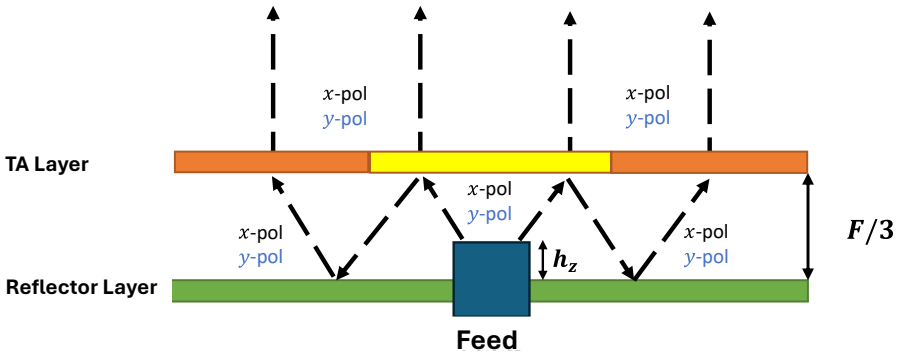

Figure 8.11 Scheme of DLP-FTA with dual phase compensation regions.

Fig. 8.12 shows the 2-bit phase compensation of the TA layer of the DLP-FTA. Two regions are considered in the design: *i)* the central region, consisting of 4×4 UCs; and *ii)* the external region, consisting of 10×10 UCs. The central region, within the grey square, is made up of UC_{-90}, as required by the distribution phase calculated via equation (2.49) considering a focal distance (or propagation path) $F/3$ and a phase $\phi_r = 0°$. Conversely, a focal distance F (or propagation path) and a phase $\phi_r = 180° + 135°$ are used for the phase compensation of the external region, after a double reflection in the TA cavity. Here, the reflection phase of the ground plane is $180°$, while the reflection phase $\phi(S_{11})$ of the unit cell UC_{-90} is $-135°$. The dimension of the central region has been chosen considering the $-3dB$ gain angular beamwidth of the horn antenna. The focal distance F has been fixed at $F = 91.8\,mm$. This value has been chosen because *i)* it is close to the value that maximizes the total efficiency η_{tot} ($F/D = 1.45$, see Fig. 8.10 (b)), and *ii)* it allows using 16 identical cells (4×4 UCs) in the central region, providing the same reflection phase $\phi(S_{11})$ after the first reflection.

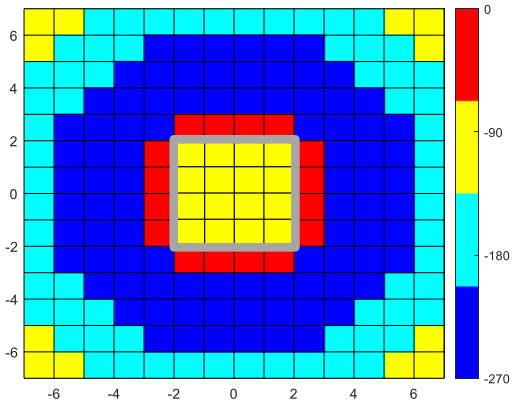

Figure 8.12 Phase compensation of internal and external regions of TA layer of DLP-FTA, considering a focal distance $F/3 = 30.6\ mm$ and focal distance $F = 91.8\ mm$, respectively at working frequency $f = 27\ GHz$.

In the folded configuration, the optimization of the distance between the top and bottom layer becomes more complex due to additional factors, such as the presence of standing waves and nonideal plane wave incidence [62]. A lot of simulations have been performed changing *i)* the focal distances F between the TA layer and the reflector layer and *ii)* the feed z-shift h_z between the horn antenna and the reflector layer in order to maximize the realized gain G, and to minimize the Side Lobe Levels (SLLs) for azimuth angle $\phi = 90°$ and $\phi = 0°$. The best result is obtained when the focal distance is $F = 72.5\ mm$ and feed z-shift is $h_z = 0\ mm$.

For a TA, the theoretical directivity D_{TH} is approximately evaluated using the equation $D_{th} = 4\pi A/\lambda^2$ [181], where A is the geometrical area of the antenna, and λ is the wavelength. For the frequencies considered in Table 8.4, the theoretical directivity D_{th} should change in the range $D_{th} = 25.5 - 26.3\ dB$. The simulation of the DLP-FTA, including the horn feeding antenna and the reflector layer, has been performed in CST Studio software.

Table 8.4 reports the directivity D, the realized gain G, the side lobe level $SLL_{\phi=90°}$ (for azimuth angle $\phi = 90°$), the side lobe level $SLL_{\phi=0°}$ (for azimuth angle $\phi = 0°$), the radiation efficiency η_{rad}, and the aperture efficiency η_{ap}, for different frequencies, when the feed z-shift h_z and focal distance F are set to $h_z = 0\ mm$ and $F = 72.45\ mm$. The aperture efficiency η_{ap} is evaluated using the equation $\eta_{ap} = \lambda^2 \cdot G/(4\pi A)$ [74, 76, 176, 181]. The radiation efficiency η_{rad} is evaluated using the equation $\eta_{rad} = G/D$ [65].

TABLE 8.4. DLP-FTA SIMULATION: RADIATIVE PARAMETERS

Frequency (GHz)	$\boldsymbol{D}$ $(\boldsymbol{dB})$	$\boldsymbol{G}$ $(\boldsymbol{dB})$	$\boldsymbol{SLL_{\phi=90°}}$ $(\boldsymbol{dB})$	$\boldsymbol{SLL_{\phi=0°}}$ $(\boldsymbol{dB})$	$\boldsymbol{\eta_{ap}}$ [%]	$\boldsymbol{\eta_{rad}}$ [%]
25.5	14.2	13.8	-7.3	-4.6	6.7	90.5
26	20.2	19.6	-16	-10.6	24.4	87
26.5	22.1	21.8	-13.6	-16.3	38.9	93.4
27	21.1	20.5	-11.3	-15.2	27.8	87.6
27.5	21.1	20.5	-13.7	-14.6	30.8	86

8.2.1 Optimization Process

The radiative parameters, i.e., the directivity D, the realized gain G, the side lobe levels SLL, the radiation efficiency η_{rad}, and the aperture efficiency η_{ap} of the DLP-FTA have been improved, by optimizing the phase of the electric field in the *xy*-plane, in order to obtain a planar wavefront. The optimization is reached by employing the suitable UC type and distribution. In the optimization, the feed z-shift $h_z = 0\ mm$ and the focal distance $F = 72.45\ mm$ are set.

Fig. 8.13 shows the electric field amplitude in the a) *xz*-plane and b) *yz*-plane, and the electric field phase in the c) *xz*-plane and d) *yz*-plane, for *y*-polarized incident wave, at the operating frequency of $f = 26.5\ GHz$. The figures show that the wavefront is not planar at the output of the TA layer.

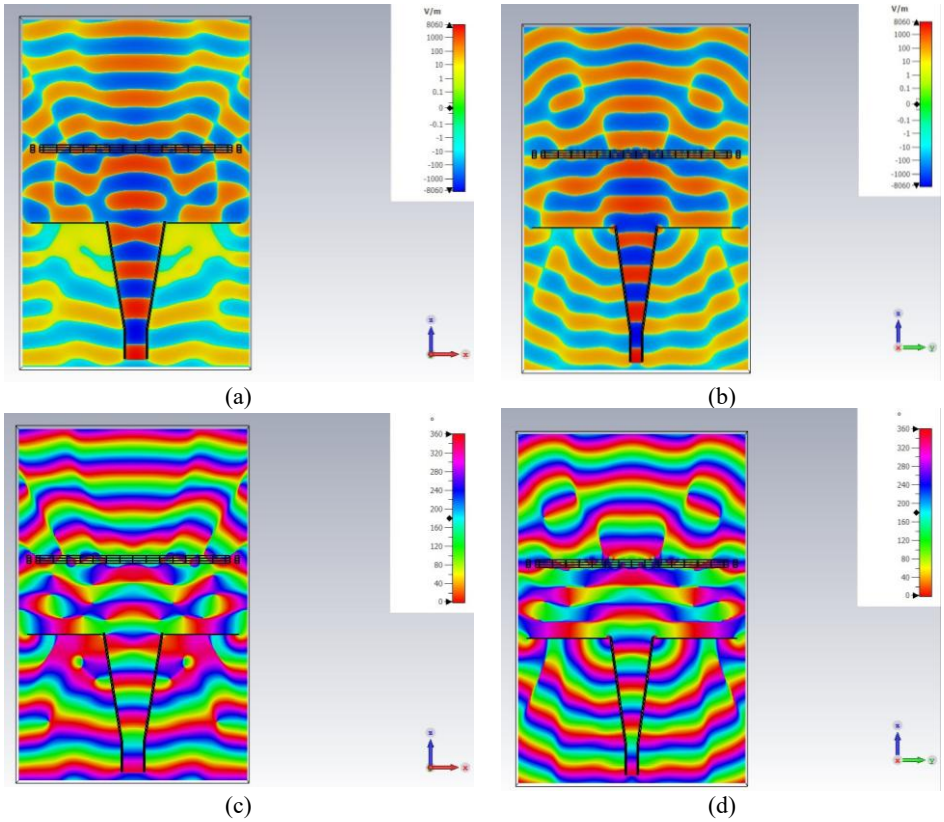

Figure 8.13 Electric field amplitude in a) *xz*-plane and b) *yz*-plane of DLP-FTA, at the working frequency of $f = 26.5\ GHz$ for y-polarized incident wave. Electric field phase in c) *xz*-plane and d) *yz*-plane of DLP-FTA, at the working frequency of $f = 26.5\ GHz$ for y-polarized incident wave.

For an *x*-polarized incident wave, the results are completely overlapping and are not presented here for the sake of shortness.

Different transverse planes (*xy*-planes of FTA-DLP) are considered at different distances from the output of TA layer and at different operative frequencies $f = 27\ GHz$, $f = 26.5\ GHz$ and $f = 26\ GHz$. Fig. 8.14 shows the *xy*-plane selected for verify the optimization degree of the phase. Taking into account the phase distribution of Fig 8.14, the UCs distribution is modified in order to obtain a uniform phase across the *xy*-plane, i.e., a constant phase of $\phi = 120°$ corresponding to the green colour.

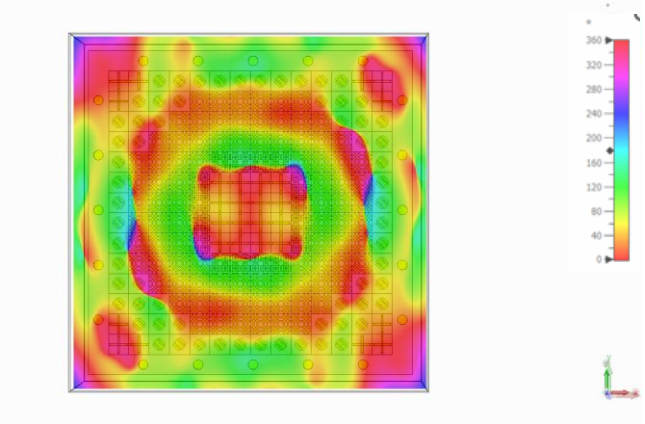

Figure 8.14 Phase distribution of electric field in *xy*-plane of FTA-DLP, at a distance of 3.5 mm from the TA layer, and at working frequency of $f = 26.5\ GHz$ for *y*-polarized incident wave.

Fig. 8.15 shows the updated phase distribution after applying a phase correction. Table 8.5 reports the optimized radiative parameters. A comparison between Table 8.4 and Table 8.5 shows a significant improvement of radiative parameters after optimization.

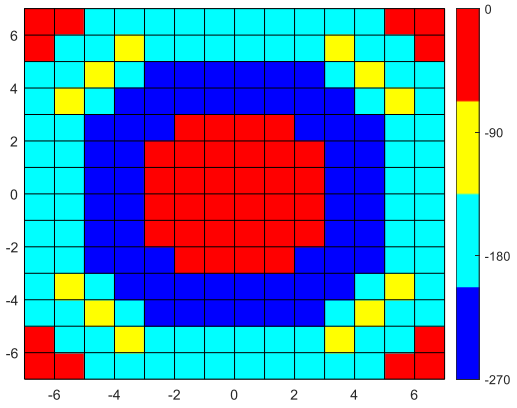

Figure 8.15 Updated phase compensation of the FTA-DLP after applying a phase correction.

TABLE 8.5 DLP-FTA SIMULATION: RADIATIVE PARAMETERS AFTER PHASE OPTIMIZATION

Frequency (GHz)	$\boldsymbol{D}$ $(\boldsymbol{dB})$	$\boldsymbol{G}$ $(\boldsymbol{dB})$	$\boldsymbol{SLL_{\phi=90^\circ}}$ $(\boldsymbol{dB})$	$\boldsymbol{SLL_{\phi=0^\circ}}$ $(\boldsymbol{dB})$	$\boldsymbol{\eta_{ap}}$ [%]	$\boldsymbol{\eta_{rad}}$ [%]
25.5	21.9	21.4	-15.1	-13.9	38.3	89.0
26	23.6	23.2	-15.6	-15.4	55.8	91.3
26.5	22.9	22.7	-19.2	-16.1	47.9	94
27	21.3	21.1	-13.9	-16.3	31.9	94
27.5	17.2	16.9	-7.8	-12.1	11.7	93.3

Fig. 8.16 shows the electric field amplitude in the a) *xz*-plane and b) *yz*-plane, and the electric field phase in the c) *xz*-plane and d) *yz*-plane at operating frequency of $f = 26.5\ GHz$, after the optimization.

The figures show that the wavefront is more planar at the output of the TA layer, when compared with Fig.8.13. Subsequently, a second optimization of the phase has been performed, but it has not yielded improvements in terms of radiative parameters and wavefront planarity with respect to the previous results.

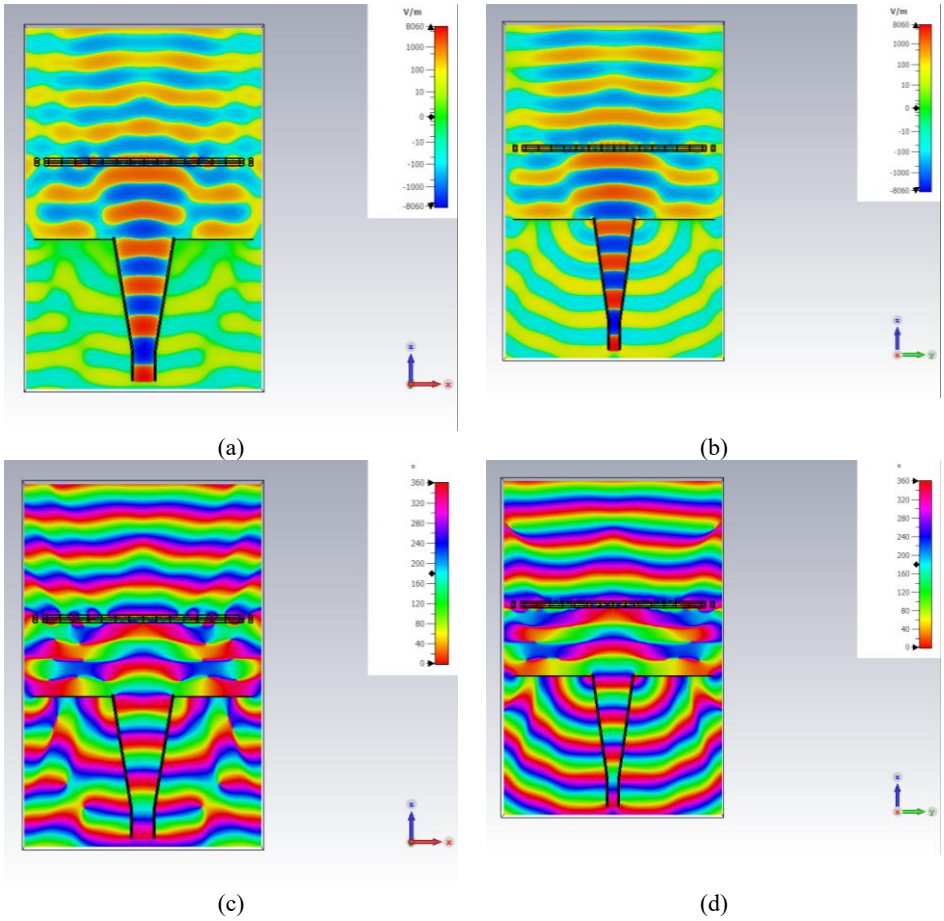

Figure 8.16 Electric field amplitude in a) *xz*-plane and b) *yz*-plane of DLP-FTA, at working frequency of $f = 26.5\ GHz$ for y-polarized incident wave. Electric field phase in c) *xz*-plane and d) *yz*-plane of DLP-FTA, at working frequency of $f = 26.5\ GHz$ for y-polarized incident wave, after the optimization.

8.3 Polarization Analysis

In this section, comparisons are reported to evaluate the DLP-FTA antenna response when illuminated by the horn antenna with polarization along the *x*-axis and *y*-axis.

Fig. 8.17 shows the input reflection coefficient $|S_{11}|$ as a function of frequency f for an *x*-polarized incident wave (black curve) and a *y*-polarized incident wave (red curve). An excellent overlap between the two curves can be observed. The impedance bandwidth, calculated at $-10\ dB$, covers the range $BW = 25.35 - 29\ GHz$.

Fig. 8.18 shows the realized gain G as a function of frequency f for *x*-polarized incident wave (black marks) and *y*-polarized incident wave (red marks). The $-3dB$ gain bandwidth is about $BW_G = 25.3 - 27.2\ GHz$.

Fig. 8.19 shows the simulated realized gain G as a function of elevation angle θ for an *x*-polarized incident wave (black curve) and *y*-polarized incident wave (red curve), for azimuth angle a) $\phi = 0°$, and b) $\phi = 90°$ at operating frequency $f = 26\ GHz$.

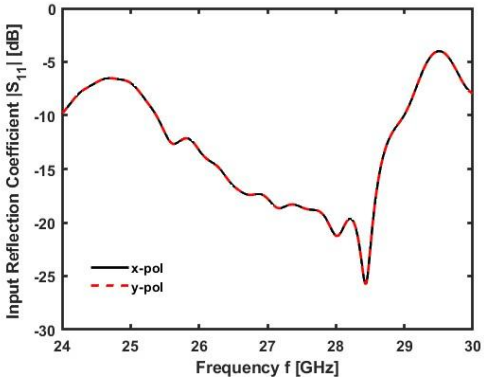

Figure 8.17 Simulated input reflection coefficient $|S_{11}|$ as a function of frequency f for x-polarized (black curve) and y-polarized (red curve) incident waves.

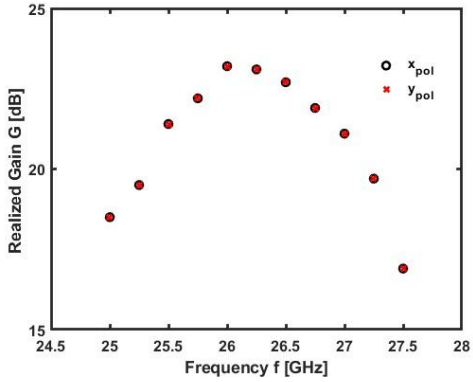

Figure 8.18 Simulated realized gain G as a function of frequency f for x-polarized (black marks) and y-polarized (red marks) incident waves.

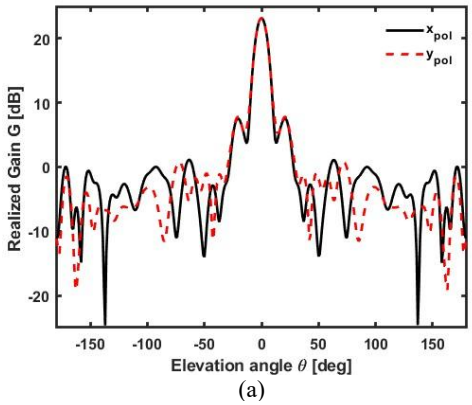

(a)

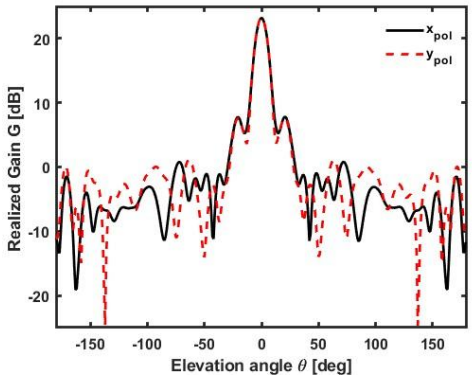

(b)

Figure 8.19 Simulated realized gain G as a function of elevation angle θ for *x*-polarized (black curve) and y-polarized (red curve) incident waves, for azimuth angle a) $\phi = 0°$ and b) $\phi = 90°$ at operative frequency $f = 26\ GHz$.

8.4 Comparison with State of the Art

Table 8.6 reports a comparison between the proposed DLP-FTA and other DLP antennas in RA, TA, and FTA configurations. The proposed DLP-FTA compared with the DLP-FTA antenna [62] shows a comparable gain bandwidth BW_G and a higher aperture efficiency η_{ap} and higher impedance bandwidth BW. Furthermore, it shows a higher aperture efficiency with respect to the TA [74, 77, 79, 173, 176] and RA [75]. Moreover, the proposed DLP-FTA achieves comparable aperture efficiency η_{ap} and gain bandwidth BW_G with respect to the TAs [76, 78], but with a significantly reduced profile due to the folded architecture.

TABLE 8.6 COMPARISON BETWEEN THE PROPOSED DLP-FTA AND LITERATURE

Refer.	**Antenna type**	**UCs No.**	f_0 $[GHz]$	$\frac{F}{D}$	**Peak Gain** G $[dB]$	**Gain B.W.*** BW_G [%]	**Imp. B.W.** BW[%]	**Ap. Eff.** η[%]
[62]	FTA	16×16	10	0.55	22	~9*	~5	~25
[74]	TA	381	28	0.4	21.4	#	#	36.8
[75]	RA	30×30	15.5	0.86	.24.5	15**	#	37.4
[76]	TA	22×22	31	1.27	28.7	10.3**	#	61.3
[77]	TA	21×21	30	1.5	21	9.6**	#	40
[78]	TA	20×20	14.25	1.4	29.2	6.8**	#	60.3
[79]	TA	351	15	0.75	23.1	37.3**	#	42.3
[173]	TA	22×22	12	0.6	21	10.8**	#	17
[176]	TA	#	27.5	0.5	24.2	12.4**	10.5	24.5
This work	FTA	14×14	26	1.15	23.2	7.3**	14***	55.8

* The gain bandwidth BW_G is defined at $-3dB$ for [62, 176] and the proposed DLP-FTA:
**The gain bandwidth BW_G is defined at $-1dB$ for [75-79, 173]
***The $-10\ dB$ relative impedance bandwidth BW is calculated with respect to the frequency corresponding to the maximum realized gain, i.e. $f = 26\ GHz$.

8.5 Conclusion

This chapter illustrates the design and optimization of a DLP-FTA operating in the *Ka*-band. The FTA consists of 14 × 14 symmetrical UCs, designed to provide a transmission coefficient of about $-3dB$ and 2π full phase coverage for both linear polarized incident waves. The proposed DLP-FTA exhibits a realized gain G of $G = 21.1\ dB$ and an aperture efficiency of $\eta = 31.5\%$ at the frequency $f = 27\ GHz$, reaching a maximum realized gain of $G = 23.2\ dB$ and an aperture efficiency of $\eta = 58.8\ \%$ at the frequency $f = 26\ GHz$. Moreover, the device demonstrates a relative impedance bandwidth of $BW = 14\%$, and $-3dB$ gain bandwidth of $BW_G = 7.3\%$ making this device competitive with the state of the art. The next step will involve the complete fabrication and experimental characterization of the proposed DLP-FTA. At the moment the fabrication has been partially performed.

Conclusions

In this Ph.D. thesis, novel microwave and optical devices for telecommunications and IoT applications have been designed, optimized, and characterized.
Regarding the optical devices, the main results concern the design and optimization of a Mid-IR *i)* fiber laser and *ii)* optical fiber amplifier based on praseodymium-doped fluoroindate glass (Pr^{3+}: InF_3) operating at $\lambda = 4\ \mu m$; and *iii)* the design, fabrication and characterization of a non-adiabatic tapered optical fiber sensor based on ZBLAN glass. In particular:

i) The fiber laser has been designed, and the simulations predict a slope efficiency of $\eta = 17.2\%$ and a pump power threshold of $P_{th} = 75\ mW$. Compared to the state of the art of fluoroindate fiber lasers, the proposed laser demonstrates competitive performance achieving longer emission wavelengths λ through single wavelength pumping at $\lambda_p = 1.55\ \mu m$;

ii) The optical fiber amplifier provides high-performance amplification, achieving a high gain $G = 32.1\ dB$, a low noise figure $NF = 6\ dB$, and a wide bandwidth $BW_G = 130\ nm$ around the central wavelength $\lambda = 4\ \mu m$, with an input signal power $P_s = -30 dBm$ and a pump wavelength $\lambda_p = 1.55\ \mu m$.

iii) The non-adiabatic tapered optical fiber sensor based on ZBLAN glass has been designed, fabricated, and characterized for temperature sensing in the Mid-IR range; the sensor exploits the thermo-optic dn/dT and thermal expansion α properties of fluoride glass and the interference pattern shift, achieving a simulated and a measured sensitivity of $S_T = -85.3\ pm/K$, demonstrating a competitive and low-cost sensor compared to the state of the art;

Regarding microwave devices, the main results concern the design, fabrication and characterization of the following structures: *iv)* an AVA with and without MTMs, *v)* an FPA, *vi)* a DLP-TA; and the design and optimization of *vii)* a DLP-FTA. In particular:

iv) The AVA without MTMs is compared with the AVA integrated with three MTM configurations based on SRRs. The simulations and the measurements have demonstrated that the integration of MTMs has allowed maximizing the measured peak gain $G_{max} = 12\ dB$ at the frequency $f = 8.6\ GHz$, with a maximum gain enhancement of $\Delta G = 2.5\ dB$ compared to the AVA without the MTMs, while maintaining a wide operating bandwidth of $f = 3 - 13\ GHz$.

v) The FPA has been realized using an unconventional hybrid fabrication technique combining conductive inkjet and 3D printing; this cost-effective prototype demonstrated excellent performance with a maximum measured

gain $G_{max} = 13.2\ dB$ at the frequency $f = 8.2\ GHz$, an impedance bandwidth $BW = 31.3\%$, and a $-3\ dB$ gain bandwidth $BW_G = 24.5\ \%$, proving the possibility of low-cost antenna manufacturing;

vi) The DLP-TA for beam-steering applications in the *Ku*-band has been realized showing a measured peak gain $G_{m0} = 21\ dB$, and an aperture efficiency $\eta_{ap,0} = 17\ \%$ at the frequency $f_0 = 12\ GHz$, while the best beam steering performance is obtained at frequency $f_1 = 12.4\ GHz$ with a beam steering up to $\gamma_{max} = \pm 30°$, and a scan loss of $\Delta G_1 = 2.73\ dB$

vii) The compact DLP-FTA operating in the *Ka*-band range has been designed and optimized; thanks to the ad-hoc design of the unit cells, the antenna operates with both linear polarizations, achieving a simulated realized gain $G = 21.1 dB$ and a high aperture efficiency $\eta_{ap} = 31.5\ \%$ at frequency $f = 27 GHz$, reaching a maximum realized gain $G_{max} = 23.2\ dB$ and an aperture efficiency $\eta_{ap,max} = 58.8\ \%$ at frequency $f = 26\ GHz$. The device demonstrates a relative impedance bandwidth of $BW = 14\%$, and a $-3dB$ gain bandwidth of $BW_G = 7.3\%$ making this device in line with the state of the art. The next step will be the fabrication and characterization.

Part of these research activities have been published in International Journals and presented at National and International Conferences, as detailed in the next paragraph.

These research activities pave the way for multiple future developments. Regarding the optical devices, future work will primarily focus on the experimental fabrication and characterization of the simulated Mid-IR fiber laser and optical amplifier to practically validate their high-performance theoretical models. Additionally, the proposed non-adiabatic tapered optical fiber sensor could be integrated into larger IoT networks for real-time, distributed environmental monitoring. Concerning the microwave devices, the immediate next step will be the simulation of the beam-steering performance, followed by the manufacturing and experimental testing of the Ka-band DLP-FTA. Furthermore, the low-cost and unconventional fabrication techniques investigated in this work, such as the combination of 3D printing and conductive inkjet printing, can be further optimized for large-scale manufacturing and improved resolution. Finally, the design methodologies applied to the proposed antennas and transmitarrays could be scaled to higher millimeter-wave and sub-THz frequency bands, integrating active electronic elements for dynamic, continuous beam-steering in order to satisfy the requirements of future communication systems.

List of Publications

International Journals:

[j1] A. M. Loconsole, V. Portosi, V.V. Francione, F. Anelli, A. Annunziato, M.C. Falconi, and F. Prudenzano "Optimization of a wideband antipodal Vivaldi antenna with metalenses," *Int. J. Microw. Wirel. Technol.*, vol. 16, no. 1, pp. 41–48, Feb. 2024.

[j2] A. M. Loconsole, V. V. Francione, A. Annunziato, F. Anelli, and F. Prudenzano, "Design of a High-Performance Mid-IR Fiber Laser Based on Pr3+-Doped Fluoroindate Glass," *J. Light. Technol.*, vol. 42, no. 7, pp. 2488–2493, Apr. 2024.

[j3] F. Anelli, A. Annunziato, A. M. Loconsole, V.V. Francione, S. Cozic, S. Poulain, and F. Prudenzano, "Mid-infrared interferometry with non-adiabatic tapered ZBLAN optical fiber," *Opt. Express*, vol. 32, no. 11, pp. 18944-18957, May 2024.

[j4] Md. I. Khan, A. M. Loconsole, F. Anelli, V. V. Francione, A. U. Khan, M. Simone, G. Sorbello, and F. Prudenzano, "A Low-Profile Dual-Polarized Transmitarray with Enhanced Gain and Beam Steering at Ku Band," *Appl. Sci.,* vol. 15, no. 9, p. 4656, Apr. 2025.

[j5] A. M. Loconsole, V. V. Francione, F. Anelli, S. Taccheo, and F. Prudenzano, "Mid-IR Amplification Based on a Pr3+: InF3 Optical Fiber in the Range 3.8−4.2 μm," *J. Light. Technol.,* vol. 43, no. 11, pp. 5451-5458, Jun. 2025

[j6] F. Anelli, A. M. Loconsole, V. V. Francione, Md. I. Khan, and F. Prudenzano, "Cost-effective Fabry-Pérot Antenna via Conductive Inkjet and Additive Printing," *IEEE Antennas Wirel. Propag. Lett.,* vol. 24, no. 8, pp. 2182-2186, Aug. 2025.

Proceedings of SPIE:

[sp1] A. M. Loconsole, V.V. Francione, A. Annunziato, F. Anelli, Md. I. Khan, S. Taccheo, and F. Prudenzano, "Design of a mid-IR optical fiber amplifier based on a Pr3+: InF3 glass," in *Proc. of SPIE Fiber Lasers and Glass Photonics: Materials through Applications IV*, Strasbourg, France, vol. 13003, Jun. 2024, p. 27.

[sp2] F. Anelli, A. Annunziato, A. M. Loconsole, V.V. Francione, S. Cozic, S. Poulain, and F. Prudenzano "A temperature sensor based on all-fiber Mach-Zehnder interferometer with indium fluoride glass," in *Proc. of SPIE Fiber Lasers and Glass Photonics: Materials through Applications IV*, Strasbourg, France, vol. 13003, Jun. 2024, p. 39.

[sp3] A. Annunziato, F. Anelli, A. M. Loconsole, V.V. Francione, S. Cozic, S. Venck, S. Poulain, and F. Prudenzano, "Single-mode fluoroindate coupler for mid-IR applications," in *Proc. of SPIE Fiber Lasers and Glass Photonics: Materials through Applications IV*, Strasbourg, France, vol. 13003, Jun. 2024, p. 29.

[sp4] A. Annunziato, A. M. Loconsole, V.V. Francione, F. Anelli, L. Ressa, F. Pisani, G. Galzerano, and F. Prudenzano, "Design of in-band pumped dysprosium-doped ZBLAN fiber amplifier for mid-IR wavelength range," in *Proc. of SPIE Fiber Lasers and Glass Photonics: Materials through Applications IV*, Strasbourg, France, vol. 13003, Jun. 2024, p. 14.

Proceedings of International Conferences:

[c1] F. Anelli, A. Annunziato, A.M. Loconsole, V. Portosi, V.V. Francione, M.C. Falconi, P. Le Pays Du Teilleul, S. Cozic, S. Poulain, and F. Prudenzano, "Fabrication of Tapered Devices with Fluoride and Chalcogenide Optical Fibers for Mid-IR Applications," in *IEEE Proceedings of 23rd International Conference on Transparent Optical Networks (ICTON 2023)*, Bucharest, Romania, Jul. 2023, pp. 1–4.

[c2] A. Annunziato, F. Anelli, A.M. Loconsole, M.C. Falconi, V. Portosi, V.V. Francione, and F. Prudenzano, "Optical Combining in Medium Infrared Wavelength Range and Its Applications," in *IEEE Proceedings of 23rd International Conference on Transparent Optical Networks (ICTON 2023)*, Bucharest, Romania, Jul. 2023, pp. 1–4, invited paper.

[c3] A. M. Loconsole, A. Annunziato, F. Anelli, V.V. Francione, V. Portosi, M.C. Falconi, and F. Prudenzano, "Design of a Pr3+: InF3 Fiber Laser Pumped in near-IR and Emitting at 4-micron Wavelength," in *IEEE Proceedings of 23rd International Conference on Transparent Optical Networks (ICTON 2023)*, Bucharest, Romania, Jul. 2023, pp. 1–4.

[c4] F. Anelli, A. M. Loconsole, V. Portosi, A. Annunziato, V. V. Francione, and F. Prudenzano, "A Wideband Flexible Fabry-Perot Resonator Antenna: Inkjet-printing on Ultrathin PET Layers," in *Proceedings of 2023 IEEE Conference on Antenna Measurements and Applications (CAMA 2023)*, Genoa, Italy, Nov. 2023, pp. 972–976.

[c5] F. Anelli, A. M. Loconsole, A. Annunziato, V. V. Francione, and F. Prudenzano, "Design and Characterization of a Flexible Fabry-Perot Antenna Fabricated using Conductive Inkjet Printing," in *IEEE Proceedings of 18th European Conference on Antennas and Propagation (EuCAP 2024)*, Glasgow, United Kingdom, Mar. 2024, pp. 1–5.

[c6] A. M. Loconsole, A. Mahmoud, F. Anelli, V. V. Francione, M. Ettorre, and F. Prudenzano, "Feasibility Investigation on a Low-Cost Air-Filled Substrate Integrated Waveguide Array Antenna in V-Band," in *IEEE Proceedings of 18th European Conference on Antennas and Propagation (EuCAP 2024)*, Glasgow, United Kingdom, Mar. 2024, pp. 1–5.

[c7] A. M. Loconsole, V.V. Francione, A. Annunziato, F. Anelli, Md. I. Khan, S. Taccheo, and F. Prudenzano, "Design of a praseodymium-doped fluoroindate fiber amplifier for medium infrared wavelength range applications," in *IEEE Proceedings of 24th International Conference on Transparent Optical Networks (ICTON 2024),* Bari, Italy, Jul. 2024, pp. 1–4.

[c8] F. Anelli, A. Annunziato, A.M. Loconsole, V.V. Francione, Md. I. Khan, S. Cozic, S. Poulain, and F. Prudenzano, "Enhancing Sensing Capabilities: Fabrication of Tapered Optical Fiber Sensors in Fluoride Glasses," in *IEEE Proceedings of 24th International Conference on Transparent Optical Networks (ICTON 2024),* Bari, Italy, Jul. 2024, pp. 1–4.

[c9] F. Anelli, A. Annunziato, A.M. Loconsole, V.V. Francione, Md. I. Khan, S. Cozic, S. Poulain, and F. Prudenzano "Indium Fluoride Optical Fiber End-Pump Combiner for High-Power All-Fiber Sources," in *IEEE Proceedings of 24th International Conference on Transparent Optical Networks (ICTON 2024),* Bari, Italy, Jul. 2024, pp. 1–4.

[c10] Md. I. Khan, F. Anelli, A. M. Loconsole, V. V. Francione, and F. Prudenzano, "Ultra-Thin Metasurface for High Gain and Beam Steering at 5G Millimeter Wave Applications," in *IEEE Proceedings of 24th International Conference on Transparent Optical Networks (ICTON 2024),* Bari, Italy, Jul. 2024, pp. 1–4.

[c11] A. M. Loconsole, F. Anelli, V. V. Francione, and F. Prudenzano, "Active Devices Based on Rare-Earth-doped Fluoroindate Fibers in Mid-Infrared Range," in *IEEE Proceedings of 25th International Conference on Transparent Optical Networks (ICTON 2025)*, Barcelona, Spain, Jul. 2025, pp. 1–4.

[c12] Md. I. Khan, A. M. Loconsole, F. Anelli, V. V. Francione, and F. Prudenzano "A Wideband Magneto-Electric Dipole Based Slant Polarized Antenna with Metasurface," in *Proceedings of 2025 IEEE Conference on Antenna Measurements and Applications (CAMA 2025),* Antibes, France, Nov. 2025.

[c13] Md. I. Khan, F. Anelli, A. M. Loconsole, V. V. Francione, and F. Prudenzano "A Wideband Magneto-Electric Dipole Antenna with Electromagnetic Bandgap Structure," in *Proceedings of 2025 IEEE Conference on Antenna Measurements and Applications (CAMA 2025),* Antibes, France, Nov. 2025.

International Conferences:

[i1] F. Anelli, V. Portosi, A. M. Loconsole, V. V. Francione, A. Annunziato, and F. Prudenzano, "A Wideband Inkjet-Printed Antenna on Flexible Pet Substrate," in *3rd International Conference on Dielectric Photonic Devices and System Beyond Visible, D-Photon 2023,* Bari, Italy, 11-13 Jul. 2023.

[i2] A. Annunziato, F. Anelli, V. V. Francione, V. Portosi, A. M. Loconsole, C. Holmes, M. Godfrey, J. Dulieu-Barton, and F. Prudenzano, "Flexible Photonic Sensor for Bending Monitoring," in *3rd International Conference on Dielectric Photonic Devices and System Beyond Visible, D-Photon 2023*, Bari, Italy, 11-13 Jul. 2023.

[i3] A. Annunziato, F. Anelli, V. V. Francione, A. M. Loconsole, V. Portosi, and F. Prudenzano, "Mid-IR Optical Combiners for All-In-Fiber Laser," in *3rd International Conference on Dielectric Photonic Devices and System Beyond Visible, D-Photon 2023*, Bari, Italy, 11-13 Jul. 2023.

[i4] A. M. Loconsole, A. Annunziato, M. C. Falconi, F. Anelli, V. V. Francione, V. Portosi, and F. Prudenzano, "Investigation on a Mid-IR Laser Based on a Praseodymium-Doped Fluoroindate Fiber," in *3rd International Conference on Dielectric Photonic Devices and System Beyond Visible, D-Photon 2023*, Bari, Italy, 11-13 Jul. 2023.

[i5] F. P. Pallotta, V. Portosi, A. M. Loconsole, V.V. Francione, F. Anelli, A. Annunziato, A. Crudele, and F. Prudenzano, "A Metalens for Non-Invasive Microwave Hyperthermia in Cancer Treatment," in *3rd International Conference on Dielectric Photonic Devices and System Beyond Visible, D-Photon 2023*, Bari, Italy, 11-13 Jul. 2023.

[i6] F. Anelli, A. Annunziato, A. M. Loconsole, M. C. Falconi, V. Portosi, V. V. Francione, and F. Prudenzano, "Fabrication of Mid-IR Tapered Devices Using Fluoride and Chalcogenide Optical Fibers," in *Conference on Photonics for Advanced Spectroscopy and Sensing (C-PASS)*, Castellaneta Marina, Italy, 3-8 Sep. 2023.

[i7] A. Annunziato, F. Anelli, V. Portosi, V. V. Francione, A. M. Loconsole, M. C. Falconi, and F. Prudenzano, "Indium Fluoride Multimode Optical Fibers Couplers," in *Conference on Photonics for Advanced Spectroscopy and Sensing (C-PASS)*, Castellaneta Marina, Italy, 3-8 Sep. 2023.

[i8] A. M. Loconsole, M. C. Falconi, A. Annunziato, F. Anelli, V. Portosi, V. V. Francione, and F. Prudenzano, "Investigation on a 4-μm emitting laser based on a fluoroindate fiber doped with praseodymium," in *Conference on Photonics for Advanced Spectroscopy and Sensing (C- PASS)*, Castellaneta Marina, Italy, 3-8 Sep. 2023.

[i9] F. Anelli, A. M. Loconsole, V. V. Francione, A. Annunziato, Md. I. Khan, and F. Prudenzano, "Recent advances on fiber devices for Mid-IR wavelength range", in *Photoluminescence in Rare Earths: Photonic Materials Workshop (PRE'24-Poland)*, Trento, Italy, 13-15 May 2024, invited paper.

[i10] F. Anelli, A. M. Loconsole, V. V. Francione, Md. I. Khan, and F. Prudenzano "Inkjet-Printed Antennas: From Simple Structures to Complex Resonators," in *20th International Conference on Microwave and High Frequency Applications (AMPERE 2025),* Bari, Italy, 15-19 Sep. 2025.

[i11] A. M. Loconsole, F. Anelli, V. V. Francione, Md. I. Khan, and F. Prudenzano "Microwave Needle Applicators for Cancer Therapy: A Low-Cost and Mini-Invasive Solution," in *20th International Conference on Microwave and High Frequency* Applications (AMPERE 2025), Bari, Italy, 15-19 Sep. 2025.

National Conferences:

[n1] F. Anelli, A. Annunziato, A. M. Loconsole, V. V. Francione, Md. I. Khan, and F. Prudenzano, "Towards Optical Fiber Sensing with Fluoride Glasses", in *Italian Conference on Optics and Photonics (ICOP),* Florence, Italy, 17-19 Jun. 2024.

[n2] F. Anelli, V. V. Francione, Md. I. Khan, and A. M. Loconsole, "Fabrication and Characterization of Micro-Tapered Long Period Gratings on Zirconium Fluoride Optical Fiber for Mid-Infrared Applications", in *XXV Riunione Nazionale di Elettromagnetismo (RiNEm)*, Viareggio, Italy, Sep. 30 – 2 Oct. 2024.

[n3] A. M. Loconsole, V. V. Francione, F. Anelli, Md. I. Khan, A. Mahmoud, M. Ettorre, and F. Prudenzano, "Design and Fabrication of an Air-Filled Substrate Integrated Waveguide Antenna Array", in *XXV Riunione Nazionale di Elettromagnetismo (RiNEm)*, Viareggio, Italy, Sep. 30 – 2 Oct. 2024.

References

[1] M. Joharifar, H. Dely, et al., "Exploring Mid-IR FSO Communications with Unipolar Quantum Optoelectronics," J. Light. Technol., vol. 43, no. 4, pp. 1633-1643, Feb. 2025.

[2] N. S. Prasad, “Optical Communications in the mid-wave IR spectral band,” in Free-Space Laser Communications, New York, NY: Springer New York, 2005, pp. 347–391.

[3] M. Seminara, T. Gabbrielli, et al., “Characterization of noise regimes in mid-IR free-space optical communication based on quantum cascade lasers,” Opt. Express, vol. 30, no. 25, pp. 44640-44656, Dec. 2022.

[4] A. Fuerbach, G. Bharathan, and M. Ams, “Grating Inscription into Fluoride Fibers: A Review,” IEEE Photonics J., vol. 11, no. 5, pp. 1-11, Oct. 2019.

[5] B. M. Walsh, H. R. Lee, and N. P. Barnes, “Mid infrared lasers for remote sensing applications,” J. Lumin., vol. 169, part B, pp. 400-405, Jan. 2016.

[6] Y. Wang, Y. Feng, A. I. Adamu, et al., “Mid-infrared photoacoustic gas monitoring driven by a gas-filled hollow-core fiber laser,” Sci. Rep., vol. 11, no. 1, art. no. 3512, Feb. 2021.

[7] F. Anelli, A. Annunziato, A. M. Loconsole, V. V. Francione, et al., “Mid-infrared interferometry with non-adiabatic tapered ZBLAN optical fiber,” Opt. Express, vol. 32, no. 11, pp. 18944-18957, May 2024.

[8] K. Goya, Y. Koyama, et al., "A fluoride fiber optics in-line sensor for mid-IR spectroscopy based on a side-polished structure," Sens. Actuators B Chem., vol. 351, art. no. 130904, Jan. 2022.

[9] Q. Hao, G. Zhu, et al., "Mid-infrared transmitter and receiver modules for free-space optical communication," Appl. Opt., vol. 56, no. 8, pp. 2260-2264, 2017.

[10] L. Sójka, L. Pajewski, S. Lamrini, et al., "High Peak Power Q-switched Er:ZBLAN Fiber Laser," J. Light. Technol., vol. 39, no. 20, pp. 6572-6578, Jul. 2021.

[11] L. Zhang, F. Guan, L. Zhang, and Y. Jiang, "Next generation mid-infrared fiber: fluoroindate glass fiber," Opt. Mater. Express, vol. 12, no. 4, pp. 1683-1707, 2022.

[12] O. Henderson-Sapir, A. Malouf, et al., "Recent Advances in 3.5 μm Erbium-Doped Mid-Infrared Fiber Lasers," IEEE J. Sel. Top. Quantum Electron., vol. 23, no. 3, pp. 6-14, May 2017.

[13] V. Fortin, F. Maes, M. Bernier, S. Toubou Bah, M. D'Auteuil, and R. Vallée, "Watt-level erbium-doped all-fiber laser at 3.44 μm," Opt. Lett., vol. 41, pp. 559-562, 2016.

[14] M. C. Falconi, A. M. Loconsole, A. Annunziato, S. Cozic, S. Poulain, and F. Prudenzano, "Design of a Broadband Erbium-doped Fluoroindate Fiber Laser Emitting up to 3.91 μm," J. Light. Technol., vol. 41, no. 18, pp. 6065-6072, Sep. 2023.

[15] F. Maes, V. Fortin, S. Poulain, M. Poulain, J.-Y. Carrée, M. Bernier, and R. Vallée, "Room-temperature fiber laser at 3.92 μm", Optica, vol. 5, no. 7, pp. 761-764, Jul. 2018.

[16] A. M. Loconsole, M. C. Falconi, V. Portosi, and F. Prudenzano, “Numerical Design of a Gain-Switched Pulsed Laser at 3.92 μm Wavelength Based on a Ho3+-Doped Fluoroindate Fiber,” J. Light. Technol., vol. 39, no. 10, pp. 3276-3283, May 2021.

[17] F. Zhou, J. Li, H. Luo, F. Quellette, and Y. Liu, “Numerical Analysis of 3.92 μm Dual-Wavelength Pumped Heavily-Holmium-Doped Fluoroindate Fiber Lasers,” J. Light. Technol., vol. 39, no. 2, pp. 633-645, Jan. 2021.

[18] Z. Cheng et al., "Numerical Modeling of Dual-wavelength Pumped Heavily-Ho3+-Doped Fluoroindate Fiber Lasers with Efficient Output at 3.92 μm," J. Light. Technol., vol. 41, no. 22, pp. 7021-7028, Nov. 2023.

[19] A. M. Loconsole, M. C. Falconi, A. Annunziato, S. Cozic, S. Poulain and F. Prudenzano, "Design of a Mid-IR Laser Based on a Ho:Nd-codoped Fluoroindate Fiber," J. Light. Technol., vol. 41, no. 2, pp. 702-708, Jan. 2023.

[20] Z. Zhang, R. Wang, M. Liu, S. Wang, et al., "Enhanced 3.9 μm emission from diode pumped Ho3+/Eu3+ codoped fluoroindate glasses," Opt. Lett., vol. 46, pp. 2031-2034, 2021.

[21] M. R. Majewski, R. I. Woodward, J.-Y. Carreé, S. Poulain, M. Poulain, and S. D. Jackson, "Emission beyond 4 μm and mid-infrared lasing in a dysprosium-doped indium fluoride (InF3) fiber," Opt. Lett., vol. 43, no. 8, pp. 1926-1929, 2018.

[22] M. R. Majewski, and S. D. Jackson, “Numerical Design of 4 μm-Class Dysprosium Fluoride Fiber Lasers,” J. Light. Technol., vol. 39, no. 15, pp. 5103-5110, May 2021.

[23] R. S. Quimby, and M. Saad, “Dy:fluoroindate fiber laser at 4.5 μm with cascade lasing,” in Proc. Adv. Solid-State Lasers Congr., 2013, art. no. AM2A.7.

[24] A. M. Loconsole, V. V. Francione, F. Anelli, et al., "Design of a High-Performance Mid-IR Fiber Laser Based on Pr3+-Doped Fluoroindate Glass," J. Light. Technol., vol. 42, no. 7, pp. 2488-2493, Apr. 2024.

[25] J. Pisarska, "IR transmission and emission spectra of erbium ions in fluoroindate glass," J. Non-Cryst. Solids, vol. 345-346, pp. 382-385, Oct. 2004.

[26] V. A. Jerez, C. B. de Araujo, and Y. Messaddeq, "Dynamics of energy transfer and frequency upconversion in Tm3+ doped fluoroindate glass," J. Appl. Phys., vol. 96, no. 5, pp. 2530-2534, Sep. 2004.

[27] L. J. Borrero-Gonzalez, G. Galleani, et al., "Visible to infrared energy conversion in Pr3+-Yb3+ co-doped fluoroindate glasses", Opt. Mater., vol. 35, no. 12, pp. 2085-2089, Oct. 2013.

[28] M. Kochanowicz, J. Zmojda, et al., "Near-IR and mid-IR luminescence end energy transfer in fluoroindate glasses co-doped with Er3+/ Tm3+," Opt. Mater. Express, vol. 9, no. 12, Dec. 2019.

[29] M. Kochanowicz, J. Zmojda, et al., "Sensitization of Ho3+-doped fluoroindate glasses for near and mid-infrared emission," Opt. Mater., vol. 101, Mar. 2020.

[30] G. Bolognesi, D. Parisi, D. Calonico, et al., "Yellow laser performance of Dy3 in co-doped Dy,Tb:LiLuF4," Opt. Lett., vol. 39, no. 23, pp. 6628-6631.

[31] H. He, Z. Jia, Y. Ohishi, W. Qin, G. Qin, "Efficient 4 μm emission from Pr3+/Yb3+ co-doped fluoroindate glass", Opt. Lett., vol. 46, no. 22, pp. 5607-5610, 2021.

[32] X. Zhu, R. K. Jain, "High Output Power (2.45 Watts) Mid-IR Fiber Amplifier," in OFC 2006, Anaheim, CA, USA, 2006.

[33] Y. Wang, H. Luo, H. Gong, et al., "2.3 W, Linearly-Polarized Superfluorescent Generation From a Polarization-Maintaining Er3+-Doped Fluoride Fiber Amplifier Around 2.8 μm," J. Light. Technol., vol. 40, no. 17, pp. 6001-6005, Sept. 2022.

[34] N. B. Chichkov, P. Ray, S. Cozic, et al., "Amplification of Nanosecond Pulses in a Single-Mode Erbium-Doped Fluoride Fibre Amplifier," IEEE Photon. Technol. Lett., vol. 35, no. 1, pp. 3-6, Jan. 2023.

[35] E. A. Anashkina, and A. V. Kim, "Numerical Simulation of Ultrashort Mid-IR Pulse Amplification in Praseodymium-Doped Chalcogenide Fibers," J. Light. Technol., vol. 35, no. 24, pp. 5397-5403, Dec. 2017.

[36] E. A. Anashkina, "Design and Numerical Modeling of Broadband Mid-IR Rare-Earth-Doped Chalcogenide Fiber Amplifiers," IEEE Photon. Technol. Lett., vol. 30, no. 13, pp. 1190-1193, July 2018.

[37] M. C. Falconi, G. Palma, F. Starecki, V. Nazabal, J. Troles, J. Adam, S. Taccheo, M. Ferrari, F. Prudenzano, "Dysprosium-Doped Chalcogenide Master Oscillator Power Amplifier (MOPA) for Mid-IR Emission," J. Light. Technol., vol. 35, no. 2, pp. 265-273, Jan. 2017.

[38] G. Palma, P. Bia, L. Mescia, T. Yano, et al., "Design of fiber coupled Er3+ chalcogenide microsphere amplifier via particle swarm optimization algorithm," Opt. Eng., vol. 53, no. 7, p. 071805, Jul. 2014.

[39] Y. Liu, H. Lin, et al., "Integrated near-infrared QEPAS sensor based on a 28 kHz quartz tuning fork for online monitoring of CO2 in the greenhouse," Photoacoustics, vol. 25, no. 2, p. 100332, Mar. 2022.

[40] Y. Wang, X. Huang and M. Wang, "Temperature Insensitive Birefringent LPG Twist Sensing Based on the Polarization Properties," IEEE Photon. Technol. Lett., vol. 27, no. 22, pp. 2367-2370, Aug. 2015.

[41] F. Anelli, A. Annunziato, M. Godfrey, A. M. Loconsole, C. Holmes and F. Prudenzano, "Effects of Curvature on Flexible Bragg Grating in Off-Axis Core: Theory and Experiment," J. Light. Technol., vol. 41, no. 9, pp. 2904-2910, May 2023.

[42] D. Tosi, E. G. Macchi, M. Gallati, G. Braschi, A. Cigada, S. Rossi, G. Leen and E. Lewis, "Fiber-optic chirped FBG for distributed thermal monitoring of ex-vivo radiofrequency ablation of liver," Biomed. Opt. Express, vol. 5, no. 6, pp. 1799-1811, May 2014.

[43] C. Zhou, H. Zhang, et al., "D-Shaped Photonic Crystal Fiber Plasmon Sensors Based on Self-Reference Channel," IEEE Photon. Technol. Lett., vol. 32, no. 10, pp. 589-591, Apr. 2020.

[44] Y. Ge and D. N. Wang, "Optical Fiber Interferometer Based on Inner Air-Cavity with an Open Channel for Gas Pressure Sensing," IEEE Photon. Technol. Lett., vol. 33, no. 21, pp. 1201-1204, 2021.

[45] H. Tai, H. Tanaka and T. Yoshino, "Fiber-optic evanescent-wave methane-gas sensor using optical absorption for the 3.392- μm line of a He-Ne laser," Opt. Lett., vol. 12, no. 6, pp. 437-439, 1987.

[46] P. Lu, L. Men, et al., "Tapered fiber Mach–Zehnder interferometer for simultaneous measurement of refractive index and temperature," Appl. Phys. Lett., vol. 94, no. 13, Apr. 2009.

[47] W. Zhang, X. Lang, X. Liu, G. Li, R. Singh, B. Zhang and S. Kumar, "Advances in Tapered Optical Fiber Sensor Structures: From Conventional to Novel and Emerging," Biosensors, vol. 13, no. 6, Jun. 2023.

[48] X. Fu et al. "A temperature sensor based on the splicing of a core offset multi-mode fiber with two single mode fiber," Optoelectron. Lett., vol. 11, pp.434–437, Nov. 2015.

[49] T. Zhou, Y. Zhang, B. Han, A. Zhang and D. Fu, "Low-cost non-adiabatic tapered fiber for high-sensitive temperature sensing," Opt. Fiber Technol., vol. 45, pp. 53-57, 2018.

[50] A. Séguin, et al., "Fabrication and characterization of indium fluoride multimode fused fiber couplers for the mid-infrared," Opt. Express, vol. 31, no. 20, pp. 33670-33678, 2023.

[51] G. Li, Y. Ge, and Z. Chen, "A Compact Multibeam Folded Transmitarray Antenna at Ku-Band", IEEE Antennas Wirel. Propag. Lett., vol. 20, no. 5, pp. 808-812, May 2021.

[52] Y. Ge, C. Lin, and Y. Liu, "Broadband Folded Transmitarray Antenna Based on an Ultrathin Transmission Polarizer", IEEE Trans. Antennas Propag., vol. 66, no. 11, pp. 5974-5981, Nov. 2018.

[53] S. Ghosh, D. Sen, "An Inclusive Survey on Array Antenna Design for Millimeter-Wave Communications," IEEE Access, vol. 7, pp. 83137-83161, 2019.

[54] T. Potelon, M. Ettorre, L. Le Coq, T. Bateman, J. Francey, R. Sauleau, "Reconfigurable CTS Antenna Fully Integrated in PCB Technology for 5G Backhaul Applications," IEEE Trans. Antennas Propag., vol. 67, no. 6, pp. 3609–3618, Jun. 2019.

[55] F. Foglia Manzillo, M. Ettorre, M. S. Lahti, K. T. Kautio, D. Lelaidier, E. Seguenot, and R. Sauleau, "A Multilayer LTCC Solution for Integrat-ing 5G Access Point Antenna Modules," IEEE Trans. Microw. Theory Tech., vol. 64, no. 7, pp. 2272-2283, Jul. 2016.

[56] M. Bozzi, A. Georgiadis, K. Wu, "Review of substrate-integrated waveguide circuits and antennas," IET Microw. Antennas Propag., vol. 5, no. 8, pp. 909–920, Jul. 2011.

[57] K. Y. Kapusuz, A. V. Berghe, S. Lemey, H. Rogier, "Partially Filled Half-Mode Substrate Integrated Waveguide Leaky-Wave Antenna for 24 GHz Automotive Radar," IEEE Antennas Wirel. Propag. Lett., vol. 20, no. 1, pp. 33-37, Jan. 2021.

[58] F. Parment, A. Ghiotto, T.-P- Vuong, J.-M- Duchamp, K. Wu, "Millimeter wave air-filled substrate integrated waveguide slot array antenna," Electron. Lett., vol. 53, no. 11, Mar. 2017.

[59] A. Belenguer, H. Esteban, A. L. Borja, V. E. Boria, "Empty SIW Technologies: A Major Step Toward Realizing Low-Cost and Low-Loss Microwave Circuits," IEEE Microw. Mag., vol. 20, no. 3, pp. 24-45, Mar. 2019.

[60] C. Bian, D. Zhou, Y. Zhang, D. Lv, H. Deng, D. Zhang, "A Multi-Polarization Folded Transmitarray Antenna Based on Huygens' Metasurface", IEEE Antennas Wirel. Propag. Lett., vol. 22, no. 12, pp. 2783-2787, Dec. 2023.

[61] C. Yang, G. Wu, et al., "An Ultralow-Profile Folded Transmitarray Antenna Based on a Multifunctional Metasurface with Both-Sided Wavefront Control", IEEE Trans. Antennas Propag., vol.71, no. 10, pp. 7804-7812, Oct. 2023.

[62] M. Wang, et al., "On Folded Transmitarray with Dual Polarization," IEEE Trans. Antennas Propag., vol. 72, no. 2, pp. 1343-1351, Feb. 2024.

[63] H.X. Xu, T. Cai, et al., "Dual-Mode Transmissive Metasurface and Its Applications in Multibeam Transmitarray," IEEE Trans. Antennas Propag., vol. 65, no. 4, pp. 1797-1806, Apr. 2017.

[64] K. T. Pham, R. Sauleau, et al., “Dual-Band Transmitarrays with Dual-Linear Polarization at Ka-Band,” IEEE Trans. Antennas Propag., vol. 65, no. 12, pp. 7009-7018, Dec. 2017.

[65] T. K. Pham, L. Guang, D. González-Ovejero, and R. Sauleau, “Dual-Band Transmitarray with Low Scan Loss for Satcom Applications,” IEEE Trans. Antennas Propag., vol. 69, no. 3, pp. 1775-1780, Mar. 2021.

[66] C. Fan, W. Che, W. Yang, and S. He, Member, “A Novel PRAMC-Based Ultralow-Profile Transmitarray Antenna by Using Ray Tracing Principle,” IEEE Trans. Antennas Propag., vol. 65, no. 4, pp. 1779-1787, Apr. 2017.

[67] C. Lee; T. V. Hoang, et al., “Low-profile quad-beam circularly polarised antenna using transmissive metasurface,” IET Microw. Antennas Propag. 2019, vol.13, no. 10, pp. 1690–1698.

[68] Y. Wang, et al., “Broadband High-Efficiency Ultrathin Metasurfaces with Simultaneous Independent Control of Transmission and Reflection Amplitudes and Phases,” IEEE Trans. Microw. Theory Techn., vol. 70, no.1, pp. 254-263, Jan. 2022.

[69] Y. Caim, K. Li, W. Li, et al., "Dual-Band Circularly Polarized Transmitarray with Single Linearly Polarized Feed," IEEE Trans. Antennas Propag., vol. 68, no. 6, pp. 5015-5020, June 2020.

[70] C. Pfeiffer, and A. Grbic, "Millimeter-Wave Transmitarrays for Wavefront and Polarization Control," IEEE Trans. Microw. Theory Techn., vol. 61, no. 12, pp. 4407-4417, Dec. 2013.

[71] Y. H. Zhang, X. W. Dai, Y. H. Fu, N. Q. Tang, and D. L. Mi, "A Broadband Multi-Beam Dual-Circularly Polarized Reflect-Array for Ka-Band Application," IEEE Access, vol. 11, pp. 48593-48600, May 2023.

[72] J. Yang, S. T. Chen, et al. "Folded Transmitarray Antenna With Circular Polarization Based on Metasurface," IEEE Trans. Antennas Propag., vol. 69, no. 2, pp. 806-814, Feb. 2021.

[73] A. Aziz, F. Yang, et al., "A High-Gain Dual-Band and Dual-Polarized Transmitarray Using Novel Loop Elements," IEEE Trans. Antennas Propag., vol. 18, no. 6, pp. 1213-1217, Jun. 2019.

[74] S. H. R. Tuloti, A. Lamacki, et al., "An Optimized Ka-Band Low Profile Dual-Polarized Transmitarray Antenna With 2D Beam Switching," IEEE Access, vol. 12, no. 6, pp. 8924-8931, Jan. 2024.

[75] L. Wu, Q. Hu, et al., "Wideband Dual-Feed Dual-Polarized Reflectarray Antenna Using Anisotropic Metasurface," IEEE Antennas Wirel. Propag. Lett., vol. 21, no. 1, pp. 129-133, Jan. 2022.

[76] X. Wang, Y. Cheng, and Y. Dong, "Millimeter-Wave High-Efficiency Double-Layer Transmitarray Antenna Using Miniaturized Dual-Polarized Elements," IEEE Trans. Antennas Propag., vol. 70, no. 9, pp. 8637-8642, Sep. 2022.

[77] S. Yang, Z. Yan, et al "A High-Efficiency Double-Layer Transmitarray Antenna Using Low-Loss Dual-Linearly Polarized Elements," IEEE Antennas Wirel. Propag. Lett., vol. 19, no. 12, pp. 2378-2382, Dec. 2020.

[78] X. Yi, T. Su, et al., "A Double-Layer Wideband Transmitarray Antenna Using Two Degrees of Freedom Elements Around 20 GHz," IEEE Trans. Antennas Propag., vol. 67, no. 4, pp. 2798-2802, Apr. 2019.

[79] M. Li, Y. Ban, and F. Yan, “Wideband Low-Profile Ku-Band Transmitarray Antenna,” IEEE Access, vol. 9, pp. 6683-6688, Dec. 2021.

[80] A. Alù, S. Maci and N. Engheta, "Metasurfaces and Metamaterials for Electromagnetics," IEEE Trans. Antennas Propag., Early Access, Jul. 2025.

[81] C. Caloz, T. Itoh, Electromagnetic Metamaterials: Transmission Line Theory and Microwave applications, Hoboken, NJ, USA: John Wiley&Sons, Inc., 2006.

[82] L. Liu, X. Zhang, et al., “Broadband Metasurfaces with Simultaneous Control of Phase and Amplitude,” Adv. Mater., vol. 26, no. 29, pp.5031-6, Aug. 2014.

[83] X. Zhang, Z. Tian, et al., “Broadband Terahertz Wave Deflection Based on C-shape Complex Metamaterials with Phase Discontinuities,” Adv. Mater., vol. 25, no. 33, pp. 4567-4572, Sep. 2013.

[84] X. Shi, Y. Cao, Y. Hu, et al. “A High-Gain Antipodal Vivaldi Antenna with Director and Metamate-rial at 1–28 GHz,” IEEE Antennas Wirel. Propag. Lett., vol. 20, no. 12, pp. 2432–2436, 2021.

[85] V. Portosi, A. M. Loconsole, F. Prudenzano, “A Split Ring Resonator-Based Metamaterial for Microwave Impedance Matching with Biological Tissue,” Appl. Sci., vol. 10, no. 19, p. 6740, Sep. 2020.

[86] V. Portosi, A. M. Loconsole, et al., "Refinement of a Microwave Needle Applicator for Cancer Therapy via Metamaterials," in 2022 Microwave Mediterranean Symposium (MMS), Pizzo Calabro, Italy, May 2022, pp.1-5.

[87] F. Attivissimo, A. M. L. Lanzolla, et. al, "A novel electromagnetic tracking system for surgery navigation," Comput. Assist. Surg., vol.23 no. 1, pp. 42-52, Nov. 2018.

[88] D.R. Smith, D.C. Vier, et al., "Electromagnetic parameter retrieval from inhomogeneous metamaterials," Phys. Rev. E, vol. 71, no. 3, p. 036617, Mar. 2005.

[89] A. T. Castro and S. K. Sharma, "Inkjet-Printed Wideband Circularly Polarized Microstrip Patch Array Antenna on a PET Film Flexible Substrate Material," IEEE Antennas Wirel. Propag. Lett., vol. 17, no. 1, pp. 176–179, Jan. 2018.

[90] B. S. Cook and A. Shamim, "Inkjet Printing of Novel Wideband and High Gain Antennas on Low-Cost Paper Substrate," IEEE Trans. Antennas Propag., vol. 60, no. 9, pp. 4148–4156, Sep. 2012.

[91] B. S. Cook, B. Tehrani, J. R. Cooper, and M. M. Tentzeris, "Multilayer Inkjet Printing of Millimeter-Wave Proximity-Fed Patch Arrays on Flexible Substrates," IEEE Antennas Wirel. Propag. Lett., vol. 12, pp. 1351–1354, 2013.

[92] H. Saghlatoon, L. Sydanheimo, L. Ukkonen, and M. Tentzeris, "Optimization of Inkjet Printing of Patch Antennas on Low-Cost Fibrous Substrates," IEEE Antennas Wirel. Propag. Lett., vol. 13, pp. 915–918, 2014.

[93] Y. Ge, K. P. Esselle, and T. S. Bird, "The Use of Simple Thin Partially Reflective Surfaces with Positive Reflection Phase Gradients to Design Wideband, Low-Profile EBG Resonator Antennas," IEEE Trans. Antennas Propag., vol. 60, no. 2, pp. 743–750, Feb. 2012.

[94] R. M. Hashmi, B. A. Zeb, and K. P. Esselle, “Wideband High-Gain EBG Resonator Antennas with Small Footprints and All-Dielectric Superstructures,” IEEE Trans. Antennas Propag., vol. 62, no. 6, pp. 2970–2977, Jun. 2014.

[95] K. Konstantinidis, A. P. Feresidis, and P. S. Hall, “Multilayer Partially Reflective Surfaces for Broadband Fabry-Perot Cavity Antennas,” IEEE Trans. Antennas Propag., vol. 62, no. 7, pp. 3474–3481, Jul. 2014.

[96] B. A. Zeb, N. Nikolic, and K. P. Esselle, “A High-Gain Dual-Band EBG Resonator Antenna with Circular Polarization,” IEEE Antennas Wirel. Propag. Lett., vol. 14, pp. 108–111, 2015.

[97] M. A. Al-Tarifi, D. E. Anagnostou, A. K. Amert, and K. W. Whites, “Bandwidth Enhancement of the Resonant Cavity Antenna by Using Two Dielectric Superstrates,” IEEE Trans. Antennas Propag., vol. 61, no. 4, pp. 1898–1908, Apr. 2013.

[98] A. R. Weily, L. Horvath, K. P. Esselle, B. C. Sanders, and T. S. Bird, “A planar resonator antenna based on a woodpile EBG material,” IEEE Trans. Antennas Propag., vol. 53, no. 1, pp. 216–223, Jan. 2005.

[99] A. M. Loconsole, V. V. Francione, et al., "Mid-IR Amplification Based on a Pr3+: InF3 Optical Fiber in the Range 3.8−4.2 μm," J. Light. Technol., vol. 43, no. 11, pp. 5451-5458, Jun. 2025.

[100] K. Iizawa, S.K. Varshney, Y. Tsuchida, K. Saitoh, and M. Koshiba, "Bend-insensitive lasing characteristics of single-mode, large-mode-area Ytterbium-doped photonic crystal fiber," Opt. Express, vol. 16, no. 2, pp. 579-591, Jan. 2008.

[101] S. Hilaire, D. Pagnoux, P. Roy, and S. Fevrier, “Numerical study of single-mode Er-doped microstructured fibers: influence of geometrical parameters on amplifier performances,” Opt. Express, vol. 14, no. 22, Jul. 2006.

[102] S. Lacroix, F. Gonthier, et al. “Tapered-fiber interferometric wavelength response: the achromatic fringe,” Opt. Lett., vol.13, no. 5, pp. 395-397, May 1988.

[103] M. I. Zibaii, H. Latifi, M. Karami, M. Gholami, S. M. Hosseini, and M. H. Ghezelayagh, “Non-adiabatic tapered optical fiber sensor for measuring the interaction between α-amino acids in aqueous carbohydrate solution,” Meas. Sci. Technol., vol. 21, no. 10, p. 105801, Oct. 2010.

[104] A. Layeghi, H. Latifi and O. Frazão, "Magnetic Field Sensor Based on Nonadiabatic Tapered Optical Fiber with Magnetic Fluid," IEEE Photon. Technol. Lett., vol. 26, no. 19, pp. 1904-1907, 2014.

[105] Y. Cardona Maya, N. Gómez Cardona, and P. I. Torres Trujillo, “Low-cost heat-and-pull rig for manufacturing adiabatic optical fiber tapers,” Rev. Fac. Ing. Univ. Antioquia, no. 70, pp. 167–172, Feb. 2014.

[106] T. A. Birks, and Y. W. Li, “The shape of fiber tapers,” J. Light. Technol., vol. 10, no. 4, pp. 432–438, Apr. 1992.

[107] R. P. Kenny, T. A. Birks, and K. P. Oakley, “Control of optical fibre taper shape,” Electron. Lett., vol. 27, no. 18, p. 1654, 1991.

[108] N. A. Razak, B. A. Hamida, N. Irawati, and M. H. Habaebi, “Fabricate Optical Microfiber by Using Flame Brushing Technique and Coated with Polymer Polyaniline for Sensing Application,” IOP Conf. Ser. Mater. Sci. Eng., vol. 210, p. 012041, Jun. 2017.

[109] Y. Shestopalov, Y. Smirnov, and E. Smolkin, Optical Waveguide Theory: Mathematical Models, Spectral Theory and Numerical Analysis, in Springer Series in Optical Sciences, vol. 237. Singapore: Springer Singapore, 2022.

[110] J. D. Love, W. M. Henry, W. J. Stewart, R. J. Black, S. Lacroix, and F. Gonthier, "Tapered single-mode fibres and devices. Part 1: Adiabaticity criteria," IEEE Proc. J Optoelectron., vol. 138, no. 5, p. 343, 1991.

[111] A. M. Loconsole, V. Portosi, V. V. Francione, G. Roberto, F. Anelli and F. Prudenzano, "Wideband antipodal Vivaldi antenna with metalenses for GPR applications," in 2022 Microwave Mediterranean Symposium (MMS), Pizzo Calabro, Italy, May 2022, pp. 1-5.

[112] A. Z. Hood, T. Karacolak and E. Topsakal, "A Small Antipodal Vivaldi Antenna for Ultrawide-Band Applications," IEEE Antennas Wirel. Propag. Lett., vol. 7, pp. 656-660, 2008.

[113] A. M. Loconsole, V. Portosi, V. V. Francione, et al. "Optimization of a wideband antipodal Vivaldi antenna with metalenses," Int. J. Microw. Wirel. Technol., vol. 16, no. 1, pp. 41–48, Feb. 2024.

[114] Z. Szabó, G. -H. Park, R. Hedge and E. -P. Li, "A Unique Extraction of Metamaterial Parameters Based on Kramers–Kronig Relationship," IEEE Trans. Microw. Theory Tech., vol. 58, no. 10, pp. 2646-2653, Oct. 2010

[115] E. G. Ozaktas, S. Chintapalli, and S. M. Thon, "Optical parameter extraction for metamaterials via robust effective and equivalent medium models," Opt. Mater. Express, vol. 14, no. 2, pp. 457-471, Feb. 2024.

[116] X. Ran, X. -H. Wang, Y. -D. Hu, S. -W. Qu and B. -Z. Wang, "Dual-Polarized Nonuniform Fabry–Pérot Cavity Antenna with Flat-Topped Radiation Pattern," IEEE Antennas Wirel. Propag. Lett., vol. 21, no. 5, pp. 1060-1064, May 2022.

[117] N. Wang, C. Zhang, Q. Zeng, N. Wang, and J.-D. Xu, "New Dielectric 1-D EBG Structure for the Design of Wideband Resonator Antennas," Prog. Electromagn. Res., vol. 141, pp. 233–248, 2013.

[118] N. Wang, J. Li, G. Wei, L. Talbi, Q. Zeng, and J. Xu, "Wideband Fabry–Perot Resonator Antenna with Two Layers of Dielectric Superstrates," IEEE Antennas Wirel. Propag. Lett., vol. 14, pp. 229-232, Sep. 2015.

[119] T. Le-Huu, S. X. Ta, K. K. Nguyen, C. Dao-Ngoc, and N. Nguyen-Trong, "Differential-Fed Dual-Polarized Filtering Fabry-Perot Antenna With High Isolation," IEEE Access, vol. 10, pp. 94616-94623, Sep. 2022.

[120] M. W. Niaz, Y. Yin, R. A. Bhatti, Y.-M. Cai, and J. Chen, "Wideband Fabry–Perot Resonator Antenna Employing Multilayer Partially Reflective Surface," IEEE Trans. Antennas Propag., vol. 69, no. 4, pp. 2404–2409, Apr. 2021.

[121] S. Fang, L. Zhang, Y. Guan, Z. Weng, and X. Wen, "A Wideband Fabry–Perot Cavity Antenna with Single-Layer Partially Reflective Surface," IEEE Antennas Wirel. Propag. Lett., vol. 22, no. 2, pp. 412–416, Feb. 2023.

[122] F. Anelli, A. M. Loconsole, V. Portosi, A. Annunziato, V. V. Francione, and F. Prudenzano, "A Wideband Flexible Fabry-Perot Resonator Antenna: Inkjet-printing on Ultrathin PET Layers," in 2023 IEEE Conference on Antenna Measurements and Applications (CAMA), Genoa, Italy: IEEE, pp. 972-976, Nov. 2023.

[123] G. L. Huang, Z. Y. Pang, et al., "A Broadband and High-Aperture-Efficiency Multilayer Transmitarray Based on Aperture-Coupled Slot Unit Cells," IEEE Trans. Antennas Propag., vol. 71, no. 12, pp. 9633-9642, Dec. 2023.

[124] J. Huang, "Analysis of a Microstrip Reflectarray Antenna for Microspacecraft Applications" TDA Progress Report 42-120, NASA, Feb. 1995.

[125] D. M. Pozar, et al., "Design of Millimeter Wave Microstrip Reflectarrays," IEEE Trans. Antennas Propag., vol. 45, no. 2, Feb. 1997.

[126] T. J. Li, G. M. Wang, et al., "Broadband Folded Transmitarray Antenna with Ultralow-Profile Based on Metasurfaces," IEEE Trans. Antennas Propag., vol. 69, no. 10, pp. 7017-7022, Oct. 2021.

[127] S. Zhang, W. Cao, et al., "The Design of a Multifunctional Coding Transmitarray with Independent Manipulation of the Polarization States," Micromachines, vol 15, no. 8, p. 1014, Aug. 2024.

[128] D. M. Pozar, Microwave Engineering. New York, NY, USA: Wiley, 2009.

[129] C. Falconi, A. M. Loconsole, D. Laneve, et al., "Design of active devices based on rare-earth-doped glass/glass ceramic: from the material characterization to the device parameter refinement," in Proc. SPIE Fiber Lasers and Glass Photonics: Materials through Applications II, Strasbourg, France, vol. 11357, Apr. 2020, pp. 39-45.

[130] C. Falconi, A. M. Loconsole, A. Annunziato, et al., "Design of an Er3+: InF3 fiber laser pumped with red light," in Proc. SPIE Fiber Lasers and Glass Photonics: Materials through Applications III, Strasbourg, France, vol. 121420, Apr. 2022, art. no. 1214210.

[131] Le Verre Fluoré, Catalog, Bruz, Brittany, France, 2022. Available online: https://leverrefluore.com/wp-content/uploads/2022/02/LVF-Catalog-2022.pdf

[132] F. Anelli, A. Annunziato, A. M. Loconsole, et al., "Low-Loss Fluoride Optical Fiber Coupler for Mid-Infrared Applications," J. Light. Technol., vol. 42, no. 7, pp. 2457-2463, Apr. 2024.

[133] P.C. Becker, N.A. Olsson, and J.R. Simpson, "Erbium-Doped Fiber Amplifier: Fundamentals and Technology," Wiley, New York, 2002, pp. 131-250.

[134] W.A. Pisarski, J. Pisarska, et al., "Fluoroindate glasses co-doped with Pr3+/Er3+ for near-infrared luminescence applications", Sci. Rep., vol. 10, art. no. 21105, Dec. 2020.

[135] A. Flórez, O.L. Malta, Y. Messaddeq, and M.A. Aegerter, "Judd-Ofelt analysis of Pr3+ ions in fluoroindate glasses: influence of odd third order intensity parameters", J. Non-Cryst. Solids, vol. 213-214, pp. 315-320, May 1997.

[136] D. Manzani, D. Pabœuf, S. J. L. Ribeiro, P. Goldner, F. Bretenaker, "Orange emission in Pr3+-doped fluoroindate glasses," Optical Materials, vol. 35, no. 3, pp. 383-386, 2013.

[137] R. S. Quimby, and B. Zheng, "New excited state absorption measurement technique and application to Pr3+-doped fluorozirconate glass", Appl. Phys. Lett., vol. 60, pp. 1055-1057, Mar. 1992.

[138] A. Remillieux, B. Jacquier, C. Linarès, C. Lesergent, S. Artigaud, D. Bayard, L. Hamon, and J. L. Beylat, "Upconversion mechanisms of a praseodymium-doped fluoride fibre amplifier", J. Phys. D: Appl. Phys., vol. 29, no. 4, pp. 963-974, Jan. 1996.

[139] R. Pappalardo “Calculated quantum yields for photon-cascade emission (PCE) for Pr3+ and Tm3+ in fluoride hosts”, J. Lumin., vol. 14, no. 3, pp. 159-163, 1976.

[140] L. Gomes, S. D. Jackson “Spectroscopic properties of ytterbium, praseodymium-codoped fluorozirconate glass for laser emission at 3.6 μm”, J. Opt. Soc. Am. B, vol. 30, no. 6, pp. 1410-1419, 2013.

[141] A. M. Loconsole, F. Anelli, V. V. Francione, and F. Prudenzano, "Active Devices Based on Rare-Earth-doped Fluoroindate Fibers in Mid-Infrared Range," in 2025 25th Anniversary International Conference on Transparent Optical Networks (ICTON), Barcelona, Spain, 2025, pp. 1-4.

[142] E. Desurvire, “Erbium-doped Fiber Amplifier – Principles and Applications,” John Wiley & Sons Inc., 1994, pp. 306–452.

[143] M. J. F. Digonnet, “Rare-Earth-Doped Fiber Lasers and Amplifiers,” 2 ed., New York, NY, USA: Marcel Dekker, 1997, pp. 531-582.

[144] L. Michaud, T. Boilard, R.Vallée, M. Bernier, “Mid-Infrared Fiber Amplification of a DFB Interband Cascade Laser,” Photonics, vol. 12, p. 988, Oct. 2025.

[145] X. Zhu, Z. Chen, Q. Jiang, et al. "Mid-infrared all-fiber superfluorescent source in Er3+-doped fluoride fiber," Opt. Laser Technol., vol. 179, p. 111266, Jun. 2024.

[146] Le Verre Fluoré, General properties. Available online: https://leverrefluore.com/scientific-world/fluoride-fibers/general-properties/

[147] X. Leng, and S. S.-H. Yam, "Mode Interference in Non-Adiabatic Fiber Taper with a Long Uniform Region," IEEE Photon. Technol. Lett., vol. 31, no. 18, pp. 1491-1494, Sep. 2019.

[148] Y. Liu, and D. N. Wang, "Fiber In-Line Fabry-Perot Interferometer With Offset Splicing for Strain Measurement with Enhanced Sensitivity," IEEE Photon. J., vol. 10, no. 1, pp. 1-8, Feb. 2018.

[149] L. Rosa, S. Mckee, F. Poli, A. Cucinotta, and L. Vincetti, "Thermo-optical numerical modal analysis of multicore fibers for high power lasers and amplifiers," Opt. Fiber Technol., vol. 70, art. 102857, May 2022.

[150] A. Annunziato, F. Anelli, et al., "Design of Polarization-Maintaining FBGs Using Polyimide Films to Improve Strain-Temperature Sensing in CFRP Laminates," IEEE Photon. J., vol. 13, no. 2, pp. 1-15, Apr. 2021.

[151] Y. Deng, R. Flores-Flores, R. K. Jain and M. Hossein-Zadeh, "Thermo-optomechanical oscillations in high-Q ZBLAN microspheres," Opt. Lett., vol. 38, no. 21, pp. 4413-4416, 2013.

[152] L. Yuan, T. Wei, Q. Han, H. Wang, J. Huang, L. Jiang and H. Xiao, "Fiber inline Michelson interferometer fabricated by a femtosecond laser," Opt. Lett., vol. 37, no. 21, pp. 4489-4491, 2012.

[153] P. Lu and Q. Chen, "Asymmetrical Fiber Mach–Zehnder Interferometer for Simultaneous Measurement of Axial Strain and Temperature," IEEE Photon. J., vol. 2, no. 6, pp. 942-953, Dec. 2010.

[154] É. Ducharme, S. Virally, et al., "Viscosity of fluoride glass fibers for fused component fabrication," Appl. Opt., vol. 61, no. 17, pp. 5031-5039, Jun. 2022.

[155] D.-P. Zhou, L. Wei, W.-K. Liu, Y. Liu and J. W. Y. Lit, " Simultaneous measurement for strain and temperature using fiber Bragg gratings and multimode fibers," Appl. Opt., vol. 47, no. 10, pp. 1668-1672, 2008.

[156] K. Wang, Y. Mizuno, H. Lee, et al., "Experimental demonstration of offset-induced sensitivity enhancement in SMS-based temperature and strain sensing," Appl. Phys. Express, vol. 16, no. 5, art. no. 052003, May 2023.

[157] X. Dong, L. Su, P. Shum, Y. Chung and C.C. Chan, "Wavelength-selective all-fiber filter based on a single long-period fiber grating and a misaligned splicing point," Opt. Commun., vol. 258, no. 2, pp. 159-163, Feb. 2006.

[158] T. Wei, X. Lan, and H. Xiao, "Fiber Inline Core–Cladding-Mode Mach–Zehnder Interferometer Fabricated by Two-Point CO2 Laser Irradiations," IEEE Photon. Technol. Lett., vol. 21, no. 10, pp. 669-671, May 2009.

[159] Z. Zhang et al., "Hollow-Core-Fiber-Based Interferometer for High-Temperature Measurements," IEEE Photon. J., vol. 9, no. 2, pp. 1-9, Apr. 2017.

[160] J. Zhang et al., "Ultrasensitive Temperature Sensor with Cascaded Fiber Optic Fabry–Perot Interferometers Based on Vernier Effect," IEEE Photon. J., vol. 10, no. 5, pp. 1-11, Oct. 2018.

[161] F. Liu, Y. Zhang, F. Meng, M. Dong, L. Zhu, and F. Luo, "Complex optical fiber sensor based on the Vernier effect for temperature sensing," Opt. Fiber Technol., vol. 61, p. 102424, Jan. 2021.

[162] A. D. D. Le, J. Hwang, M. Yusuf, K. H. Park, S. Park, and J. Kim, "Simultaneous measurement of humidity and temperature with cytopreduced graphene oxide-overlaid two-mode optical fiber sensor," Sens Actuators B Chem., vol. 298, p. 126841, Nov. 2019.

[163] X. Li, H. Zhou, Z. Gao, et al., "Metamaterial Slabs Covered UWB Antipodal Vivaldi Antenna," IEEE Antennas Wirel. Propag. Lett., vol. 16, pp. 2943–2946, Sep. 2017.

[164] L. Chen, Z. Lei, et al. "A Broadband Artificial Material for Gain Enhancement of Antipodal Tapered Slot Antenna," IEEE Trans. Antennas Propag., vol. 63, no. 1, pp. 395-400, Jan. 2015.

[165] N. Wang, Q. Liu, C. Wu, L. Talbi, Q. Zeng and J. Xu, "Wideband Fabry-Perot Resonator Antenna with Two Complementary FSS Layers," IEEE Trans. Antennas Propag., vol. 62, no. 5, pp. 2463–2471, May 2014.

[166] Y. Pan, J. Dong, and M. Wang, "Equivalent Circuit-Assisted Multi-Objective Particle Swarm Optimization for Accelerated Reverse Design of Multi-Layer Frequency Selective Surface," Nanomaterials, vol. 12, no. 21, p. 3846, Oct. 2022.

[167] F. Anelli, A. M. Loconsole, V. V. Francione, Md. I. Khan and F. Prudenzano, "Cost-effective Fabry-Pérot Antenna via Conductive Inkjet and Additive Printing," IEEE Antennas Wirel. Propag. Lett., vol. 24, no. 8, pp. 2182-2186, Aug. 2025.

[168] G. Gonçalves Machado, R. Cahill, V. Fusco, and G. Conway, "Frequency selective superstrate absorber for wideband RCS reduction of metal-backed antennas," IET Microw. Antennas Propag., vol. 15, no. 4, pp. 441–450, Mar. 2021.

[169] M. M. Taskhiri and S. Fakhte, "Broadband inhomogeneous lens with conical radiation pattern," Sci. Rep., vol. 13, no. 1, p. 12907, Aug. 2023.

[170] J. A. Ansari, S. K. Dubey, P. Singh, R. U. Khan, and B. R. Vishvakarma, "Analysis of V-slot loaded patch for wide-band operation," Microw. Opt. Technol. Lett., vol. 50, no. 12, pp. 3069–3075, Dec. 2008.

[171] S. F. Jilani, M. O. Munoz, Q. H. Abbasi, and A. Alomainy, “Millimeter-Wave Liquid Crystal Polymer Based Conformal Antenna Array for 5G Applications,” IEEE Antennas Wirel. Propag. Lett., vol. 18, no. 1, pp. 84–88, Jan. 2019.

[172] W. Peng, J. Yu, H. Zhang, X. Wang, C. Zhang, and H. Xiao, “High-Bandwidth Flexible Inkjet-Printed Antenna Design for Microwave Power Transfer Applications,” IEEE Electron Device Lett., vol. 45, no. 7, pp. 1377–1380, Jul. 2024.

[173] Md. I. Khan, A. M. Loconsole, F. Anelli, V. V. Francione, et al., “A Low-Profile Dual-Polarized Transmitarray with Enhanced Gain and Beam Steering at Ku Band,” Appl. Sci., vol. 15, no. 9, p. 4656, Apr. 2025.

[174] Z. Li, X. Weng, X. Yi, et al., “Design and analysis of a complementary structure-based high selectivity triband frequency selective surface,” Sci. Rep., vol. 14, art. no. 9415, Apr. 2024.

[175] O. Losito, V. Portosi, G. Venanzoni, et al., “Feasibility investigation of SIW cavity-backed patch antenna array for Ku-band applications,” Appl. Sci., vol. 9, no 7, p. 1271, Mar. 2019.

[176] M. Jiang, Z. N. Chen, et al., “Metamaterial-based thin planar lens antenna for spatial beamforming and multibeam massive MIMO,” IEEE Trans. Antennas Propag., vol. 65, no. 2, pp. 464-472, Feb. 2017.

[177] F. Zhang, G.-M. Yang, and Y.-Q. Jin, "Low-profile circularly polarized transmitarray for wide-angle beam control with a third-order meta-FSS," IEEE Trans. Antennas Propag., vol. 68, no. 5, pp. 3586–3597, May 2020.

[178] M. Niroo Jazi, M. R. Chaharmir, J. Shaker, and A. R. Sebak, "Broadband transmitarray antenna design using polarization-insensitive frequency selective surfaces," IEEE Trans. Antennas Propag., vol. 64, no. 1, pp. 99–108, Jan. 2016.

[179] Horn Antenna Standard Gain / High Gain / Wide Band, model ATM-28-441, Available online: https://www.atmmicrowave.com/waveguide/horn-antenna-standard-gain-wide-band/

[180] EverythingRF, model WR28, Available online: https://www.everythingrf.com/tech-resources/waveguides-sizes

[181] A. H. Abdelrahman, F. Yang, A. Z. Elsherbeni, and P. Nayeri, Analysis and Design of Transmitarray Antennas, San Rafael, CA, USA: Morgan & Claypool, 2017.